CONSTRAINING PHYSICS BEYOND THE COSMOLOGICAL STANDARD MODEL

A Dissertation

Presented to the Faculty of the Graduate School

of Cornell University

in Partial Fulfillment of the Requirements for the Degree of

Doctor of Philosophy

by

Eva-Maria Katarina Mueller

February 2016

CONSTRAINING PHYSICS BEYOND THE COSMOLOGICAL STANDARD MODEL

Eva-Maria Katarina Mueller, Ph.D.

Cornell University 2016

In this thesis we consider cosmological constraints arising from the background expansion history on the effective field theory (EFT) of cosmic acceleration, a theoretical framework that allows for a unified way to classify both models of dark energy and modified gravity within the linear regime. In the Einstein frame, the most general action for the background can be written in terms of a canonical scalar field which is nonminimally coupled to matter. The leading corrections to the action are expressible through a quartic kinetic term, and scalar couplings to a Gauss-Bonnet curvature term and the Einstein tensor. We determine the implications of the terms in this general action for the predicted expansion history in the context of dynamical attractors. We find that each modifies the matter dominated and/or accelerative eras in ways that allow us to place cosmological constraints on them. We present current constraints on the effective action using the latest Type Ia supernovae, cosmic microwave background (CMB), and baryonic acoustic oscillation (BAO) data. This includes the finding that the scalar field EFT with a coupled Gauss-Bonnet term and the data are significantly discrepant.

In addition, we calculate the constraints on dark energy and cosmic modifications to gravity achievable with upcoming CMB surveys sensitive to the Sunyaev-Zel'dovich (SZ) effects. The analysis focuses on using the mean pairwise velocity of clusters as observed through the kinematic SZ effect (kSZ), an approach based on the same methods used for the first detection of the kSZ effect, and includes a detailed derivation and discussion of this statistic's covariance under a variety of different survey assumptions.

The potential of current, "Stage II" (ACTPol + BOSS), and upcoming, "Stage III"

(Advanced ACTPol + BOSS), and "Stage IV" (CMB-S4 + DESI), CMB observations are considered, in combination with contemporaneous spectroscopic and photometric galaxy observations. A detailed assessment is made of the sensitivity to the assumed statistical and systematic uncertainties in the optical depth determination, the magnitude and uncertainty in the minimum detectable mass, and the importance of pairwise velocity correlations at small separations, where nonlinear effects can start to arise.

In combination with Stage III constraints on the expansion history, such as those projected by the Dark Energy Task Force, we forecast 5% and 3% for fractional errors on the growth factor, γ, for Stage III and Stage IV surveys respectively, and 2% constraints on the growth rate, f_g, for a Stage IV survey for $0.2 < z < 0.6$. The results suggest that kSZ measurements of cluster peculiar velocities, obtained from cross-correlation with upcoming spectroscopic galaxy surveys, could provide robust tests of dark energy and theories of gravity on cosmic scales.

We present the mean pairwise momentum of clusters, as observed through the kSZ effect, as a novel probe of massive neutrinos. We find that kSZ measurements with current and upcoming surveys will provide complementary constraints on the sum of neutrino masses from large scale structure (LSS) and will improve on Planck satellite measurements of the primordial cosmic CMB and CMB lensing. Central to the constraints is a distinctive scale dependency of the kSZ neutrino signature on the mean pairwise momentum of clusters that we do not expect to be mirrored in systematic effects that change the overall amplitude of the signal, like the cluster optical depth. Assuming a minimal ΛCDM cosmology including massive neutrinos with Planck primordial CMB priors combined with conservative kSZ specifications, we forecast 68% upper limits on the neutrino mass sum of 310, 240, 110 meV for Stage II, Stage III, and Stage IV surveys respectively, compared to the Planck alone forecast of 540 meV. These forecasts include the ability to simultaneously constrain the neutrino mass sum and the mass-averaged optical depth of the cluster sample in each redshift bin. If the averaged optical depth of clusters can be measured with few percent accuracy

and a lower limiting mass is assumed, the projected kSZ constraints improve further to 100, 85 and 33 meV (Stage II, III and IV). These forecasts represent a conservative estimate of neutrino constraints using cross-correlations of arcminute-resolution CMB measurements and spectroscopic galaxy surveys. More information relevant for neutrino constraints is available from these surveys, such as galaxy clustering, weak lensing, and CMB temperature and polarization.

Biographical Sketch

Eva-Maria Mueller was born in 1986 in Nürnberg, Germany and grew up in the small town of Eckental, Forth. After graduating from high school in 2005, she went on an adventure to Central America, volunteering for the Red Cross in Panama and traveling across Costa Rica and Nicaragua. She attended the Ruprecht-Karls-Universität Heidelberg from 2006 to 2009, getting her first research experience in Astrophysics working with Professor Dr. Burkhard Fuchs. In 2009, Eva moved to Ithaca, NY, to study Physics at Cornell University as a Fulbright scholar. She decided to continue her studies at Cornell, pursuing a graduate career in Cosmology working with Professor Rachel Bean.

This dissertation is dedicated to my parents, Jutta Müller and Bernd Moll.

Acknowledgements

I wish to thank my advisor Rachel Bean for teaching me how to be a scientist. Your enthusiasm, support and advice kept me going.

I would like to thank Professor Michael D. Niemack, whom I consider my co-advisor, for expanding my horizon to the experimental side of cosmology and countless useful discussions. Special thanks to Francesco de Bernardis and Scott Watson for very enjoyable collaboration, endless patience and guidance through my graduate career.

Furthermore, I am very grateful for the many contributions to my scientific education here at Cornell University by Jolyon Bloomfield, Éanna Flanagan, Joyce Byun and Tom Loredo.

I am in debt to the Department of Astronomy for friendly environment, hospitality and support during all these years.

And finally, I specially wish to thank my family and Andrusha for supporting me during difficult times, Michael, Ryan, Mike and Tyler for distracting me from work and supplying me with coffee through numerous trips to the C-store, as well as Manolis for frequently coming to my office for no apparent reason.

This research was supported in part by the Cornell University Physics Department, NASA ATP grants NNX11AI95G, NNX08AH27G and NNX14AH53G, NASA ROSES grant 12-EUCLID12- 0004, NSF CAREER grant 0844825, NSF grant PHY0968820, and DoE grant DE-SC0011838, and the John and David Boochever Prize Fellowship in Fundamental Theoretical Physics at Cornell University.

Table of Contents

List of Figures

List of Tables

List of Abbreviations

The following abbreviations are commonly used in this document.

- ACT –*Atacama Cosmology Telescope*
- BAO –*Baryonic Acoustic Oscillations*
- BOSS –*Baryon Oscillation Spectroscopic Survey*
- CMB – *Cosmic Microwave Background*
- DE –*Dark Energy*
- DES –*Dark Energy Survey*
- DESI –*Dark Energy Spectroscopic Instrument*
- DETF –*Dark Energy Task Force*
- EFT –*Effective Field Theory*
- FoM –*Figures of Merit*
- GB –*Gauss-Bonnet*, referring to the modification of the Einstein-Hilbert action
- GR –*General Relativity*
- kSZ –*kinetic Sunyaev-Zel'dovich*, referring to the secondary anisotropy effect in the CMB.
- ΛCDM –Λ *Cold Dark Matter*, referring to the concordance model of cosmology.
- ΛMDM –Λ *Mixed Dark Matter*, referring to the ΛCDM model including massive neutrinos
- LRG –*Luminous Red Galaxy*
- LSS –*Large Scale Structure*
- LSST –*Large Synoptic Survey Telescope*
- MCMC –*Markov Chain Monte Carlo*
- MG –*Modified Gravity*
- SDSS –*Sloan Digital Sky Survey*
- SN –*Supernovae*
- SPT –*South Pole Telescope*
- SZ –*Sunyaev-Zel'dovich*, referring to the secondary anisotropy effect in the CMB.
- WMAP –*Wilkinson Microwave Anisotropy Probe*

Preface

Citations to Previously Published Work

This dissertation includes material from work that has been previously published or submitted as follows.

> Eva-Maria Mueller, Rachel Bean, Scott Watson. Cosmological implications of the effective field theory of cosmic acceleration [1]. Physical Review D,vol. 87, Issue 8, id. 083504, 2013
>

> Eva-Maria Mueller, Francesco de Bernardis, Rachel Bean, Michael D. Niemack. Constraints on gravity and dark energy from the pairwise kinematic Sunyaev-Zeldovich effect [2]. Astrophysical Journal,vol. 808 (2015) 1, 47
>

> Eva-Maria Mueller, Francesco de Bernardis, Rachel Bean, Michael D. Niemack. Constraints on massive neutrinos from the pairwise kinematic Sunyaev-Zel'dovich effect [3]. Physical Review D, vol. 92, Issue 6, id. 063501, 2015
>

Permission from coauthors has been granted for these works to be included in this dissertation.

Chapter 1

Introduction

Contents

"Some say the world will end in fire, / Some say in ice" are the famous first lines of Robert Frost poem 'Fire and Ice' about the future of our Universe. The fate of our Universe has not only inspired writers to compose poems, but also generations of physicist to pursue a career in cosmology. Despite great advances in both technology as well as theory, many question about our Universe remain puzzling. Why is our Universe accelerating? What is the nature of dark matter? Why does our Universe appear to be flat? Why is the Universe so smooth? And many more!

The aim of this thesis is to shed light on some of these questions by building a bridge between cosmological observations and fundamental physical theories.

1.1 The ΛCDM Universe

In the Λ cold dark matter (ΛCDM) model, the Universe consists of baryonic matter, dark matter, which only interacts gravitationally, radiation, i.e. photons and neutrinos, as well as

a cosmological constant, Λ. The cosmological constant was originally introduced by Einstein in 1917 to assure a static Universe. Later on, he dismissed the cosmological constant as his "biggest blunder". Almost a century later, however, his idea was revived to explain the acceleration of the Universe at late times and his "biggest blunder" became part of the standard model of cosmology, the ΛCDM Universe.

I Background evolution

On large scales our Universe appears to be homogenous and isotropic and is therefore well described by the Friedmann-Robertson-Walker (FRW) metric

$$ds^2 = -dt^2 + a(t)^2 \left(\frac{dr^2}{1 - kr^2} + r^2 d\theta^2 + r^2 sin^2\theta d\phi \right) \tag{1.1.1}$$

where a(t) is the scale factor and k the spatial curvature. Evaluating the fundamental equations of general relativity, the Einstein equations,

$$G_{\mu\nu} \equiv R_{\mu\nu} - \frac{1}{2} g_{\mu\nu} \mathcal{R} = 8\pi G T_{\mu\nu} \tag{1.1.2}$$

where $G_{\mu\nu}$ is the Einstein tenor, $R_{\mu\nu}$ the Riemann tensor, $T_{\mu\nu}$ the energy momentum tensor and R the Ricci scalar, for the FRW metric leads to the Friedmann equations, which govern the background evolution of our Universe,

$$H^2 = \left(\frac{\dot{a}}{a} \right)^2 = \frac{8\pi G}{3} \rho - \frac{kc^2}{a^2} \tag{1.1.3}$$

$$\dot{H} + H^2 = \frac{\ddot{a}}{a} = -\frac{4\pi G}{3} \left(\rho + \frac{3p}{c^2} \right) \tag{1.1.4}$$

with the Hubble parameter H and the total energy density given by

$$\rho = \rho_0 \left(\frac{\Omega_m}{a^3} + \frac{\Omega_r}{a^4} + \frac{\Omega_k}{a^2} + \Omega_\Lambda \right) \tag{1.1.5}$$

where Ω_x refers to the density fraction of matter, Ω_m, radiation, Ω_r, curvature, Ω_k and the cosmological constant, Ω_Λ.

II Perturbations

Even though on large scales the Universe appears homogenous and isotropic, over time small matter fluctuations can form galaxies and galaxy clusters and evolve into the large scale structure (LSS) of the Universe. The growth of these structures depends on the underlying physical theory and can therefore be used to constrain cosmological models. To account for perturbations around a smooth background, we can specify the metric in the Newtonian gauge as,

$$ds^2 = -(1 + 2\Psi(\mathbf{x}, t))dt^2 + a(t)^2(1 - 2\Phi(\mathbf{x}, t))d\mathbf{x}^2 \tag{1.1.6}$$

with the two Newtonian potentials Φ and Ψ. Combining the perturbed Einstein equations, that follow from (1.1.6), with the Poisson equation, the over-densities $\delta\rho$ can be related to the Newtonian potentials via

$$\nabla\Psi = 4\pi G a^2 \delta\rho \tag{1.1.7}$$

$$\nabla^2(\Phi + \Psi) = 8\pi G a^2 \delta\rho. \tag{1.1.8}$$

These equations fully describe the evolution of the scalar perturbations. The scalar perturbation are decoupled from the tensor perturbation and evolve independently. Tensor perturbations can play an important role in the very early Universe but are not further discussed in this work.

1.2 Physics beyond ΛCDM

I Dark energy and modified gravity

Current measurements of the expansion history have provided complementary evidence for the Universe's recent transition to a accelerative expansion. The primary constraints have come from geometric measurements of cosmic distances from Type Ia supernovae (SN)

luminosity distances [4, 5, 6, 7, 8, 9, 10], the angular scale of the sound horizon at last scattering imprinted in the cosmic microwave background (CMB) temperature correlations [11, 12, 13, 14, 15, 16], and in the distribution of large scale structure (LSS) through baryon acoustic oscillations (BAO) [17, 18, 19].

Understanding the underlying cause of this acceleration, under the broad banner of "dark energy", represents one of the primary challenges facing contemporary astronomy and astrophysics. Though current constraints are entirely consistent with a cosmological constant, Λ, a dynamically evolving dark energy is by no means ruled out by the data. Theoretically, the coincidence and fine-tuning problems associated with Λ have led theorists to consider broader alternative causes for the acceleration. These include introducing a new type of matter, typically in the form of a scalar field, or modifications to general relativity on large scales. Many models have been suggested in the literature, e.g., quintessence, non-minimal couplings between quintessence and matter, k-essence, $f(R)$-gravity, Brans-Dicke theories, Galileon gravity, and Dvali-Gabadadze-Porrati (DGP) gravity; see, for example, [20] for a review of a wide range of dark energy models, and [21, 22] for recent discussions on modified gravity models.

I.a Background evolution and Dark Energy

The most common way to parametrize our ignorance about the nature of dark energy is to modify the dark energy equation of state [23, 24]

$$w(a) = \frac{P}{\rho} = w_0 + (1-a)w_a \tag{1.2.1}$$

introducing two new parameters, w_0, a constant contribution to the equation of state, and w_a, a time dependent one, to allow a background evolution that evolves over time and therefore differs from that of a cosmological constant. We can recover the standard cosmological

constant for $w_0 = -1$ and $w_a = 0$. The dark energy density is the given by

$$\frac{\rho_\Lambda(z)}{\rho_\Lambda(0)} = \exp\left(\int_0^z dz' \frac{3\left[1 + w(z')\right]}{1 + z'}\right). \tag{1.2.2}$$

This is a simplistic approach, however, it encompasses the effects of many different dark energy model on the background evolution. To quantify the strength of upcoming surveys to constrain dark energy in this framework we are using the Dark Energy Task Force (DETF) Figures of Merit (FoM) ([25]) defined as

$$\text{FoM} \;=\; \det\left[(F^{-1})\right]^{-1/2}_{w_0,w_a}. \tag{1.2.3}$$

Higher FoM correspond to tighter constraints on dark energy for a given survey.

I.b Cosmic structure and modified gravity

According to linear theory, the matter over-density, δ_m, is related to the velocity of dark matter particles as $\dot{\delta}_m \propto v_m$, which connects the time evolution of the perturbations to the dark matter velocity. Any tracer of the underlying dark matter velocity distribution can be used to constrain cosmological parameters and in particular modified gravity models. In a variety of modified gravity scenarios the evolution of the density perturbations can be quite different from standard gravity even though the background expansion of the Universe is undistinguishable from a ΛCDM Universe (for example [26, 27, 28]). Thus, the LSS of the Universe is particularly important to verify or dismiss these theories. The linear perturbation equations have a solution of the form $\delta_m(\vec{x}, t) = D_a(t)\delta(x)$, factorizing the spatial and temporal dependency, with D_a being the growth factor. We can define the growth rate at a given scale factor, a, as

$$f_g(a) \equiv \frac{d\ln D_a}{d\ln a} \tag{1.2.4}$$

to parametrize the growth of structure. The growth rate is well approximated by $f_g(a) \approx \Omega_m(a)^\gamma$ with the growth index $\gamma \simeq 0.55$ for standard gravity ([29, 30]).

A more general approach is to modify the perturbed Einstein equations in combination with the Poisson equation (1.1.8) directly,

$$\nabla\Psi = 4\pi G a^2 \delta\rho \times G_M \tag{1.2.5}$$

$$\nabla^2(\Phi + \Psi) = 8\pi G a^2 \delta\rho \times G_L, \tag{1.2.6}$$

with two additional degrees of freedom, $G_M(a,k)$ and $G_L(a,k)$. Any deviation from unity of these two parameters would represent a deviation from general relativity. The first equation determines the growth of structure, whereas the second equation alters the lensing of light. Both parameters can therefore be constrained with LSS observations.

II Massive neutrinos

Neutrino flavor oscillations in atmospheric and solar neutrinos suggest that neutrinos are massive, implying an extension to the original Standard model of particle physics (e.g., [31, 32, 33, 34]). These results have also been confirmed by reactor experiments and particle accelerators (e.g., [35, 36, 37, 38]). Flavor oscillation experiments, however, cannot measure the neutrino mass eigenstates individually but only the squared mass differences [39],

$$\Delta m_{21}^2 = (7.59 \pm 0.20) \times 10^{-5}\ \mathrm{eV}^2 \tag{1.2.7}$$

$$|\Delta m_{31}|^2 = (2.43 \pm 0.13) \times 10^{-3}\ \mathrm{eV}^2. \tag{1.2.8}$$

These measurements allow two distinct neutrino mass hierarchies: normal ($m_1 < m_2 \ll m_3$) and inverted ($m_3 \ll m_1 \simeq m_2$), as well as a degenerate case ($m_3 \simeq m_2 \simeq m_1$). The difference in the squared masses implies there is a minimum neutrino mass sum of $\sum m_\nu \approx 58$ meV for the normal hierarchy, roughly two times larger for the inverted hierarchy, and ~ 150 meV for the degenerate case (e.g. [40]). Cosmological probes are primarily sensitive to the total sum of the neutrino masses, $\sum m_\nu$. Direct detection experiments in combination with cosmological probes will therefore provide valuable insights into the neutrino hierarchy.

Massive neutrinos affect the background expansion of the Universe as well as the growth of structure, which enables constraints from a variety of observations. At early times massive neutrinos are relativistic, acting as a radiation component, though they become nonrelativistic at a redshift that scales with the mass. CMB experiments can probe massive neutrinos through their effect on the redshift of matter-radiation equality, $z_{\rm eq}$, or the distance to the last scattering surface, $d_A(z_{\rm dec})$. Furthermore, since massive neutrinos suppress the matter power spectrum any probe of LSS, such as galaxies and galaxy clusters as well as the Lyman-α forest, is potentially sensitive to $\sum m_\nu$.

Current constraints on $\sum m_\nu$ depend strongly on the used data sets. Assuming a six-parameter minimal flat ΛCDM cosmology plus the neutrino mass sum as a free parameter leads to an upper limit of $\sum m_\nu < 0.72$ eV at 95% confidence level for CMB data only, Planck TT + lowP [41]. Including LSS information can further improve the results, yielding $\sum m_\nu < 0.21$ eV (95%, for Planck TT+lowP+BAO) [41]. Combining more data sets, such as Lyman-α surveys, can lead to even stronger constraints [42].

Neutrino science is not only interesting from a particle physics perspective, for it has also been used as a means of reconciling observed tensions in the primary CMB anisotropies, cluster counts, and lensing as measured by the Planck satellite [43], and between Planck and the Background Imaging of Cosmic Extragalactic Polarization experiment (BICEP) regarding the tensor-to-scalar ratio [44]. However, understanding systematic effects, such as cluster mass calibration for the former and foreground contamination by dust emission for the latter, is crucial for interpreting these discrepancies before ascribing them to neutrino physics. Nevertheless this illustrates that, despite having relatively small masses, neutrinos can play an important role in cosmology.

1.3 Cosmological observables

In this section we summarize the main cosmological observations that have lead to the concordance model of cosmology, mainly SN measurements, the discovery of the CMB and LSS probes.

I The cosmic microwave background

In 1964, the accidental discovery of the CMB at Bell labs, provided the first evidence for the Big Bang theory and has lead to an new, data-driven era in cosmology. Recently, the Planck satellite measured the anisotropies in the CMB to an impressive accuracy, following in the footsteps of the Cosmic Background Explorer (COBE), Wilkinson Microwave Anisotropy Probe (WMAP) as well the Atacama Cosmology Telescope (ACT) and the South Pole Telescope (SPT), among other small scale CMB experiments. The success of the CMB arises from its robustness to systematic effects as well as its well understood theoretical background based on linear theory.

The CMB temperature fluctuations at a given point on the sky,

$$\frac{\delta T}{T}(\theta,\phi) \equiv \frac{T(\theta,\phi) - \langle T \rangle}{\langle T \rangle} \tag{1.3.1}$$

are commonly decomposed into spherical harmonics, $Y_{lm}(\theta,\phi)$,

$$\frac{\delta T}{T}(\theta,\phi) = \sum_{l=0}^{\infty} \sum_{m=-1}^{l} a_{lm} Y_{lm}(\theta,\phi). \tag{1.3.2}$$

The correlation function, $C(\theta)$, of the temperature fluctuations can then be written in the form

$$C(\theta) = \frac{1}{4\pi} \sum_{l=0}^{\infty} (2l+1) C_l P_l(\cos(\theta), \tag{1.3.3}$$

where P_l are the usual Legendre polynomials. A simplified parametrization, that incorporates most of the geometrical information contained in the CMB anisotropies was introduced in

[45]. The CMB is sensitive to two distance ratios to decoupling, through the position of the peaks and the acoustic oscillations [45]: the acoustic scale at decoupling,

$$l_A(z_*) \equiv (1+z_*)\frac{\pi D_A(z_*)}{r_s(z_*)}, \tag{1.3.4}$$

and the "shift parameter",

$$\mathcal{R} \equiv \frac{\sqrt{\Omega_m H_0^2}}{c}(1+z_*)D_A(z_*), \tag{1.3.5}$$

where $D_A(z_*)$ is the angular diameter distance, and $r_s(z_*)$ is the sound horizon at the redshift to decoupling z_*. As discussed in [45], the definition of $\mathcal{R}$ suppresses the influence of radiation, dark energy or curvature on the Hubble parameter at decoupling $H(z_*)$ but is used by convention.

In addition to the primary anisotropies, the CMB exhibits secondary anisotropies, including the thermal and kinematic Sunyaev-Zel'dovich effect (kSZ). As the CMB photons pass through a galaxy cluster they get distorted due to the temperature of the cluster (thermal) or the velocity of the cluster (kinetic). Even though these effects are small compared to the primary CMB anisotropic, they provide a alternative way to constrain cosmology.

II Supernovae

The first evidence hinting at the accelerative expansion of the Universe came from Type Ia SN observations. Indeed, the nobel prize in physics has been awarded to Saul Perlmutter, Brian P. Schmidt and Adam G. Riess in 2011 "for the for the discovery of the accelerating expansion of the Universe through observations of distant supernovae". Their extraordinary achievements lie not 'merely' in the discovery of the acceleration but also in their meticulous treatment of instrumental, astrophysical and statistical systematics, that allowed them to rule out other possible explanations of their results. Cosmological SN constraints draw on the idea of a cosmological 'standard candle'; a quantity intrinsic to the observable, independent of its redshift and astrophysical properties that allows us to infer the redshift-distance relation.

In the case of Type Ia supernovae, the standard candle is the absolute brightness of the stellar explosion. The observed quantity is the distance modulus, μ, defined as

$$\mu(z) = 5 \log \left[\frac{D_L(z)}{1 \text{ Mpc}} \right] + 25, \tag{1.3.6}$$

where D_L is the luminosity distance. Even though SN are not "per se" standard candles, they can be calibrated precisely to effectively become one by relating their peak brightness to the light curves time scale. They have become one of the most powerful tools to trace the history of our Universe.

III Large scale structure of the Universe

LSS observations provide two complementary probes of the properties of gravity: the bending of light due to a gravitational potential and the effect of gravity on the motions of non-relativistic objects. The latter manifests as the peculiar velocities of galaxies imprinted in redshift space distortions (RSD) in the galaxy correlation function ([46]) as well as cluster motions as observed through the kinematic Sunyaev-Zel'dovich (kSZ) effect ([47]). Upcoming surveys such as the Dark Energy Survey (DES) ([48]), HyperSuprimeCam (HSC) ([1]), the Large Synoptic Survey Telescope (LSST) ([49]) and the Euclid ([50]) and WFIRST ([51]) space telescopes, will provide gravitational lensing surveys out to redshift two, and beyond. Concurrently spectroscopic surveys such as the extended Baryon Oscillation Spectroscopic Survey (eBOSS) ([52]), DESI ([53]) and spectroscopy from Euclid and WFIRST, will provide both BAO and redshift space clustering measurements over overlapping epochs and survey areas. Each of those probes, though having the potential to constrain gravity, are affected by systematic effects. Cosmological measurements using weak gravitational lensing (WL) will require precise photometric redshift and point spread function calibrations, along with characterization of intrinsic alignment contamination of shear correlations, (e.g. [54]), that

[1] http://sumire.ipmu.jp/en/

can bias and dilute dark energy constraints ([55, 56, 57]). Accurate modeling of redshift space clustering into the nonlinear regime requires precise descriptions of the galaxy clustering correlations beyond the Kaiser formula ([58]).

1.4 Likelihood Analysis

The increase in complexity of analyzing cosmological observations due to both, the quantity and quality of current and upcoming data sets as well as the intricacy of cosmological models, calls for more and more advanced, statistical techniques. The Likelihood function, $\mathcal{L}$, is a fundamental, statistical concept used in cosmology. The Likelihood describes the probability of the data, D, given the model, y, and is usually well approximated by a multi-variate Gaussian

$$\mathcal{L} = \frac{1}{(2\pi)^{n/2}|\det(C)|^{1/2}} \exp\left[-\frac{1}{2}\sum_{ij}(D_i - y_i)C_{ij}^{-1}(D_j - y_j)\right] \tag{1.4.1}$$

where $C_{ij} = \langle (D_i - y_i)(D_j - y_j)\rangle$ is the covariance matrix. The Likelihood can be evaluated to provide parameter estimates and to place bounds on these parameters.

In the following, two statistical methods, commonly used in cosmology, are outlined: The Markov chain Monte Carlo algorithm and the Fisher information technique.

I MCMC

The Markov chain Monte Carlo (MCMC) technique has become the standard tool in cosmology to estimate the Likelihood surface from the observed data. The MCMC is a probabilistic algorithm that generates random walks to sample a probability distribution, $p(\vec{x})$, for a multi-dimensional random variable $\vec{x}$. A common method is the Metropolis-Hastings algorithm. Given a starting point, $\vec{x}_0$, a sequence of points, called a "chain", is generated, $\vec{x}_1$, $\vec{x}_2$, ..., drawing from a proposal density, usually assumed to be a Gaussian. The trial, $\vec{x}_p$, is accepted

if $\alpha = p(\vec{x}_t)/p(\vec{x}_i) \geq 1$. Otherwise, the trial is rejected with a probability of (1-α) and accepted with the probability α. If $\vec{x}_t$ is accepted, it becomes the new starting point for the next trial; if $\vec{x}_t$ is rejected, the chain keeps searching around a last accepted point. In the limit of an infinitely long chain, the sequence of points reflects exactly the underlying probability distribution. In practice, a finite chain is said to be "converged" if it describes the distribution with sufficient accuracy. The convergence of a chain can be assessed using the Gelman & Rubin test, for instance. The Gelman & Rubin method can be applied if more than two chains of length, n, are calculated; it compares the variance within a chain, W, with the variance between several chains, B. The potential scale reduction factor, R, defined as

$$R = \frac{(1 - \frac{1}{n})W + \frac{1}{n}B}{W} \tag{1.4.2}$$

gives an estimate of the convergence of the chain. A smaller R value implies a better convergence.

II Fisher information

The Fisher information is a powerful, albeit time efficient, statistical technique to asses the strength of upcoming surveys. It is used to forecast the expected constraints on cosmological parameters as well as to quantify systematic uncertainties, depending only on the noise properties of the experiment. The Fisher formalism is based on the Cramér-Rao bound, stating that the inverse Fisher matrix, F^{-1}, is an estimate for the covariance matrix, C, of a given set of parameters, $\{\theta_i\}$. The 1σ error on a certain parameter θ_i is then given by $\sigma_{ii} \geq \sqrt{(F^{-1})_{ii}}$. The Fisher matrix is defined as

$$F_{ij} = -\left\langle \frac{\partial^2 \ln \mathcal{L}}{\partial\theta_i \partial\theta_j} \right\rangle \tag{1.4.3}$$

where $\langle\rangle$ denotes an ensemble average. Assuming the parameters $\{\theta_i\}$ are Gaussian distributed, the Fisher matrix can be interpreted as the expectation value of the Hessian matrix considering

the Taylor expansion of the log likelihood, $\mathcal{L}$,

$$\ln\mathcal{L} = \ln\mathcal{L}(\theta_0) + \frac{1}{2}\sum_{ij}(\theta_i - \theta_{i,0})\frac{\partial^2 \ln\mathcal{L}}{\partial\theta_i\partial\theta_j}\Big|_{\theta_0}(\theta_j - \theta_{j,0}) + ... \tag{1.4.4}$$

around the maximum likelihood value, $\theta_{i,0}$. The Fisher matrix can then be calculated as

$$F_{ij} = \frac{1}{2}\text{Trace}[C^{-1}C_{,i}C^{-1}C_{,j} + C^{-1}M_{ij}] \tag{1.4.5}$$

with the derivative of the covariance with respect to θ_i, $C_{,i}$, and the matrix M_{ij} defined as $M_{ij} = \mu_{,i}\mu^t_{,j} + \mu_{,j}\mu^t_{,i}$, given the mean μ of the observable. Assuming the covariance is independent of the cosmological parameter the Fisher matrix can be simplified to

$$F_{ij} = \mu^t_{,i}C^{-1}\mu_{,j}. \tag{1.4.6}$$

A detailed derivation of (1.4.6) can be found in [59].

Chapter 2

Cosmological Implications of the effective field theory of Cosmic Acceleration

Contents

2.1 Introduction

There has been significant progress in characterizing possible theoretical mechanisms to generate cosmic acceleration. Arguably, however, the improvements in the precision and breadth of observational constraints, of the expansion history and the growth of LSS, are providing remarkable opportunities to learn about the phenomenological properties of dark energy. As the accuracy of cosmological measurements continues to improve at a rapid pace, it is crucial to establish a robust and systematic way to connect data with fundamental theory. In particle physics and condensed matter systems the framework of effective field theory (EFT) has proven to be very successful at this endeavor (for reviews see [60, 61]).

The procedure is to construct the most general theory for observables that is compatible with the expected symmetries of the theory. The terms in the action can then be constrained by a combination of data from experiments, as well as ensuring theoretical self consistency.

The application of the EFT approach to cosmology has recently been carried out for single and multi-field inflation [62, 63]. In these papers the authors construct the most general action for the cosmological fluctuations around an assumed inflationary background. For inflation, this is reasonable, since apart from establishing a successful period of inflation the key observables are the correlation functions of scalar and metric perturbations. However, the same is not true for present day acceleration where the background expansion itself gives rise to observables, motivating the construction of the EFT of the background. Such an approach was first developed[1] for inflation by Weinberg [65] and for late-time cosmic acceleration in [66] – with later work appearing in [67, 68, 69, 70].

The goal of these approaches is to systematically categorize all proposals for cosmic acceleration, other than a cosmological constant, so they can be efficiently scrutinized by theory and experiment simultaneously. To facilitate such an approach a Lagrangian was constructed that could not only account for dark energy models, such as quintessence, but also theories of modified gravity in the linear regime. The relevant Lagrangian is that of a scalar-tensor theory nonminimally coupled to gravity, where in the modified gravity case the scalar can be interpreted as the extra degree of freedom arising from the longitudinal component of the graviton.

In [71], the authors restricted their attention to quintessence and utilized the EFT of the *perturbations* around the accelerating background, as was done for inflation in [62]. This has the advantage that perturbations about nonlinear backgrounds can be considered, but the disadvantage that the acceleration of the background must be assumed *a priori*. Regardless, this type of approach is important when considering models beyond the linear regime, and in

[1]For a review of earlier work utilizing EFT methods to address the importance of high energy signatures on inflation we refer the reader to [64] and references within.

particular for models of modified gravity where recovering the predictions of general relativity and consistency with solar system tests requires the EFT of the background to ultimately fail – e.g. in regions of high density leading to a screening mechanism e.g. [72, 73, 74].

In addition to the EFT background approach, one may also consider imposing symmetries on nonlinear backgrounds to retain a well defined Cauchy problem. In the EFT approach, this is never a concern since for energies below the cutoff of the theory, the number of degrees of freedom remains fixed, and higher time derivatives never appear in the equations of motion [65]. However, as shown long ago by Horndeski [75], by restricting the operators to be considered in the action it is possible to construct nonlinear backgrounds that give rise to only two derivatives acting on fields at the level of the equations of motion. These models are less general than the EFT approach, but in addition to being able to capture nonlinearities they also exhibit interesting self-tuning properties. The authors of [76] recently studied these actions identifying four terms that are important for classifying these scalar-tensor theories. Given our EFT approach, these terms are captured at leading order by the action to be considered below, but the full nonlinear effects will not be captured.

A powerful approach to understanding the implications of a given theory is to find dynamical attractor solutions for cosmological evolution. These provide predictions of evolutionary trajectories that a theory will naturally tend towards, largely insensitive to assumptions about initial conditions. Dynamical attractor analyses have allowed inferences about the viability of dark energy theories, in the context of minimally coupled quintessence theories [77, 78], non-minimal couplings in the dark sector [79], and $f(R)$ theories [80], and see [81] for a rather comprehensive review of dynamical attractors in dark energy. There are ways to evade dynamical attractors, for example by choosing forms of self-interactions that, by construction, do not allow attractors [82]. While such selections provide a proof of principle, they explicitly require a fine-tuning by the specificity of their form, which the generality of dynamical attractors works to avoid.

In this chapter we consider the implications for dynamical attractors in the background expansion history of an effective theory of cosmic acceleration expressed in terms of the low-energy effective action proposed by Park, Watson, and Zurek [66] and Bloomfield and Flanagan [67]. Our results here apply strictly to the linear regime. There has been recent work looking at observational implication of the nonlinear EFT of perturbations [83, 84, 85].

In section 2.2 we outline the effective field theory action which we consider in the chapter and discuss the origins of the contributing terms and the resulting equations of motion. In section 2.3 we present dynamical attractor solutions for the components of the effective theory and consider the analytical and numerical implications for the background expansion history. In section 2.4 we outline the cosmological data sets we use to constrain the effective theory and summarize our results. We bring together our findings and discuss implications for future work in section 2.5.

2.2 Effective field theory for dark energy

Working in the Einstein frame, we consider the effective theory for the background with leading scalar and gravitational corrections [67, 66]

$$\begin{aligned} S &= \int d^4x\sqrt{-g}\left\{\frac{M_p^2}{2}R - \frac{1}{2}(\nabla\phi)^2 - V(\phi)\right\} \\ &\quad + \int d^4x\sqrt{-g}\left\{f_{\rm quartic}(\phi)(\nabla\phi)^4 + f_{\rm curv}(\phi)G^{\mu\nu}\nabla_\mu\phi\nabla_\nu\phi\right. \\ &\quad \left. + f_{\rm GB}(\phi)\left(R^2 - 4R^{\mu\nu}R_{\mu\nu} + R_{\mu\nu\sigma\rho}R^{\mu\nu\sigma\rho}\right)\right\} \\ &\quad + S_{\rm m}\left[\Omega(\phi,\nabla\phi)g_{\mu\nu}, \psi_{\rm m}\right] \end{aligned} \tag{2.2.1}$$

where $M_p = 1/\sqrt{8\pi G} = 2.43\times10^{18}$ GeV is the reduced Planck mass and ψ_m are the standard model and dark matter fields. The first line gives the leading order terms, a canonical scalar field with an arbitrary potential $V(\phi)$. The second line gives the leading derivative corrections: a quartic kinetic term and a direct coupling between the scalar gradient and the Einstein

tensor. The third line is a Gauss-Bonnet (GB) curvature term. The last line describes the nonminimally coupling between the scalar field and matter in the Einstein frame, with

$$\Omega(\phi, \nabla\phi) \;=\; e^{\alpha(\phi)} \left(1 + f_{\rm kin}(\phi)(\nabla\phi)^2\right) \tag{2.2.2}$$

where α is the leading order coupling and a term proportional to $f_{\rm kin}$ provides the next order correction. The coefficients $f_{\rm quart}$, $f_{\rm curv}$, $f_{\rm GB}$ and $f_{\rm kin}$, along with V and α, are all arbitrary functions of the scalar field. We note that this implies that the GB term is no longer a total derivative.

We focus here on terms in the effective theory that may influence cosmic evolution in the matter dominated and late time accelerative eras. We do not consider higher order corrections to the energy-momentum tensor, $T^{\mu}{}_{\nu} = \mathrm{diag}(-\rho, P, P, P)$ where ρ is the cosmic matter density and P is the isotropic pressure that can arise in the a general EFT. Specifically we neglect operators such as those proportional to $(T^{\mu}{}_{\mu})^2 = (-\rho + 3P)^2$ or $T^{\mu\nu}T_{\mu\nu} = (\rho^2 + 3P^2)$, since these types of corrections would most likely lead to effects at all times, and be particularly relevant in the high density regime during radiation domination.

The power of the EFT approach is that data from observations can be used to constrain the possible values of the parameters, while at the same time theoretical consistency places additional constraints to eliminate regions of the parameter space. As an example of the latter, it is well known that radiative stability of the scalar field for quintessence puts strong constraints on the form of the scalar potential [86]. While the coefficients in the action are arbitrary functions of the scalar field, it is useful to expand these functions in powers of the cutoff of the effective theory. The cutoff is a dimensionful scale that characterizes the higher energy, microscopic physics that has been integrated out as our observational interest passes to lower energy scales. For example, for the application to dark energy this scale could result from integrating out electrons. We note, that given the cosmological background is dynamic (characterized by the Hubble parameter, $H(t)$), this can lead to several scales besides the masses of heavy particles going into determining the effective cutoff(s) of the theory – see e.g.

[87]. Lacking a knowledge of the high energy completion here, in this chapter we will study the implications for each leading correction by expanding functions with time derivatives of the scalar scaled by powers of the Hubble scale, whereas the scalar field will be suppressed by powers of the Planck mass.

We emphasize that since we are considering the EFT of the background (not the perturbations) our expansion must always respect the hierarchical structure of the terms, i.e. higher order corrections must always be sub-leading to lower order terms. This is particularly important to keep in mind in regards to the GB term, as this type of term is often considered with a large pre-factor, which can lead to a number of instabilities[2]. Here we will follow the EFT approach and treat the GB term as the first in a serious of higher derivative corrections. Indeed, the procedure followed in [66, 67] for arriving at the general action (2.2.1) requires that this term remain small for the reduction procedure that was implemented there to be valid. We also emphasize that the presence of the scalar dependent coefficient $f_{\rm GB}$ implies that the GB term is *not* purely topological and so can play an important role in the dynamics.

Our cutoffs, chosen to scale with powers of the Hubble and Planck scales, represent the most optimistic case for observations, and therefore the strongest constraints for theories. For larger cutoffs the observational effects of higher dimensional operators for dark energy and modified gravity are known to be negligible. Models of ghost condensation offer an example, where there the cutoff is typically taken to be of order a few GeV, and so the evolution is indistinguishable from a cosmological constant [88]. For the EFT of quintessence, a GeV scale cutoff implies a similar story, and all models remain observationally indistinguishable from ordinary, vanilla quintessence. Thus, here we focus on the lowest possible cutoff consistent with the effective theory, leaving the important question of the UV completion to future work.

Given these considerations we take the couplings to terms involving scalar gradients to be

[2]For a discussion of the pathologies associated with large GB terms and the difference with the EFT approach we refer the reader to [65].

of the form:

$$f_{\rm quart} = \frac{F_q}{M_p^2 H^2} \tag{2.2.3}$$

$$f_{\rm curv} = \frac{F_c}{H^2} \tag{2.2.4}$$

$$f_{\rm kin} = \frac{F_k}{M_p^2 H^2} \tag{2.2.5}$$

where F_q, F_c, F_k are constants. Following common examples from the literature, we assume exponential couplings and potentials for the interactions not involving scalar gradients,

$$V = V_0 \exp\left(-\lambda \frac{\phi}{M_p}\right) \tag{2.2.6}$$

$$e^{\alpha} = \exp\left(-2Q \frac{\phi}{M_p}\right) \tag{2.2.7}$$

$$f_{\rm GB} = F_0 \exp\left(\mu \frac{\phi}{M_p}\right) \tag{2.2.8}$$

with V_0, λ, Q, F_0 and μ constant. Our definitions of λ, μ and Q are chosen to be consistent with previous work, such as [77, 89], and $Q = \sqrt{2/3}C$ in [79]. While we consider an exponential potential in this analysis, power law potentials are also commonly considered, and though the findings differ in the details, typically they yield broadly comparable results in relation to the constraints on the coupling Q, e.g. [79, 90].

The equations of motion

We assume a FRW metric,

$$ds^2 = -dt^2 + a^2 dx^2 \tag{2.2.9}$$

where t is physical time and a is the scale factor and $H = \dot{a}/a$. Given a homogeneous scalar field, the Einstein field equations and energy-momentum conservation equations for the scalar and matter give rise to consistent general equations of motion given by the Friedmann equation,

$$\begin{aligned} 3M_p^2 H^2 = {} & \rho_m(\phi) + \rho_\gamma + \frac{1}{2}\dot{\phi}^2 + V(\phi) + 3f_{\rm quart}\dot{\phi}^4 \\ & + 9f_{\rm curv} H^2 \dot{\phi}^2 + 24\dot{\phi} f'_{\rm GB} H^3, \end{aligned} \tag{2.2.10}$$

the acceleration equation,

$$\begin{aligned} -3 \quad M_p^2 H^2 & \left[\frac{2}{3}\frac{\dot{H}}{H^2}\left(1 - f_{\rm curv}\frac{\dot{\phi}^2}{M_p^2}\right) + 1\right] \\ &= \frac{1}{3}\rho_\gamma + \frac{1}{2}\dot{\phi}^2 - V(\phi) + f_{\rm quart}\dot{\phi}^4 \\ &- f_{\rm curv}(3H^2\dot{\phi}^2 + 4H\dot{\phi}\ddot{\phi}) - 2f'_{\rm curv}H\dot{\phi}^3 \\ &- 8H^3 f'_{\rm GB}\dot{\phi}\left(\frac{f''_{\rm GB}\dot{\phi}}{f'_{\rm GB}H} + \frac{\ddot{\phi}}{\dot{\phi}H} + 2\frac{\dot{H}}{H^2} + 2\right), \end{aligned} \tag{2.2.11}$$

the scalar field equation,

$$\begin{aligned} &(1 + 12f_{\rm quart}\dot{\phi}^2)\ddot{\phi} + \left(3 + 12f_{\rm quart}\dot{\phi}^2\right)H\dot{\phi} + V' = \\ &\rho_m\left(\frac{Q}{M_p} + \frac{f'_{\rm kin}\dot{\phi}^2 + 2f_{\rm kin}\ddot{\phi}}{2(1 - f_{\rm kin}\dot{\phi}^2)}\right) - 3f'_{\rm quart}\dot{\phi}^4 \\ &-24f'_{\rm GB}H^4\left(\frac{\dot{H}}{H^2} + 1\right) \\ &-f_{\rm curv}(6H^2\ddot{\phi} + 12H\dot{H}\dot{\phi} + 18H^3\dot{\phi}) - 3f'_{\rm curv}H^2\dot{\phi}^2, \end{aligned} \tag{2.2.12}$$

and the matter fluid equation,

$$\begin{aligned} \dot{\rho} \quad &= \quad -3H(\rho + P) \\ &\quad - \left(\frac{Q}{M_p}\dot{\phi} + \frac{f'_{\rm kin}\dot{\phi}^3 + 2f_{\rm kin}\dot{\phi}\ddot{\phi}}{2(1 - f_{\rm kin}\dot{\phi}^2)}\right)(\rho - 3P), \end{aligned} \tag{2.2.13}$$

where primes denote derivatives with respect to the scalar field and dots denote derivatives with respect to physical time. ρ and P are functions of ϕ through Q and $f_{\rm kin}$, unless conformally coupled.

While it is convenient to perform the dynamical attractor analysis in the Einstein frame, comparisons with observations are performed in the Jordan frame, as typically cosmological redshifts in data assume baryonic matter is minimally coupled, and not subject to fifth forces due to a direct scalar coupling. To transform into the Jordan frame we use the conformal transformation to remove the coupling Ω from the metric, with $\tilde{g}_{\mu\nu} = \Omega g_{\mu\nu}$, $d\tilde{t} = \Omega^{-1/2}dt$, $\tilde{a} = \Omega^{-1/2}a$ and matter variables transforming as $\tilde{P} = \Omega^{-2}P$, and $\tilde{\rho} = \Omega^{-2}\rho$, where tildes denote Jordan frame variables.

2.3 Dynamical Attractor Solutions

In this section we use the background equations of motion to look for the stationary "attractor" solutions during the matter and late time accelerative eras. We will consider the impact of the higher order operators arising in the effective field theory on the cosmological dynamics compared with the behavior predicted by the leading order action.

I Leading order terms

The standard dynamical solutions for a nonminimally coupled, canonical scalar field [77, 78, 81] are commonly written using dimensionless variables, see for example [81],

$$x = \frac{1}{M_p H}\frac{\dot{\phi}}{\sqrt{6}}, \quad y = \frac{1}{M_p H}\frac{\sqrt{V}}{\sqrt{3}}, \quad z = \frac{1}{M_p H}\frac{\sqrt{\rho_\gamma}}{\sqrt{3}}. \tag{2.3.1}$$

The Friedmann equation gives the fractional matter density, Ω_m, in terms of these variables

$$\Omega_m(a) = \frac{\rho_m}{3M_p^2 H^2} = 1 - x^2 - y^2 - z^2. \tag{2.3.2}$$

The acceleration equation gives the effective Einstein frame equation of state parameter, w_E,

$$-\frac{\dot{H}}{H^2} = \frac{3}{2}(1 + w_E) = \frac{3}{2}\left(1 + x^2 - y^2 + \frac{1}{3}z^2\right), \tag{2.3.3}$$

and an effective scalar equation of state parameter,

$$w_\phi = \frac{w_E - \frac{1}{3}z^2}{x^2 + y^2} = \frac{x^2 - y^2}{x^2 + y^2}. \tag{2.3.4}$$

The scalar and matter fluid equations give the evolution for x, y, and z,

$$\frac{dx}{d\ln a} = -x\left(3 + \frac{\dot{H}}{H^2}\right) + \frac{\sqrt{6}}{2}\lambda y^2 + \frac{\sqrt{6}}{2}Q\Omega_m(a), \tag{2.3.5}$$

$$\frac{dy}{d\ln a} = -y\left(\frac{\sqrt{6}}{2}\lambda x + \frac{\dot{H}}{H^2}\right), \tag{2.3.6}$$

$$\frac{dz}{d\ln a} = -z\left(2 + \frac{\dot{H}}{H^2}\right). \tag{2.3.7}$$

The dynamical attractors are given by the static solutions to these equations $dx/d\ln a = dy/d\ln a = dz/d\ln a = 0$.

We can write a general expression for the effective Jordan equation of state, w_J, during attractor-driven epochs, in terms of the coupling and w_E, using the conformal transformation,

$$3(1+w_J) \;=\; \frac{3(1+w_E)-2\sqrt{6}Qx}{1-\sqrt{6}Qx}, \tag{2.3.8}$$

where x is the fractional scalar kinetic energy component in the attractor regime. This relationship holds true even when the nonrelativistic matter density, and its effect on the fluid equations, is negligible, and is well defined as long as $x \neq 1/\sqrt{6}Q$.

Two primary matter era attractor solutions arise: one dependent on the potential (MAT-λ), and one wholly determined by the non-minimal coupling (MAT-Q). A single potential-driven late time accelerative attractor exists (ACC-λ).

Attractor	x	y	Ω_ϕ	w_ϕ	w_E	w_J
RAD-λ	$\frac{2\sqrt{6}}{3\lambda}$	$\frac{2\sqrt{3}}{3\lambda}$	$\frac{4}{\lambda^2}$	$1/3$	$1/3$	$\frac{1}{3}\frac{(\lambda+4Q)}{(\lambda-4Q)}$
RAD-null	0	0	0	–	$1/3$	$1/3$
MAT-λ	$\sqrt{\frac{3}{2}}\frac{1}{\lambda-Q}$	$\frac{\sqrt{\frac{3}{2}-Q(\lambda-Q)}}{\lambda-Q}$	$\frac{3}{(\lambda-Q)^2}-\frac{Q}{\lambda-Q}$	$\frac{Q(\lambda-Q)}{Q(\lambda-Q)-3}$	$\frac{Q}{\lambda-Q}$	$\frac{2Q}{\lambda-4Q}$
MAT-Q	$\sqrt{\frac{2}{3}}Q$	0	$\frac{2Q^2}{3}$	1	$\frac{2Q^2}{3}$	$\frac{4Q^2}{3(1-2Q^2)}$
ACC-λ	$\frac{\lambda}{\sqrt{6}}$	$\sqrt{1-\frac{\lambda^2}{6}}$	1	$-1+\frac{\lambda^2}{3}$	$-1+\frac{\lambda^2}{3}$	$-1+\frac{\lambda(\lambda-2Q)}{3(1-Q\lambda)}$

Table 1: Table summarizing the properties of the principal dynamical attractors arising from the leading order terms in the effective action. They consist of two radiation era attractors, RAD-λ and RAD-null, two matter era attractors, MAT-λ and MAT-Q, and one accelerative era attractor, ACC-λ. We give the values of the dimensionless scalar field dynamical variables, x and y, the Einstein frame fractional energy density, Ω_ϕ and equation of state, w_ϕ, for the scalar field, and the overall effective equation of state in the Einstein, w_E, and Jordan frame, w_J.

For a minimal coupled scalar field, when $Q = 0$, the MAT-λ attractor is the main cosmological scaling solution [77, 78]. In this case, the scalar field evolves with the same

equation of state, w, as the dominant matter component, with the attractive property that the radiation and matter dominated eras evolve as in ΛCDM. To satisfy this scaling solution the scalar must be subdominant, $\Omega_\phi < \Omega_m$ requiring $\lambda > \sqrt{6}$. Nucleosynthesis puts a stronger lower bound on λ in the RAD-λ attractor; the non-zero scalar density increases the expansion rate, altering the primordial abundances. For example [91] reported a dark energy density of $\Omega_\phi < 0.09$ which translates into the constraint $\lambda > 6.5$. One cannot, however, simultaneously realize a cosmological solution that flows from this matter era attractor to an accelerative expansion at late times, as acceleration with the ACC-λ attractor requires $\lambda < \sqrt{2}$. A simple exponential dark energy model cannot provide a viable matter and accelerative era without a degree of freedom, such as a double potential or a feature in the potential [92].

In the nonminimally coupled scenario, an alternative matter era attractor, MAT-Q, is also present. The benefit of this attractor is that it can arise from the RAD-null attractor, evading the BBN constraints on λ, and transition to an accelerative ACC-λ attractor at late times (for appropriate choice of λ). It runs into problems observationally, however, because during the matter era $w_J \neq 0$. This was first highlighted in the context of $f(R)$ theories [80], for which $Q = 1/\sqrt{6}$, $w_E = 1/9$ and $w_J = 1/3$ during the matter dominated era, showing that dynamical attractors for such theories are inconsistent with data. The MAT-λ attractor also deviates from the dominant background equation of state when $Q = 0$, putting it in tension with data.

The accelerative expansion, in ACC-λ is enhanced as Q is increased for $0 < Q < 1/\lambda$, or $Q > (3-\lambda^2)/\lambda$ for $\lambda < \sqrt{2}$. In the case $\lambda > \sqrt{3}$ the coupling Q must be larger than $Q > 1/\lambda$. This could expand the range of λ that can give rise to acceleration.

II Gauss-Bonnet term

If uncoupled to the scalar, the Gauss-Bonnet (GB) term is a topological term which would play no role in the cosmic dynamics. If coupled, however, it will impact the expansion history

[89, 93].

We introduce an extra dimensionless variable for the GB term

$$v \equiv \frac{8 f'_{\rm GB} H^2}{M_p}. \tag{2.3.9}$$

The modified Friedmann equation (2.2.10) yields a matter density

$$\Omega_m(a) = 1 - x^2 - y^2 - z^2 - \sqrt{6} x v \tag{2.3.10}$$

and the acceleration equation gives

$$\begin{aligned} -\frac{2}{3}\frac{\dot{H}}{H^2}\left[1 - v\left(\sqrt{6}x - \frac{3}{2}v\right)\right] &= 1 + \frac{1}{3}z^2 + x^2 - y^2 \\ &\quad -v\left(\lambda y^2 + Q\Omega_m(a) + 2\mu x^2 - v - \sqrt{\frac{2}{3}}x\right). \end{aligned} \tag{2.3.11}$$

The fluid equations for y and z have the same forms as in (2.3.6) and (2.3.7), while the dynamical equation for the kinetic term, x, and the GB term are given by

$$\begin{aligned} \frac{dx}{d\ln a} &= -x\left(3 + \frac{\dot{H}}{H^2}\right) \\ &\quad + \frac{\sqrt{6}}{2}\left[\lambda y^2 + Q\Omega_m(a) - v\left(1 + \frac{\dot{H}}{H^2}\right)\right], \end{aligned} \tag{2.3.12}$$

$$\frac{dv}{d\ln a} = 2v\left(\frac{\sqrt{6}}{2}\mu x + \frac{\dot{H}}{H^2}\right). \tag{2.3.13}$$

The matter dominated era allows static solutions with $v = 0$, so that the GB term is negligible and attractors are the same for the leading terms: MAT-λ and MAT-Q given in Table 1. The difference in including the GB term occurs in the late time accelerative era. An alternative attractor exists, which is independent of the coupling Q, given by

Attractor	x	y	v	Ω_ϕ	w_ϕ	w_E	w_J
ACC-GB	0	1	λ	1	-1	-1	-1

.

This allows cosmological evolution following the MAT-λ, with a scaling attractor in the matter dominated era, to transition to a Gauss-Bonnet induced, de-Sitter solution at late

times. Note that the accelerative era arises because the gradient in the GB term becomes comparable, and opposite to that of the potential, however the energy density in the GB term, given by $\sqrt{6}xv$, tends to zero in both the matter and de-Sitter epochs.

At late times $v = \lambda$, $y = 1$, and $x = 0$, and ϕ is constant. The time at which the transition from the matter dominated to accelerative era occurs depends on the relative importance of the potential, V_0, and Gauss-Bonnet term, F_0, in the scalar field equation. We can obtain an approximate relationship between the two by assuming the accelerative attractor is reached today, with $H = H_0$, [93],

$$v = \lambda \approx 8 f'_{\rm GB} \frac{H_0^2}{M_p} \mid_{\phi=\phi_0} = \frac{-8 F_0 \mu H_0^2}{M_p^2} \exp\left(-\frac{\mu \phi_0}{M_p}\right), \tag{2.3.14}$$

$$y = 1 \approx \frac{V_0}{3 M_p^2 H_0^2} \exp\left(-\lambda \frac{\phi_0}{M_p}\right). \tag{2.3.15}$$

This gives an approximate relation to estimate the value of F_0 required to give acceleration today, in terms of the potential,

$$F_0^{est} = \frac{\lambda M_p^2}{8 \mu H_0^2} \left(\frac{3 M_p^2 H_0^2}{V_0}\right)^{\mu/\lambda}. \tag{2.3.16}$$

This relation is only a rough estimate, as the transition occurs prior to today and we have not yet reached the pure accelerative era. It gives a sufficiently good starting point, however, to guide a nuisance parameter in the MCMC analysis as discussed in 2.4.I.

III Quartic term

We now consider the implications of an additional quartic term $f_{\rm quart}\dot{\phi}^4$ in the action, with the coupling $f_{\rm quart}$ parametrized as in (2.2.3). The Friedmann equation gives the fractional matter density, Ω_m, in terms of these variables

$$\Omega_m(a) = 1 - x^2 - y^2 - z^2 - 36 F_q x^4. \tag{2.3.17}$$

The acceleration equation becomes

$$-\frac{\dot{H}}{H^2} = \frac{3}{2}\left[1 + x^2 - y^2 + \frac{1}{3}z^2 + 12 F_q x^4\right], \tag{2.3.18}$$

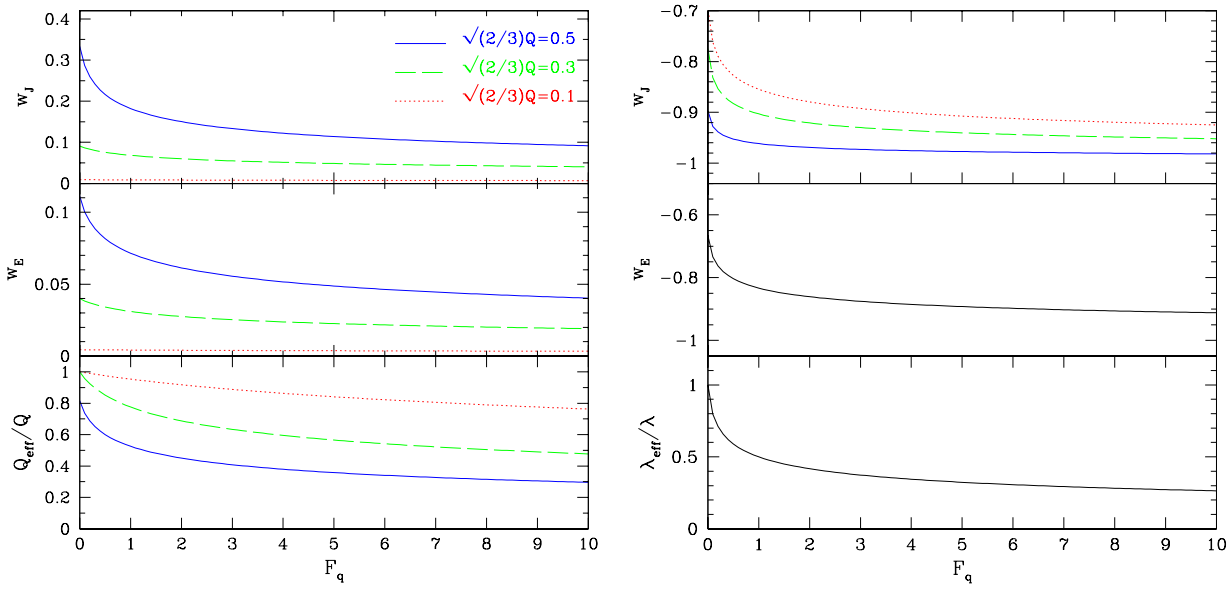

Figure 1: The implications of the attractor solutions in the matter-dominated (left panel) and accelerative (right panel) eras when the leading order terms in the action are augmented by the quartic kinetic term parametrized by an amplitude F_q. The panels show (top) the effective equations of state in the Jordan frame, w_J, and (middle) the Einstein frame, w_E along with (bottom) the effective coupling $Q_{\rm eff}$ (right) and potential exponent $\lambda_{\rm eff}$ (left), relative to their fiducial values. Three values of non-minimal couplings $\sqrt{3/2}Q = 0.1, 0.3, 0.5$ are considered. During the accelerative era Q only affects the conformal transformation and Jordan frame equation of state.

with an effective, overall equation of state

$$w_E \;=\; x^2 - y^2 + \frac{1}{3}z^2 + 12F_q x^4. \tag{2.3.19}$$

The fluid equations for y and z have the same forms as in (2.3.6) and (2.3.7), while the dynamical equation for the kinetic term, x, is given by

$$\begin{aligned}(1+72F_q x^2)x' \;&=\; -x\left(3 + (1+36x^2F_q)\frac{\dot{H}}{H^2} + 72F_q x^2\right)\\ &\quad + \frac{\sqrt{6}}{2}\lambda y^2 + \frac{\sqrt{6}}{2}Q\Omega_m(a).\end{aligned} \tag{2.3.20}$$

The RAD-null solution during the radiation dominated era is unchanged. For the RAD$-\lambda$ scaling solution z is changed to $z = \frac{\sqrt{\lambda^4 - 4\lambda^2 - 256F_q}}{\lambda^2}$; however, this just represents an adjustment of the relative contributions of Ω_γ and Ω_ϕ that keeps the effective equation of state unaltered,

$w_E = \frac{1}{3}$. The same is true for the MAT$-\lambda$ scaling, the solution for y is altered but $w_E = \frac{Q}{\lambda - Q}$ is unchanged.

The coupling in the matter dominated era still admits the MAT-Q attractor, but with a coupling that is dependent on both Q and F_q.

Considering all the terms in $x' = 0$, one finds a matter attractor solution, $x_{\rm MAT}$, that differs from the leading case

$$\begin{aligned} 0 &= 1296F_q^2 x_{\rm MAT}^7 + 144F_q x_{\rm MAT}^5 - 36\sqrt{6}QF_q x_{\rm MAT}^4 \\ &\quad +3(1-12F_q)x_{\rm MAT}^3 - \sqrt{6}Qx_{\rm MAT}^2 - 3x_{\rm MAT} + \sqrt{6}Q. \end{aligned} \tag{2.3.21}$$

We can define an effective coupling strength, $Q_{\rm eff}$, based on this attractor solution which would yield the same equation of state in the absence of the quartic term,

$$Q_{\rm eff} = \sqrt{\frac{3}{2}} x_{\rm MAT}(Q, F_q). \tag{2.3.22}$$

The Einstein frame effective equation of state during the MAT-Q attractor is

$$w_E = \frac{2}{3}Q_{\rm eff}^2(1 + 8F_q Q_{\rm eff}^2). \tag{2.3.23}$$

While the non-minimal coupling, Q, in essence, speeds up the scalar's evolution, and increases w_E, the quartic term, F_q, has the opposite effect, acting as a resistive force on the scalar and suppressing the kinetic fractional energy density in the MAT era , $x_{\rm MAT}$. The effective equations of state in both the Einstein and Jordan frames are brought closer to $w = 0$ as F_q increases. In theory, therefore, this quartic coupling might lessen the tension between nonminimally coupled attractor solutions and constraints on the matter dominated era evolution from CMB distance measurements.

In the accelerative era $y^2 = 1 - x^2 - 36F_q x^4$, and the attractor solution satisfies

$$24F_q x_{\rm ACC}^4 + x_{\rm ACC}^2 - \frac{1}{\sqrt{6}}\lambda x_{\rm ACC} = 0. \tag{2.3.24}$$

We can define an effective potential parameter, $\lambda_{\rm eff}$, that would give rise to the same dynamics in the absence of the quartic coupling,

$$\lambda_{\rm eff} = \sqrt{6} x_{\rm ACC}(F_q) \tag{2.3.25}$$

The Einstein frame effective equation of state

$$w_E = -1 + \frac{1}{3}\lambda_{\rm eff}^2(1 + 4F_q\lambda_{\rm eff}^2) \tag{2.3.26}$$

As we see in Figure 1, the effect of an increasing quartic coupling is to reduce the effective equation of state at late times relative to the standard ACC-λ value of $w = -1 + \lambda^2/3$. We can see this consistently in the analytic solutions in the limit of small F_q for the effective equation of state in the Einstein frame

$$w_E \approx -1 + \frac{\lambda^2}{3} - \frac{4\lambda^4 F_q}{3} + \ldots, \tag{2.3.27}$$

and in the Jordan frame

$$w_J \approx -1 + \frac{\lambda(\lambda - 2Q)}{3(1 - Q\lambda)}\left(1 - \frac{4\lambda^2 F_q}{(1 - Q\lambda)} + \ldots\right). \tag{2.3.28}$$

This should allow a larger range of values for λ to be consistent with observations for $F_q > 0$.

IV Coupling to the Einstein tensor

The presence of a direct coupling of the scalar to the Einstein tensor, with an amplitude parametrized by F_c (2.2.4), modifies the Friedmann, acceleration and fluid equations:

$$\Omega_m(a) = 1 - (1 + 18F_c)x^2 - y^2 - z^2, \tag{2.3.29}$$

$$\begin{aligned} -\frac{2}{3}\frac{\dot{H}}{H^2}\left(1 + \frac{6F_c}{1 + 6F_c}(1 + 18F_c)x^2\right) &= 1 + (1 + 18F_c)x^2 \\ &\quad -y^2 + \frac{1}{3}z^2 - 4\frac{F_c}{1 + 6F_c}\sqrt{6}x\left[(Q\Omega_m + \lambda y^2)\right], \end{aligned} \tag{2.3.30}$$

and

$$x' = -3x - (1 + \frac{6F_c}{1+6F_c})x\frac{\dot{H}}{H^2} + \frac{\sqrt{6}}{2}\frac{1}{(1+6F_c)}\left[\lambda y^2 + Q\Omega_m(a)\right], \tag{2.3.31}$$

where $|F_c| < 1/18$ if the coupling to the Einstein tensor is to be subdominant to the canonical kinetic term.

While the new coupling does not introduce a new attractor, nor change the predictions for the RAD-λ or the MAT-λ attractor, it does modify the other two attractors from their nominal values, determined by the leading order terms.

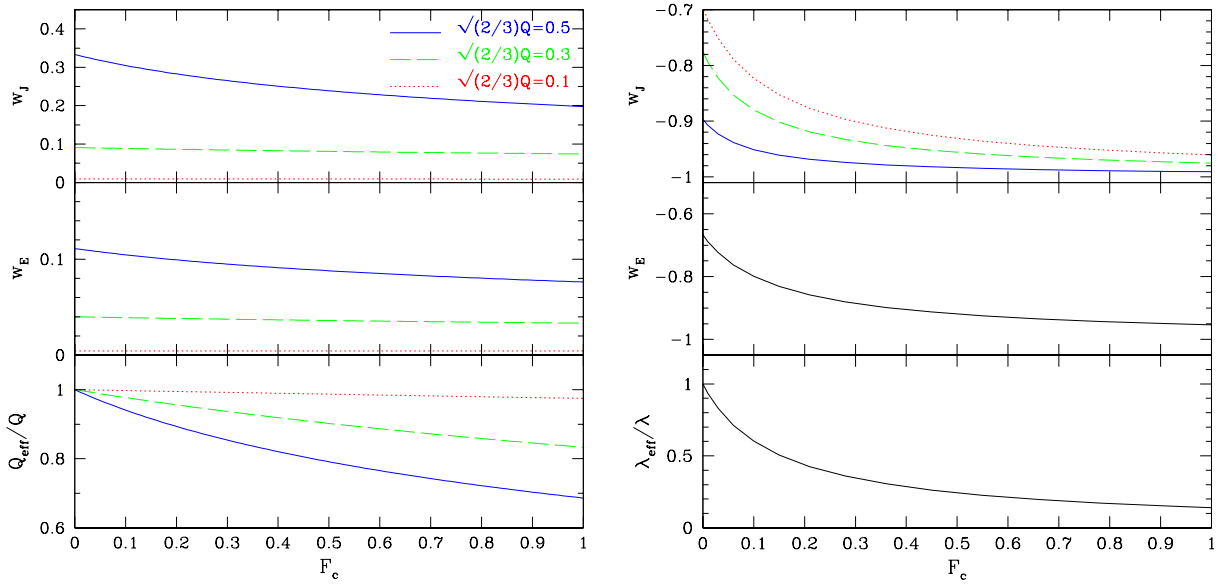

Figure 2: The implications of the attractor solutions in the matter-dominated (left panel) and accelerative (right panel) eras when the leading order terms in the action are augmented by a coupling to the Einstein tensor parametrized by an amplitude F_c. The panels show (top) the effective equations of state in the Jordan frame, w_J, and (middle) the Einstein frame, w_E, along with (bottom) the effective coupling $Q_{\rm eff}$ (right) and potential exponent $\lambda_{\rm eff}$ (left), relative to their fiducial values. Three values of non-minimal couplings $\sqrt{3/2}Q = 0.1, 0.3, 0.5$ are considered. During the accelerative era Q only affects the conformal transformation and Jordan frame equation of state.

The MAT-Q solution now satisfies,

$$\begin{aligned} 0 &= \sqrt{6}Q - 3x - \sqrt{6}Qx^2(1+24F_c) + (3+54F_c)x^3 \\ &\quad +6\sqrt{6}(1+18F_c)F_cQx^4, \end{aligned} \tag{2.3.32}$$

leading to the solution

$$\begin{aligned} x &= \frac{1}{12\sqrt{6}F_cQ}(-3+3\sqrt{1+16F_cQ^2}) \\ &\approx \frac{2}{3}Q\left(1-4F_cQ^2+\dots\right). \end{aligned} \tag{2.3.33}$$

the approximation holding for $F_c \ll 1$. The effective equation of state in the Einstein frame is reduced for $F_c > 0$,

$$\begin{aligned} w_E &= \frac{1}{12F_c}\left(-1+\sqrt{1+16F_cQ^2}\right) \\ &\approx \frac{2}{3}Q^2\left(1-4F_cQ^2+\dots\right) \end{aligned} \tag{2.3.34}$$

as it also is in the Jordan frame,

$$w_J = \frac{-1+4Q^2+\sqrt{1+16FcQ^2}}{3(1+2Fc-2Q^2)} \tag{2.3.35}$$

$$\approx \frac{4Q^2}{3(1-2Q^2)}\left(1+\frac{4Q^2F_c}{1-2Q^2}\right). \tag{2.3.36}$$

In the MAT $-\,\lambda$ solution, while the relative amplitudes of the kinetic and potential scalar densities are changed,

$$x = \sqrt{\frac{3}{2}}\frac{1}{(\lambda-Q)} \tag{2.3.37}$$

$$y = \frac{\sqrt{\frac{3}{2}-Q(\lambda-Q)\left(1+\frac{9F_c}{\lambda-Q}\right)}}{\lambda-Q}, \tag{2.3.38}$$

the effective equation of state is unchanged,

$$w_E = \frac{Q}{\lambda-Q}. \tag{2.3.39}$$

The late time accelerative attractor equation, with $y^2 = 1 - (1+18)x^2$ and $z = 0$, is

$$x' = -3x + \frac{\sqrt{6}}{2}\frac{\lambda}{1+6Fc} - 3\sqrt{6}\frac{F_c}{1+6F_c}\lambda x^2 \tag{2.3.40}$$

altering the ACC-λ solution

$$x = \frac{-1-6F_c+\sqrt{1+4F_c(3+9Fc+\lambda^2)}}{2\sqrt{6}F_c\lambda} \tag{2.3.41}$$

$$\approx \frac{\lambda}{\sqrt{6}}\left[1-6F_c\lambda\left(1+\frac{\lambda^2}{6}\right)\right]+\ldots. \tag{2.3.42}$$

For small F_c the effective accelerative equation of state is seen to become more negative for $F_c > 0$,

$$w_E \approx -1+\frac{\lambda^2}{3}\left[1-6F_c\left(1+\frac{\lambda^2}{6}\right)\right]+\ldots, \tag{2.3.43}$$

and

$$w_J \approx -1+\frac{\lambda(\lambda-2Q)}{3(1-Q\lambda)}\left(1-F_c\frac{(\lambda^2+6)}{(1-Q\lambda)}\right)+\ldots. \tag{2.3.44}$$

The numerical solutions are shown in Fig.2. For increasingly positive values of F_c the matter and accelerative era equations of state are lower, making them more consistent with data than $F_c = 0$. While we show the implications for $0 \le F_c \le 1$ here, in our analysis to follow we will impose a restriction that $|F_c| < 1/18$ to ensure the term remains subdominant to those at leading order.

V A kinetic non-minimal coupling

If we introduce a kinetic non-minimal coupling of the scalar field to matter, as in (2.2.5), the Friedman equation and acceleration equation in the Einstein frame are unchanged, however the scalar equation of motion is modified leading to a modified attractor equation:

$$x' + x\frac{\dot{H}}{H^2} = \frac{1-6F_kx^2}{1-6F_kx^2-3F_k\Omega_m} \times\left(-3x+\sqrt{\frac{3}{2}}\lambda y^2+\sqrt{\frac{3}{2}}\Omega_m Q-\frac{3f_{\rm kin}\Omega_m x}{(1-6F_kx^2)}\frac{\dot{H}}{H^2}\right). \tag{2.3.45}$$

This does not influence the effective equation of state in either the RAD-λ or the RAD-null era, and the leading order matter and accelerative era attractors are unmodified by the inclusion of $f_{\rm kin}$. Moreover, the conformal transformation can still be calculated via (2.3.8) since only derivatives of $f_{\rm kin}\dot{\phi}^2 = 6F_k x^2$ enter the equation which are zero for attractor solutions. The coupling does, however, open up additional matter and accelerative era attractor solutions, with $x = 1/\sqrt{6F_k}$. While we find that the numerical analyses do in some circumstances attempt to approach this attractor, the effect tends to be a transitory, then returning to the leading order attractors. In its limit this attractor would lead to an ill-defined and unphysical $\Omega = 0$ in the conformal transformation to the Jordan frame. Since the well-defined attractors are unmodified by this first order term, we do not investigate it further in the remainder of the chapter.

2.4 Comparison with Data

I Analysis Approach

To investigate the impacts of the leading order and first order terms in the EFT, we numerically evolve the Einstein frame Friedmann, acceleration and scalar field fluid equations, and simultaneously use the conformal transformation to calculate the Jordan frame variables. We compare the data to quantities in the Jordan frame since observations such as fluctuations in the CMB and the redshift of supernovae are reported assuming that the baryons are minimally coupled to gravity. We hence define the present day epoch as $a_J = 1$ and using the Jordan frame redshifts and distance measures as the physical observables.

To establish the cosmological constraints on the EFT parameters, we perform a MCMC analysis assuming flat priors on Ω_b, Ω_m, and H_0, along with leading order parameters V_0, λ, and Q. We consider constraints on the leading order terms plus each first order term separately to understand the individual effects of each. We assume flat priors on the quartic

coupling, $-10 \leq F_q \leq 10$, and the coupling to $G_{\mu\nu}$, $0 \leq F_c \leq 1/18$ where the upper limit ensures subdominance to the leading order terms. Scenarios with a Gauss-Bonnet term are investigated with exponent $0 \leq \mu \leq 70$ and magnitude given by $F_0 = p_{\rm GB} F_0^{\rm est}$, where $F_0^{\rm set}$ was defined in (2.3.16) and $-10 \leq \log p_{\rm GB} \leq 0$.

Our 1D and 2D constraints are obtained after marginalizing over the remaining parameters using the programs included in the publicly available *CosmoMC* package [3]. To ensure convergence we apply the Gelman and Rubin variance of chain meanmean of chain variances R statistic for each parameter on 8 or more chains. All MCMC runs have a convergence of $R < 0.1$ or lower.

We consider constraints from the "Union 2.1" compilation [4] of 580 Type Ia supernovae observations [94], with redshifts in the range $0 < z < 1.414$. We compare predicted distance modulus estimates for the MCMC scenarios for each supernovae, at redshift z, against the observations using the compilation's covariance matrix including systematic errors.

To investigate geometric constraints from the CMB, we use the WMAP-7 [11] results parametrized as outlined in section 1.3.I. We use the CMB data vector given in [11]

$$\begin{pmatrix} l_A \\ \mathcal{R} \\ z_* \end{pmatrix} = \begin{pmatrix} 302.09 \\ 1.725 \\ 1091.3 \end{pmatrix}$$

with the inverse covariance matrix

$$\mathrm{Cov}_{\rm CMB}^{-1} = \begin{pmatrix} 2.305 & 29.698 & -1.333 \\ & 6825.270 & -113.180 \\ & & 3.414 \end{pmatrix}.$$

[3] http://cosmologist.info
[4] http://supernova.lbl.gov/Union/

The redshift of decoupling, z_*, is obtained , to percent accuracy, from the fitting formula [95]

$$g_2 = \frac{0.560}{1 + 21.1(\Omega_b h^2)^{1.81}}, \tag{2.4.1}$$

$$g_1 = \frac{0.0783(\Omega_b h^2)^{-0.238}}{1 + 39.5(\Omega_b h^2)^{0.763}}, \tag{2.4.2}$$

$$z_* = 1048(1 + 0.00124(\Omega_b h^2)^{-0.738})(1 + g_1(\Omega_m h^2)^{g_2}). \tag{2.4.3}$$

where $h = H_0/100$ kms^{-1}Mpc^{-1}. In principle a non-minimal coupling, Q, will affect the the matter dominated expansion era and consequently the accuracy of the fitting function. We find that the redshift to decoupling z_* is only changed by 2×10^{-3} %, and the effects on l_A and $\mathcal{R}$ are smaller, so that the effect of the coupling on the accuracy fitting function in not a significant concern.

BAO are the imprint of the sound horizon at last scattering as a characteristic scale in the clustering of matter. When observed at different redshifts the characteristic scale can be used as a standard ruler to estimate cosmological distances.

The acoustic scale along the line of sight encodes information about the Hubble parameter H whereas the tangential component measures the angular diameter distance D_A. Current measurement accuracy is not sufficient to measure H_0 and D_A separately, so observational radial and tangential measurements are typically combined into an effective, averaged scale [96] defined as

$$D_v(z) = \left[\frac{D_A(z)^2(1+z)^2 cz}{H(z)}\right]^{1/3}. \tag{2.4.4}$$

The most accurate measurements of the BAO results to date come from the 2dF Galaxy Redshift Survey (2dFGRS), the Sloan Digital Sky Survey (SDSS) DR7, the WiggleZ Dark Energy Survey, and the Baryon Oscillation Spectroscopic Survey (BOSS). The results presented in [17] are based on the spectroscopic SDSS DR7 sample, including both LRG and Main galaxy samples in combination with the 2dFGRS survey. The ratio $r_s(z_{\rm drag})/D_v(z)$ is given for two redshifts, $z = 0.2$ and $z = 0.35$,

$$r_s(z_{\rm drag})/D_v(0.35) = 0.1094 \pm 0.033, \tag{2.4.5}$$

$$r_s(z_{\rm drag})/D_v(0.2) = 0.1980 \pm 0.0058 \tag{2.4.6}$$

(1σ errors), $z_{\rm drag}$ is the comoving sound horizon at the baryon drag epoch, baryon decouple from photons. If the ratio $3\rho_b/4\rho_\gamma = 1$ at z_* then the drag epoch and decoupling occur simultaneously. For typical, cosmological scenarios, however $z_* > z_{\rm drag}$. We calculate the redshift $z_{\rm drag}$ using the fitting formula from [97]:

$$\begin{aligned} z_d &= 1291\frac{(\Omega_m h^2)^{0.251}}{1+0.659(\Omega_m h^2)^{0.828}}[1+b_1(\Omega_b h^2)^b 2], && (2.4.7)\\ b_1 &= 0.313(\Omega_m h^2)^{0.419}[1+0.607(\Omega_m h^2)^{0.674}], && (2.4.8)\\ b_2 &= 0.238(\Omega_m h^2)^{0.223}, && (2.4.9) \end{aligned}$$

accurate to a few percent.

For $z = 0.35$ however, we are using the results of the updated analysis of the SDSS DR7 data by [98] yielding to $D_v/r_s = 8.88 \pm 0.17$.

As the distance scale D_v is highly degenerate with $\Omega_m h^2$ the WiggleZ survey introduced the acoustic parameter $A(z)$ [18],

$$A(z) = D_v(z)\sqrt{\Omega_m H_0^2}/cz. \tag{2.4.10}$$

The WiggleZ survey provides BAO measurements for three redshifts complementary to those from the SDSS/2dFGRS surveys: $A(0.44) = 0.474$, $A(0.6) = 0.442$, $A(0.73) = 0.424$. The inverse covariance matrix is given by

$$\mathrm{Cov}^{-1}_{\rm BAO:WiggleZ} = \begin{pmatrix} 1040.3 & -807.5 & 336.8 \\ & 3720.3 & -1551.9 \\ & & 2914.9 \end{pmatrix}.$$

Finally, we include the recent BOSS survey results, $D_v/r_s = 13.67 \pm 0.22$ at $z = 0.57$ [19].

In combination, the data sets have $589 - d$ degrees of freedom where d is the number of MCMC parameters. For ΛCDM $d = 3$, leading order $d = 6$ and all other model have $d = 7$.

II Findings

II.a Constraints on the leading order, quartic kinetic, and Einstein tensor terms

In Table 2 we summarize the results of the MCMC analysis for the EFT models involving only the leading order terms, and those in which a quartic coupling or a coupling to the Einstein tensor are present, in comparison to ΛCDM. These models modify the attractor behaviors in both the matter and accelerative eras. The minimum χ^2 is the same for each scenario, $\chi^2 = 547.6$, equivalent to that for ΛCDM, reflecting that in spite of including one or two extra parameters, these scenarios can recreate, but not improve upon, the predictions for ΛCDM.

Model	Ω_m	$\lvert Q\rvert$	$\lvert\lambda\rvert$
ΛCDM	$0.293^{+0.020}_{-0.019}$	—	—
+Q (leading order)	$0.299^{+0.025}_{-0.022}$	< 0.037	< 1.10
$+F_c$	$0.299^{+0.024}_{-0.022}$	< 0.037	< 1.32
$+F_q$	$0.300^{+0.024}_{-0.025}$	< 0.039	< 1.94

Table 2: Summary of the 95% confidence level constraints from the MCMC analysis for all scenarios except that including the Gauss-Bonnet term. The χ^2 for all models are the same as for ΛCDM=547.6

Scenarios with increasing magnitudes of coupling and exponential exponent come into tension with the data as they increase the predicted equation of state parameter in the matter era (for $Q \neq 0$) and the accelerative era (for $\lambda \neq 0$) relative to the ΛCDM prediction. In the minimally coupled scenario, one would require $\lambda < \sqrt{2}$ to achieve any acceleration (and $\lambda \ll \sqrt{2}$ to have $w \approx -1$). The presence of a non-minimal coupling, $Q < 1/\lambda$, creates a

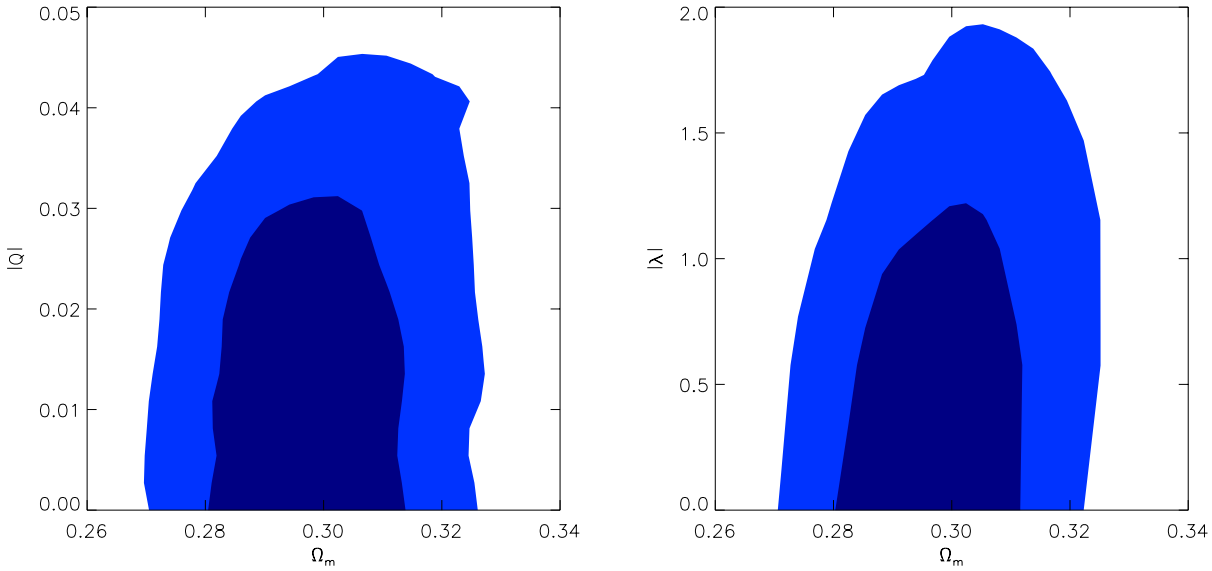

Figure 3: Joint 68% (dark shaded) and 95% (light shaded) constraints for the leading order action on the fractional matter density today, Ω_m, and the coupling of the scalar field to matter, Q, (left panel) and the scalar potential exponent, λ (right panel).

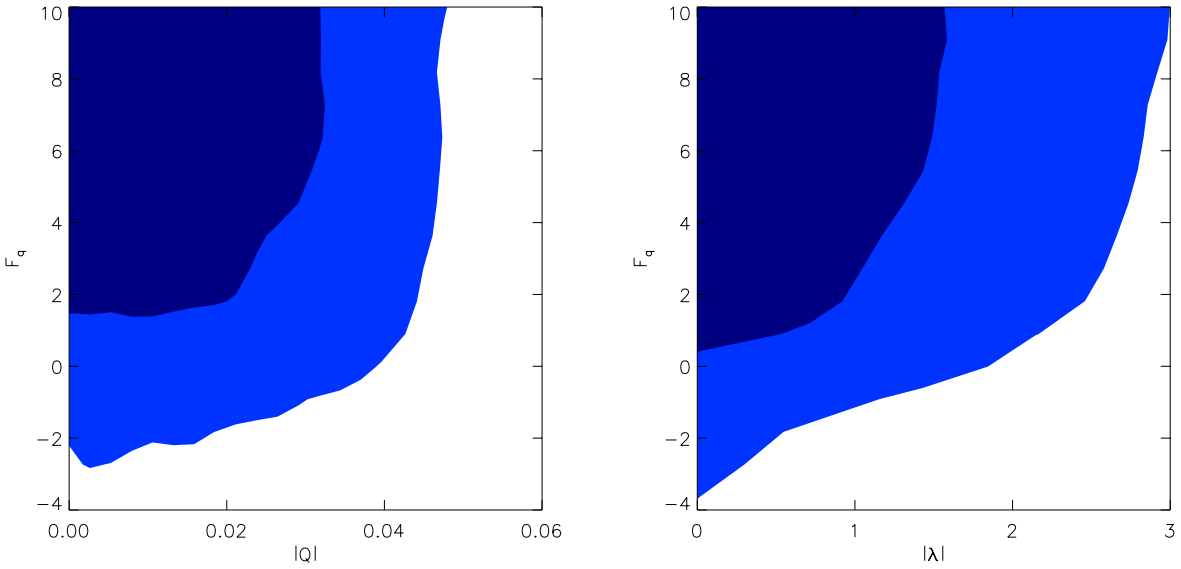

Figure 4: Joint 68% (dark shaded) and 95% (light shaded) constraints on the quartic kinetic coupling, F_q, and the coupling of the scalar field to matter, Q, (left panel) and the scalar potential exponent, λ (right panel). The quartic term has a significant effect on reducing the equation of state in the accelerative era, allowing a larger range of λ to be consistent with the data. The evolution is sensitive to the sign of F_q leading to a lower bound on the coupling.

more negative equation of state in the Jordan frame, allowing a larger range of λ, including potentially $\lambda > \sqrt{2}$, to be consistent with the data.

In Figure 3 we show the combined 2D constraints arising from CMB, BAO and SN for the coupling Q and the exponential exponent λ. We find 1D marginalized errors on the coupling of $|Q| < 0.021(0.037)$ and exponential potential, $\lambda < 0.70(1.10)$ at the 68% (95%) confidence level. In [79] a similar analysis was performed, but in the context of constraints arising from a non-minimal coupling purely to cold dark matter, for which the comparison with observations is performed in the Einstein frame. They found similar constraints of $|Q| < 0.055$ and exponential potential, $\lambda < 0.95$ at the 95% confidence level. The similarity can be understood in terms of the small values of Q; as the conformal transformation tends towards unity, the Einstein and Jordan frame become comparable.

As discussed in section 2.3, while the quartic kinetic term and the coupling to the Einstein tensor do not lead to new attractor solutions, they do alter the leading order attractor solutions during the matter dominated and accelerative eras. Their effects become less significant, however, as the coupling, Q, becomes smaller. We find that the constraints on Q are little changed by the inclusion of these terms as its magnitude is already tightly constrained, to be very small, by the data. During the accelerative era these terms have a more pronounced effect, and their enhancement of the accelerative equation of state allows a broader range of λ to be consistent with the data, as given in Table 2.

While the effects of Q and λ are sensitive to their magnitude, not sign, the quartic coupling term modification is sign dependent; negative values of F_q and F_c increase the effective equation of state during both the matter and accelerative eras. If the quartic term is included, we find the data provide a lower bound with $F_q > -0.62$ at the 95% confidence level, as shown in Figure 4. For the coupling to the Einstein tensor, we find no significant difference in best fit likelihoods in the range we investigated $0 \leq F_c \leq 1/18$.

II.b Constraints on the Gauss-Bonnet term

The Gauss-Bonnet term gives rise to a new accelerative attractor solution through creating a minimum in the effective scalar potential, produced by the exponential potential and the GB term. This enables the expansion history to exit the scaling solution during the matter dominated era into a stable de-Sitter point. The GB term does not affect the RAD or MAT era attractors, so we consider its impact on a simple nonminimally coupled quintessence model, with $Q = 0$.

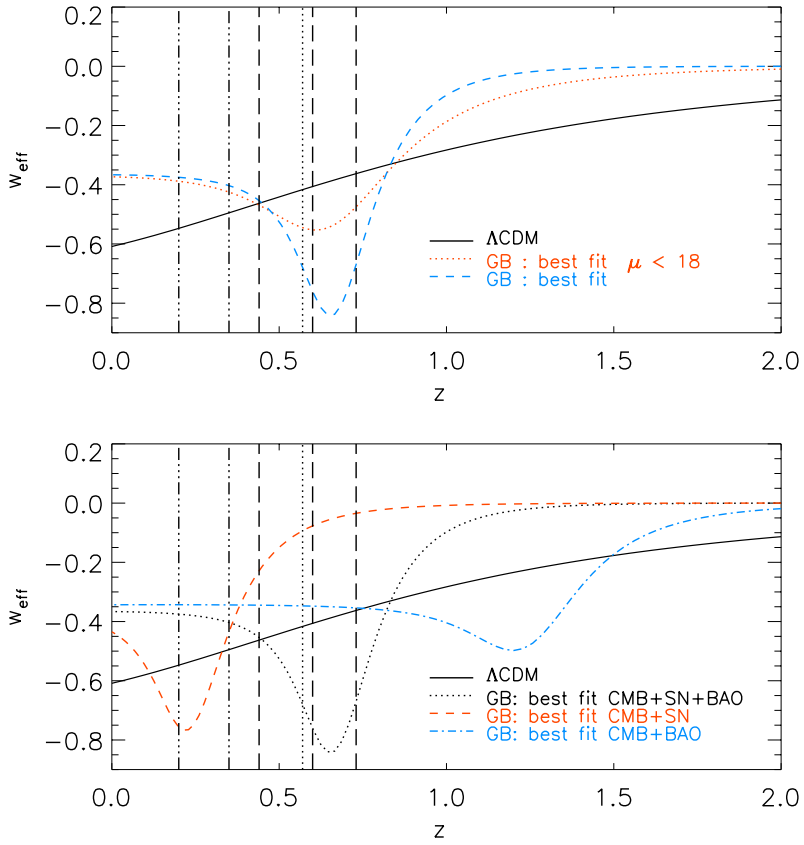

Figure 5: The effective equation of state, $w_{\rm eff}$, as a function of redshift, z,for the Gauss-Bonnet model in comparison to a best fit ΛCDM scenario (black solid). (Top panel) Comparison of the best fit prediction for the Gauss-Bonnet model overall (blue,dashed) and for models with a low value of the exponent, $\mu < 18$ (red dotted), showing how the depth of the "trough" in $w_{\rm eff}$ is dependent on μ. (Lower panel]) Comparison of the overall best fit for CMB+SN (blue, dot-dashed), CMB+BAO (red, dashed-dotted) and CMB+BAO+SN (black, dotted) showing the tension between the preferred evolution histories for the different data sets.

In this scenario our present day epoch is in the transition period between the matter and de-Sitter eras characterized by a trough [89] and plateau in the effective equation of state as shown in Figure 5. Prior to the transition the scalar follows the MAT-λ attractor with $w_{\rm eff} = 0$. At the transition epoch the positive gradient of the GB term temporarily dominates the field's equation of motion. The trough in the effective equation of state is generated as the scalar slows and instantaneously becomes static, then $\dot{\phi}$ changes sign, and the equation of state increases again. Following this the scalar proceeds on a slow evolution towards the static de-Sitter solution (in the distant future). Both before and after the trough, $w_{\rm eff}$ is greater than in ΛCDM scenarios.

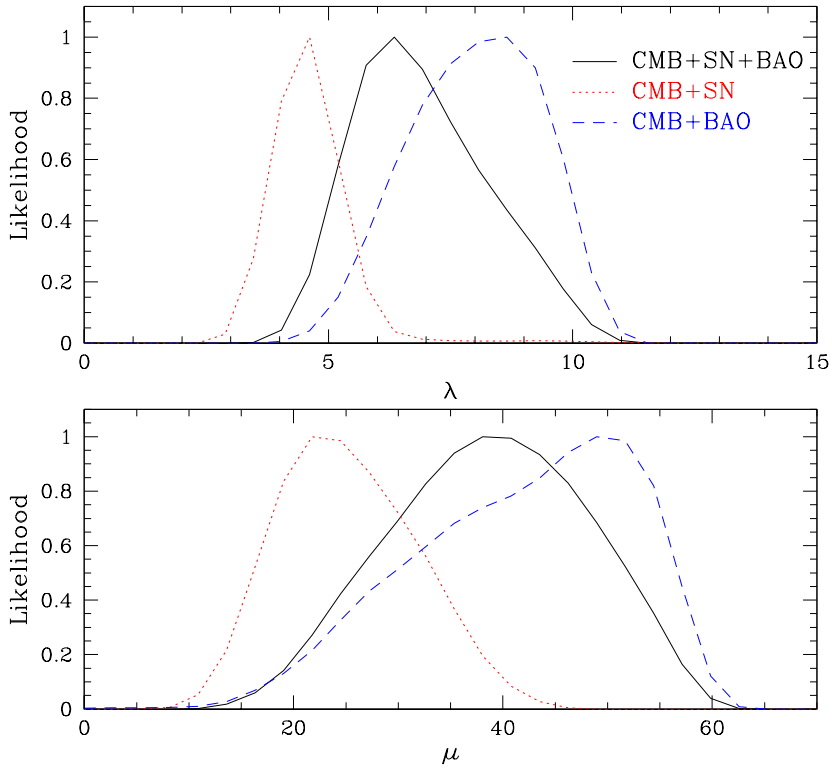

Figure 6: 1D likelihood contours for the Gauss-Bonnet parameter μ and the potential exponent λ for the different data sets: CMB+BAO+SN (black solid line), CMB+BAO (blue dashed line) and CMB+SN (red dotted line). There is a clear tension between the supernova and the BAO data sets. As discussed in the text, through their effects on $w_{\rm eff}$, the data provide both upper and lower bounds on λ and μ in this model.

We note that while in the matter and de-Sitter eras the fractional energy density in the GB term, $\Omega_{\rm GB} = \sqrt{6}xv$, tends to zero, it is non-zero and can be significant in this brief transition between the two. During this epoch therefore we are close to, if not at, the point, of no longer satisfying the subdominance criteria used to formulate the EFT action.

The depth of the trough is enhanced by a smaller value of λ (giving a larger kinetic energy during the MAT-λ phase), or steeper GB coupling, μ. Enhancing the depth of trough also reduces the duration of the transient feature, however, so that there is a sweet spot optimizing the trough's observational impact. The redshift position of the transient is degenerately sensitive to μ, λ, and V_0 through (2.3.16) and can be tuned through varying $p_{\rm GB}$.

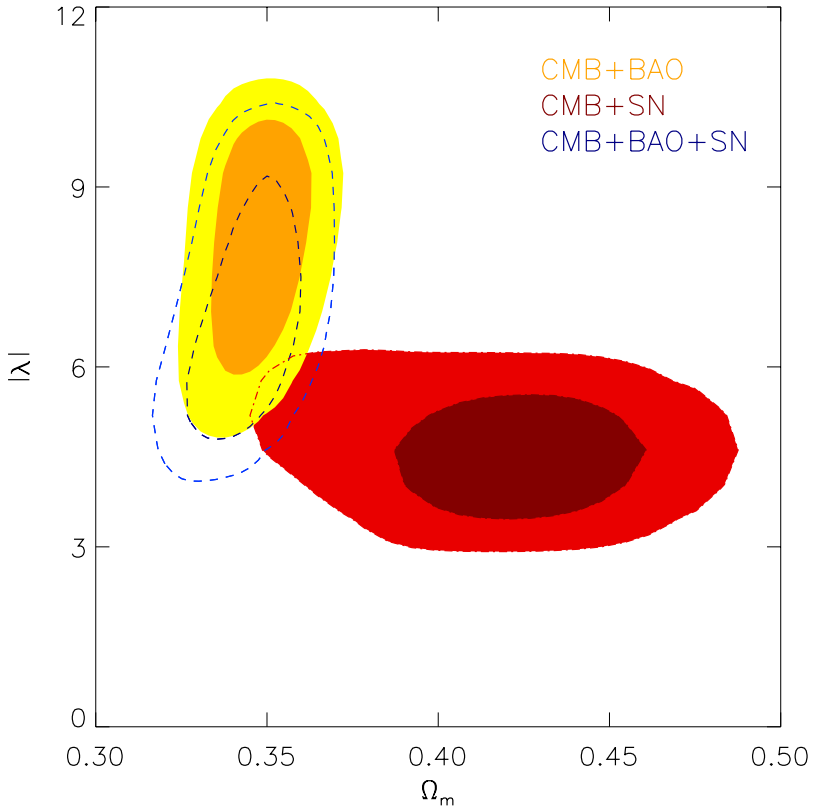

Figure 7: Joint 68% (dark shaded) and 95% (light shaded) constraints for the fraction matter density, Ω_m and for potential exponent λ in the Gauss-Bonnet model for the different data sets: CMB+SN (red solid contours), CMB+BAO (yellow solid contours), and in combination CMB+BAO+SN (blue dashed lines). There CMB+SN and CMB+BAO data have almost orthogonal dependencies in this projection, highlighting the origins of the tension between them.

As summarized in Table 3, we find that this distinctive equation of state profile is well constrained by the BAO and SN data, allowing us to place constraints on μ, λ, and $p_{\rm GB}$, and the contribution of the GB term in this effective action.

In Figure 6 we show the tension between the constraints from CMB+SN and CMB+BAO in terms of the exponents μ and λ and Ω_m. We find the SN data have the strong preference for the GB trough to be located around z ∼0.2-0.3, where previous principal component analyses of SN have shown the best measured modes in $w_{\rm eff}$ are peaked [99]. The accelerative era starts somewhat later than in ΛCDM and corresponds to a significantly higher Ω_m. Values of λ ∼4-5 are preferred to create a trough that is deep but still sufficiently broad to make the redshift averaged effective equation of state as consistent with that for ΛCDM as possible. By contrast the BAO place tight constraints on the matter density today. The average equation of state in the low redshift regime is somewhat larger than that predicted in ΛCDM, which results in a comparatively higher Ω_m being preferred to fit the BAO data. This is consistent with the standard degeneracies found in BAO constraints of a constant equation of state, e.g. [18]. The BAO are less sensitive to shape and depth of the trough than the SN, and place weaker constraints on λ, μ and $p_{\rm GB}$.

A previous analysis of this scenario [93], only including the SDSS BAO survey, found reasonable agreement with the data when only considering CMB+BAO constraints. We find that when we also include the WiggleZ and BOSS data the combined fit is not good and both the CMB+SN and CMB+BAO yield a worse fit than ΛCDM. The major issue arises when trying to jointly fit SN and BAO data. In this case, the Gauss-Bonnet model fits the data significantly worse than ΛCDM, with a difference of χ^2(GB)-χ^2(ΛCDM)=19.8.

Data	ΛCDM		Gauss-Bonnet				
	χ^2	Ω_m	$\Delta\chi^2$	Ω_m	λ	μ	lg $p_{\rm GB}$
CMB+SN	545.3	$0.29^{+0.05}_{-0.05}$	2.8	$0.42^{+0.05}_{-0.06}$	$4.6^{+0.7}_{-0.5}$	25^{+10}_{-9}	$-1.7^{+0.5}_{-0.7}$
CMB+BAO	2.5	$0.29^{+0.02}_{-0.02}$	5.7	$0.35^{+0.02}_{-0.02}$	$8.0^{+1.8}_{-2.0}$	46^{+20}_{-21}	$-2.9^{+1.3}_{-1.2}$
CMB+BAO+SN	547.6	$0.29^{+0.02}_{-0.02}$	19.8	$0.34^{+0.02}_{-0.02}$	$6.9^{+2.4}_{-1.7}$	41^{+20}_{-16}	$-2.3^{+1.3}_{-1.6}$

Table 3: Summary of the 95% confidence level constraints from Gauss-Bonnet MCMC analysis. The SN data provide the best constraints on GB parameters μ and λ and $p_{\rm GB}$. There is significant tension between the constraints from SN and BAO data sets separately. The compromise, when the data sets are considered in combination, is a significantly worse fit to the data than ΛCDM.

2.5 Conclusions

We have considered the existence of dynamical attractor solutions in a general approach to dark energy model building, utilizing methods of effective field theory. A wide range of dark energy and modified gravity models are able to be described using this approach, so that it forms a useful phenomenological link between underlying theories and observations. Dynamical attractors are powerful because of their weak sensitivity to initial conditions, which helps to alleviate some of the fine-tunings required to make models observationally viable. This robustness can also be useful in determining constraints on the action of the effective theory and, in the presence of stark tensions with astrophysical observations, can help isolate terms which are strongly disfavored - helping focus model building efforts.

We considered both the analytical and numerical predictions for the cosmic expansion history and obtained numerical constraints on the effective theory in light of recent CMB, Type Ia SN and BAO constraints. In the Einstein frame attractor solutions exist that predict observationally consistent radiation (RAD-null) and accelerative eras (ACC-λ), but require tight constraints on the presence of a non-minimal coupling to matter,Q, to give a viable matter era evolution (MAT-Q). We have shown that the addition of terms which are quartic in the time derivative of the scalar field, scalar couplings to the Einstein tensor, and a

Gauss-Bonnet term can all lead to modifications of the expansion history in the matter and accelerative eras. The quartic and Einstein tensor terms both modify the existing attractor solutions, creating effective couplings and potential exponents $Q_{\rm eff}$ and $\lambda_{\rm eff}$ that can reduce the effective equation of state parameter in both eras, and improve the fit to the data. They have a limited impact on the constraints of Q in the matter era, because their effect is diminished when Q is small. They can, however, have a significant affect on expanding the range of potentials consistent with the data by increasing the range of λ allowed.

The Gauss-Bonnet coupling opens up a new late-time de-Sitter solution (ACC-GB) induced by the creation of a minimum in the effective potential formed from $V(\phi)$ and the GB term. In this scenario, our current epoch is a transitory era between matter domination and the de-Sitter phase, with a characteristic evolution in the equation of state parameter that is constrained well by the data. In particular, a tension exists between the BAO and Type Ia supernovae, through their different redshifts sensitivity, when fitting the GB model to the data. In combination they rule out this scenario at large significance, with a best fit $\chi^2({\rm GB}) - \chi^2(\Lambda{\rm CDM})$=19.8. This model, as well as being observationally disfavored, involves a transient epoch where the GB term becomes comparable with the leading order potential, so that on theoretical grounds one must also be cautious and ensure that the EFT remains valid.

The complementarity of the SN, BAO, and CMB distance measures, has enabled us to place constraints on the cosmological background evolution by constraining the EFT couplings of higher dimensional operators. Our general approach is limited to perturbatively constructed backgrounds and does not apply to models where the background evolution becomes strongly coupled or highly nonlinear. This means that we are unable to capture screening effects that could be an important additional signature for some models of modified gravity, as well as models such as k-essence where a perturbative description of the background is not possible. To utilize the EFT approach in these models, one must put aside the possibility of constraining the background evolution, and instead construct an effective theory for the perturbations

around an assumed ΛCDM-like background. Such an approach has already been taken for models of quintessence [71], where it was shown that instability issues - which are common place in such models - can be addressed within the context of the EFT. Further work will extend this approach in much the same spirit as here, but with an emphasis on constraining the EFT of the perturbations. This will extend our analysis of cosmological constraints to the EFT of the perturbations, and their implications for complementary constraints from LSS measurements of weak lensing, galaxy position, and peculiar velocity fields. These correlations, comparing and contrasting relativistic and nonrelativistic tracers, could be a powerful probe of the broad range of gravitational modifications described by the EFT [100].

Chapter 3

Constraints on gravity and dark energy from the pairwise kinematic Sunyaev-Zel'dovich effect

Contents

3.1 Introduction

Many alternatives to standard gravity have been proposed to explain the acceleration of the Universe, many of which can have interesting effects on the growth of structure on cosmic, cluster and galaxy scales. In particular clusters are highly affected by the underlying theory of gravity because of their density environments. Therefore the peculiar velocities of clusters provide an alternative, complementary measurement of gravity's influence on cosmic structure to the peculiar motions of individual galaxies [101, 102, 103, 104, 105, 106, 107, 108]. Considering these as part of a multiple tracer approach, in combination with other large scale structure (LSS) probes, will provide the clearest picture of gravity's properties.

Cluster motions leave a secondary imprint in the CMB known as the kinetic Sunyaev-Zel'dovich (kSZ) effect [47], the process of CMB photons passing through a cluster and being Doppler shifted due to the cluster's peculiar velocity relative to the CMB rest frame. This provides a potentially powerful measurement of the gravitational field. Despite its potential,however, the kSZ has been hard to measure; the signal is small when compared to the thermal SZ effect and emission from dusty galaxies, and doesn't have a distinct frequency dependence. Observational efforts to constrain the cluster peculiar velocities have come from multi-band photometry in combination with X-ray spectra [109, 110, 111, 112, 113] and spectroscopy around the thermal SZ null frequency [114]. Recent work extracted the kSZ signature from individual clusters by combining sub-mm, X-ray and subarcminute resolution CMB data to respectively remove dusty galaxy emission, estimate electron density and fit thermal and kinematic SZ templates [115]. Data from the *WMAP* and *Planck* satellites have been used to place upper limits on the bulk flows and statistical variation in cluster peculiar velocities [116, 117], while South Polar Telescope (SPT) data [16, 118] and Atacama Cosmology Telescope (ACT) data [119] have been used to place limits on the kSZ signal from the epoch of reionization.

Multi-band methods do not yet provide a practical approach to extract the kSZ signal from thousands of clusters as desired for large scale cosmological correlations. Cross-correlating arcminute resolution CMB maps with cluster positions and redshifts determined by a spectroscopic LSS survey can enable extraction of the pairwise kSZ signal [106, 107, 120]. Indeed, the first detection of the kSZ effect in the CMB spectrum was made by combining CMB measurements from the ACT [121] with the SDSS BOSS spectroscopic survey [52] to measure the mean pairwise momentum of clusters, using luminous red galaxies as a tracer for clusters [122]. The pairwise approach for extracting the kSZ signal measures the difference in peculiar velocities of nearby clusters as a function of the comoving distance between the clusters. This approach minimizes contributions from the CMB, thermal SZ, and foregrounds, which can be treated as approximately constant on these scales, and by averaging over many clusters pairs

any effects independent of the separation will cancel. CMB surveys such as ACTPol [123], SPTPol [124], Advanced ACTPol [125], SPT-3G [126], and a next-generation, so-called Stage IV CMB survey [40] in combination with overlapping galaxy surveys, such as those described above, can improve upon this detection and enable the use of mean pairwise velocities as a cosmological probe.

In this chapter, we study the constraints on dark energy and cosmic modifications to gravity expected from analyzing the mean pairwise velocity of clusters observed through the kSZ effect by upcoming CMB observations in combination with spectroscopic LSS redshift surveys. In section 3.2 the analytical formalism used to construct statistics and associated covariances for cluster velocity correlations is summarized. The analysis approach and findings are presented in section 3.3, with conclusions and implications for future work discussed in section 3.4. A detailed derivation of key results in 3.2 is presented in the Appendix.

3.2 Formalism

We consider the mean pairwise velocity of clusters derived from the kSZ effect as a probe for dark energy models and modifications to general relativity. Section 3.2.I summarizes the halo model approach to analytically calculate the mean pairwise velocity of clusters, and 3.2.II presents the formalism to estimate the covariance matrix of the mean pairwise velocity. In sections 3.2.III and 3.2.IV we discuss the fiducial cosmological model and survey assumptions.

I Motion of clusters as a probe of cosmology

Pairwise velocity statistics can be used to constrain the cosmological model of the Universe and the underlying theory of gravity [127, 128, 129]. We analytically model the expected large scale motion of clusters under cosmological gravitational interactions by considering the properties of dark matter particles, in linear theory, and then using a halo model to infer the

velocity statistics of gravitationally bound halos, which we use as proxies for galaxy clusters.

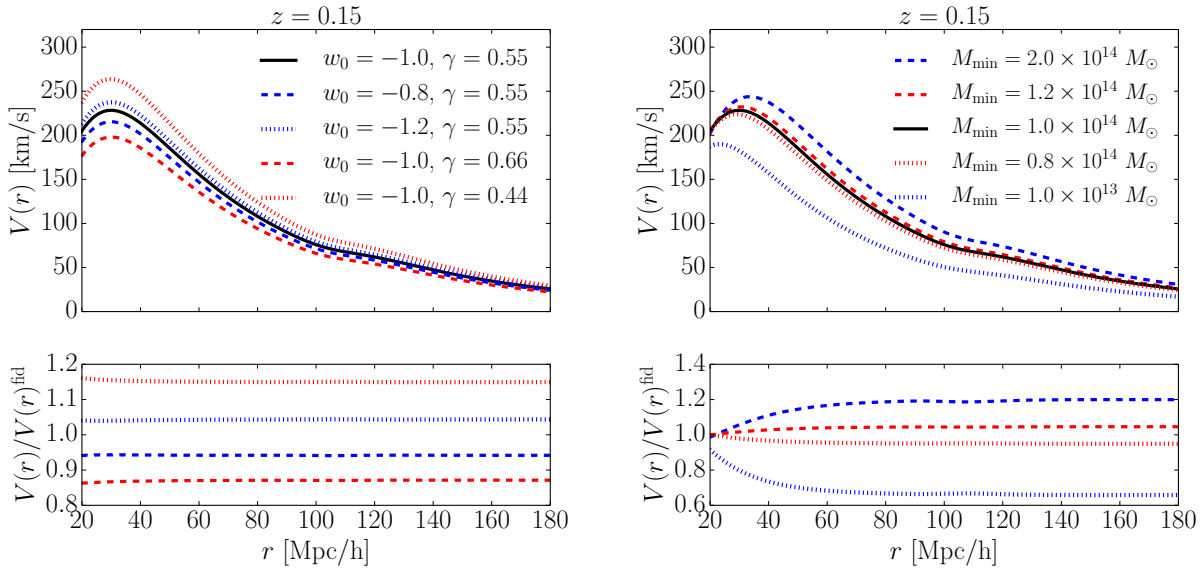

Figure 8: [Left panel] The mean pairwise cluster velocity, V, for different values of the dark energy equation of state parameter, w_0, and the modified gravity parameter, γ, at $z = 0.15$ with the black line corresponding to our fiducial model (see Section 3.2.III) and assuming a minimum cluster mass of $M_{\rm min} = 1 \times 10^{14}\ M_\odot$. A more negative w_0 leads to an increase in V. A decreased value of γ increases the growth rate and therefore increases V whereas a higher value of γ has the opposite effect. The same fractional change in γ has a greater effect on the amplitude of V than changing w_0. [Right panel] The mean pairwise cluster velocity, V, for different minimum mass cut-offs at redshift of $z = 0.15$. Note that changing $M_{\rm min}$ changes the shape as well as the amplitude of V. Higher $M_{\rm min}$ leads to an increase in mean pairwise velocity since the more massive clusters tend to have higher streaming velocities. [Lower panels] Ratio of the mean pairwise velocity, V, for the different scenarios to that for the fiducial model, $V^{\rm fid}$.

Following the formalism outlined in [130], we assume linear theory to describe the mean pairwise streaming velocity, v, between two dark matter particles, at positions $\mathbf{r_i}$ and $\mathbf{r_j}$, in terms of their comoving separation $r = |\mathbf{r_i} - \mathbf{r_j}|$,

$$v(r,a) \quad = \quad -\frac{2}{3} f_g(a) H(a) a r \frac{\bar{\xi}(r,a)}{1+\xi(r,a)} \tag{3.2.1}$$

where ξ is the dark matter 2-point correlation function and $\bar{\xi}$ the volume averaged correlation

function, respectively defined as,

$$\xi(r,a) = \frac{1}{2\pi^2}\int dk k^2 j_0(kr) P(k,a), \tag{3.2.2}$$

$$\bar{\xi}(r,a) = \frac{3}{r^3}\int_0^r dr' r'^2 \xi(r',a), \tag{3.2.3}$$

with $P(k,a)$ being the dark matter power spectrum and $j_0(x) = \sin(x)/x$ is the zeroth order spherical Bessel function.

The properties of dark matter halos of mass M, relative to the dark matter distribution, can be modeled using a halo bias

$$b(M,a) = 1 + \frac{\delta_{\rm crit}^2 - \sigma_0^2(M, a=1)}{\sigma_0^2(M,a=1)\delta_{\rm crit} D_a}, \tag{3.2.4}$$

where $M(R) = 4\pi R^3 \bar{\rho}/3$, $\bar{\rho}$ is the average cosmological matter density, the critical overdensity is taken to have the standard ΛCDM value of $\delta_{\rm crit} \approx 1.686$, and the zeroth order moment of the mass distribution squared is

$$\sigma_0^2(m,a) = \frac{1}{2\pi^2}\int_0^\infty dk k^2 P(k,a) W^2(kR(M)) \tag{3.2.5}$$

with a top-hat window function $W(x) = 3(\sin x - x\cos x)/x^3$.

Surveys will generally include cluster halos over a range of masses above some limiting mass threshold, $M_{\rm min}$. To analyze the mass statistics we consider a *mass averaged* cluster pairwise velocity statistic, V, for pairs of clusters separated by a comoving distance r

$$V(r,a) = -\frac{2}{3} H(a) a f_g(a) \frac{r\bar{\xi}_h(r,a)}{1+\xi_h(r,a)}, \tag{3.2.6}$$

which has an analogous expression to that in equation (3.2.1) [130, 131], with

$$\xi_h(r,a) = \frac{1}{2\pi^2}\int dk k^2 j_0(kr) P_{\rm lin}(k,a) b_h^{(2)}(k), \tag{3.2.7}$$

$$\bar{\xi}_h(r,a) = \frac{3}{r^3}\int_0^r dr' r'^2 \xi(r',a) b_h^{(1)}(k). \tag{3.2.8}$$

The mass-averaged halo bias moments, $b_h^{(q)}$, are given by

$$b_h^{(q)}(k,a) = \frac{\int_{M_{\rm min}}^{M_{\rm max}} dM\ M\ n(M,a) b^q(M,a) W^2[kR(M)]}{\int_{M_{\rm min}}^{M_{\rm max}} dM\ M\ n(M,a) W^2[kR(M)]} \tag{3.2.9}$$

where $n(M, a)$ is the number density of halos of mass M, given by the Jenkins mass function, and the Gaussian window function, $W(x) = \exp(-x^2/2)$, with $M(R) = (2\pi)^{3/2}\bar{\rho}R^3$.

In Figure 8 we show the mean pairwise velocity, V as a function of cluster separation r for a number of cosmological models at $z = 0.15$ for a survey with limiting mass $M_{\rm min} = 10^{14}\ M_\odot$, assuming all other survey specifications are fixed (left panel) and for various assumptions on the limiting mass (right panel). The figure suggests that, as with other linear growth rate related statistics, the equation of state, w_0, and growth exponent, γ, have degenerate effects on the pairwise velocity amplitude, through their effects on the growth factor, and do not alter the shape of the function. However, as indicated in section 3.3.IV, the redshift dependence of these parameters helps to break the degeneracy. To be more specific, the amplitude of V as a function of z is different for variations in γ compared to w_0. Increasing the minimum cluster mass shifts the peak of the pairwise velocity function to larger scales (on scales below 60 Mpc/h) and boosts the overall amplitude on scales larger than this, because the larger clusters have a larger streaming velocity.

Figure 9 shows the effect of different window function when calculating the mass-averaged halo moments $b_h^{(q)}(k, a)$. For large minimum mass, a top-hat filter induces sharp features in V due to edge effects of the window function at small scales, whereas a Gaussian filter leads to smoother results. Therefore, in the following we assume a Gaussian window function.

II Covariance matrix

Measurements of cluster velocities are subject to a number of statistical and systematic uncertainties. First, discreteness effects need to be taken into consideration; a smooth continuous field is typically assumed to underly a discrete distribution of local objects, which leads to shot noise. For a large sample size the shot noise should be approximately Gaussian resulting in an error proportional to $1/N$ [132], where N is the number of objects in the sample. If the number of objects (e.g. clusters) in the sample is not sufficiently large, the

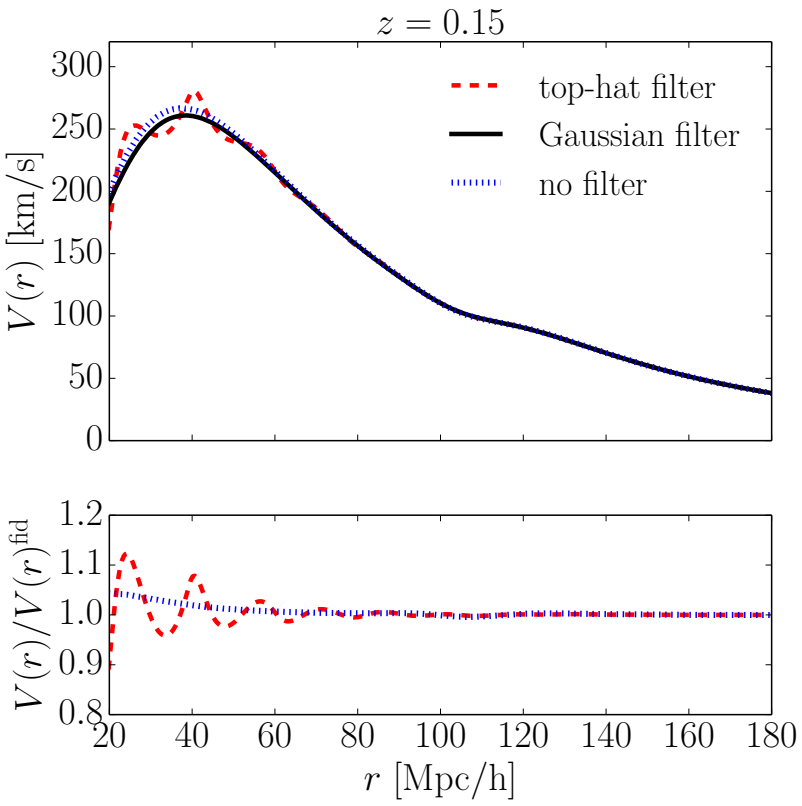

Figure 9: [Upper panel] The mean pairwise cluster velocity, V, for different window function in the $b_h^{(q)}(k,a)$ calculation at $z = 0.15$ and assuming a limiting mass of $M_{\rm min} = 4 \times 10^{14}\ M_\odot$ with the black line corresponding to a Gaussian filter. A top-hat (red dashed line) window function leads to sharp features due to edge effects at small scales, while no filtering (blue dotted line) shows a slight excess at small scales compared to a Gaussian filter. These edge effects increase for higher masses. [Lower panels] Ratio of the mean pairwise velocity, V, for the different scenarios to the Gaussian filter.

Gaussian limit breaks down, and an additional non-Gaussian contribution to the shot noise can become relevant [133].

Second, as in any cosmological survey, the measurement will be subject to cosmic variance due to the finite size of the sample. Third, in addition to the statistical errors we include a velocity measurement error [131] to account for the accuracy of the measurements and the uncertainty in the optical depth of the clusters. The total covariance for the mean pairwise velocity is therefore a combination of cosmic variance, shot noise, and the velocity

measurement error:

$$C_V^{\rm total}(r,r') = C_V^{\rm cosmic}(r,r') + C_V^{\rm shot}(r,r') + C_V^{\rm measurement}(r,r'). \quad (3.2.10)$$

A detailed derivation of the covariance terms can be found in the Appendix. We summarize the results here.

Defining an estimator for the mean pairwise velocity, $\hat{V}$, enables the covariance matrix to be calculated using

$$C_V(r,r') = \langle \hat{V}(r)\hat{V}(r')\rangle - \langle \hat{V}(r)\rangle\langle \hat{V}(r')\rangle \quad (3.2.11)$$

where $\langle \dots \rangle$ is the volume average. For analyzing a survey we include binning, as observations will be combined not at just one radius r but in bins of width Δr,

$$\hat{V}(r) \to V_\Delta(r) = \frac{1}{V_{\rm bin}} \int_{r-\Delta r/2}^{r+\Delta r/2} \tilde{r}^2 d\tilde{r} \int d\Omega \hat{V}(\tilde{r}), \quad (3.2.12)$$

assuming spherical symmetry and where a Δ subscript indicates binned quantities over bins of size Δr.

The covariance between the mean pairwise velocities of two cluster pairs, with the two pairs separated by r and r' and using bin width Δr, can be expressed as

$$\begin{aligned} C_V(r,r') = & \frac{4}{\pi^2 V_s(a)} \left(\frac{H(a)a}{1+\xi_h(r,a)}\right)^2 f_g(a)^2 \\ & \times \left[\int dk \left(P_{\rm lin}(k,a) b_h^{(1)}(k) + \frac{1}{n_{\rm cl}(a)} \right)^2 W_\Delta(kr) W_\Delta(kr') \right. \\ & + \left. \frac{\Delta r}{V_\Delta(r')} \int dk k \frac{P_{\rm lin}(k,a) b_h^{(1)}(k)}{n_{\rm cl}(a)^2} W_\Delta(kr) \right], \end{aligned} \quad (3.2.13)$$

where $V_s(a)$ is the survey volume, $n_{\rm cl}(a)$ is the number density of clusters, and

$$W_\Delta(kr) = 3\frac{R_{\rm min}^3 \tilde{W}(kR_{\rm min}) - R_{\rm max}^3 \tilde{W}(kR_{\rm max})}{R_{\rm max}^3 - R_{\rm min}^3} \quad (3.2.14)$$

$$\tilde{W}(x) = \frac{2\cos(x) + x\sin(x)}{x^3}. \quad (3.2.15)$$

The first term in equation (3.2.13) is the Gaussian contribution to the covariance, which includes both cosmic variance ($\propto P$) and shot noise ($\propto 1/n_{\rm cl}$). The second term is an additional contribution that is often neglected, which arises if the Gaussian limit breaks down; we refer to this term as 'Poisson' shot noise as in [133]. While we find it is subdominant in comparison to the Gaussian terms for a mass cut-off $M \leq 1 \times 10^{14}\ M_\odot$ (see Figure 11), it can be important for surveys with smaller cluster number densities. The purely Gaussian shot noise contribution on the other hand is not insignificant and should be included.

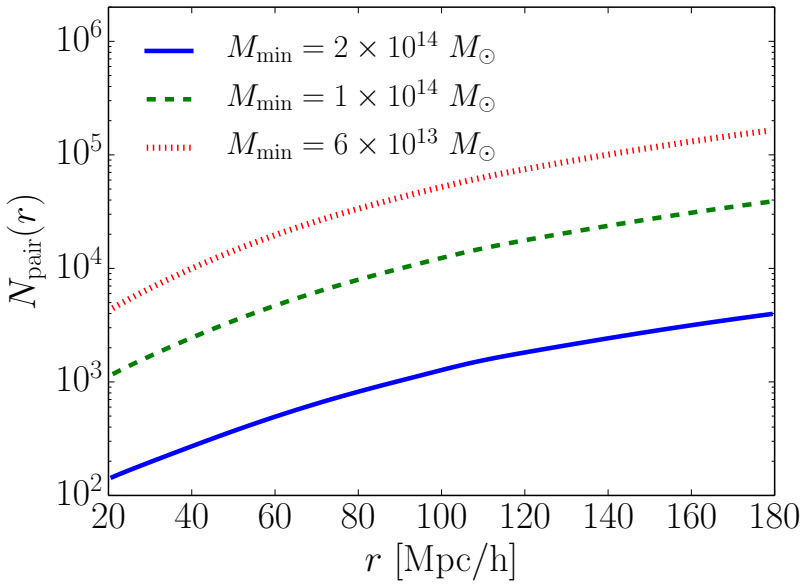

Figure 10: Number of cluster pairs, $N_{\rm pair}(r)$, versus separation in bins of $\Delta r = 2$ Mpc/h for different mass cut-offs at redshift $0.1 < z < 0.2$. This assumes a Jenkins mass function and a 6000 square degree survey.

We include a contribution to the covariance due to the uncertainty in measuring the velocity given by [131],

$$C_V^{\rm measurement}(r, r') \;=\; \frac{2\sigma_v^2}{N_{\rm pair}}\delta_{r,r'} \tag{3.2.16}$$

where σ_v is the measurement error discussed in more detail in section 3.3.IV, and $N_{\rm pair}$ is the

number of pairs in each separation bin given by

$$N_{\rm pair}(r,a) = \frac{n_{\rm cl}(a)V_s(a)}{2} \times \left(V_\Delta(r)n_{\rm cl}(a) + 4\pi r^2 n_{\rm cl}(a)\xi_h(r,a)\Delta r\right). \quad (3.2.17)$$

As shown in Figure 10, the number of cluster pairs increases rapidly with decreased minimum mass. The measurement error term in the covariance is proportional to $1/N_{\rm pairs}$ and will increase quickly with an increasing number of bins since the number of cluster pairs directly depends on the size of the r-bin.

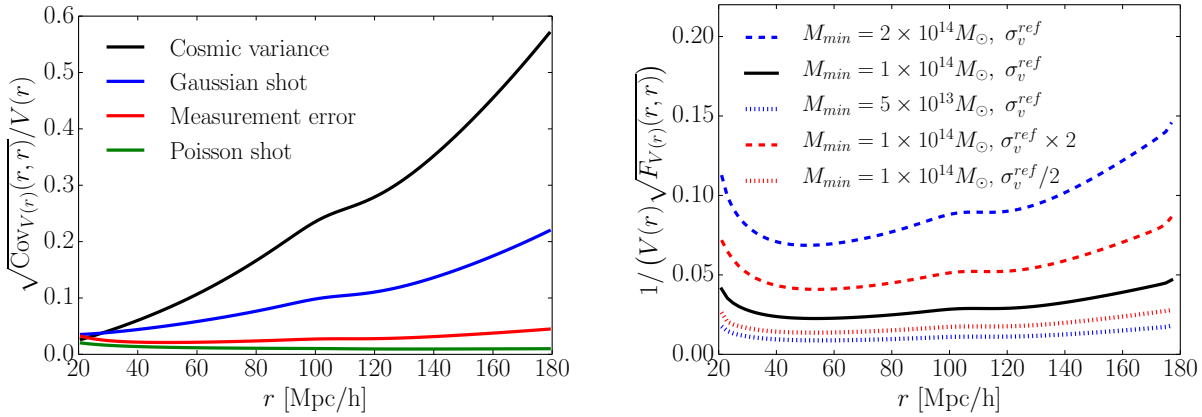

Figure 11: [Left panel] The relative error on the mean pairwise velocity of clusters at redshift $0.1 < z < 0.2$ for a separation bin size $\Delta r = 2$ Mpc/h assuming a Stage III like survey (see Table 5). The Poisson shot noise is sub-dominant compared to the other terms, the Gaussian shot noise term however cannot be neglected. [Right panel] One over the diagonal terms of the total Fisher matrix relative to the mean pairwise velocity for varying the minimum mass and the measurement error. The effect of the minimum mass on the fisher matrix is more prevailing than the dependency on the measurement error.

Figure 11 shows the diagonal elements of the covariance matrix for the different covariance components, for a bin width of $\Delta r = 2$ Mpc/h. As cluster separation increases, the covariance becomes dominated by cosmic variance, while at smaller separations $\lesssim 40$ Mpc/h, the contributions from each of the terms becomes comparable. As a result of the multiple contributions to the covariance matrix, and their respective sensitivities to bin size and cluster separation, the total covariance matrix slightly depends upon the number of bins.

The measurement error and shot noise can be reduced by choosing a coarser binning with the trade-off of decreased resolution and loss of information. On the other hand, the fractional contribution of the cosmic variance will increase as the size of the bins increases. Once the cosmic variance dominates nothing can be gained from a coarser binning. A very coarse binning marginally reduces the constraints, e.g. using $\Delta r = 20$ Mpc/h lowers the FoM by 30% compared to $\Delta r = 2$ Mpc/h, however, any bin size smaller than $\Delta r = 5$ Mpc/h leads to equivalent results. Throughout the analysis we assume a bin size of $\Delta r = 2$ Mpc/h.

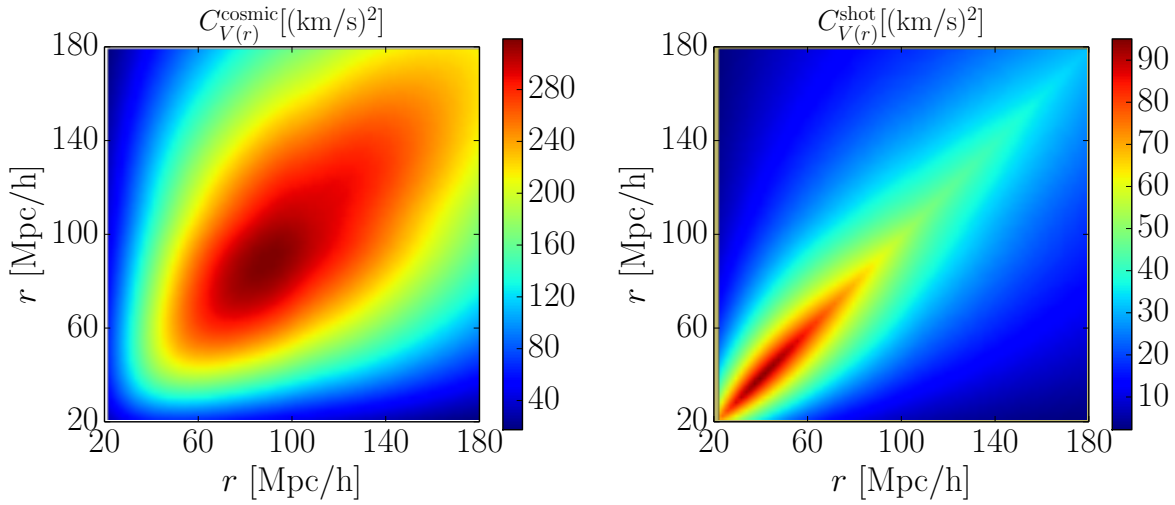

Figure 12: 2D contour plots of the cosmic variance [left panel] and the shot noise term [right panel] at redshift $0.1 < z < 0.2$ assuming a separation bin size of $\Delta r = 2$ Mpc/h, a lower mass limit of $M_{\rm min} = 1 \times 10^{14}\ M_\odot$, and a sky coverage of 6000 square degrees. Note that both terms have notable nonzero off-diagonal terms that affect the total inverse covariance used in the Fisher analysis, and that while the cosmic variance values are larger, the Gaussian noise term should not be neglected as it can have a significant effect, particularly for small separations.

Off-diagonal covariances between cluster pairs of different separations are important. Figure 12 shows the covariance contributions from cosmic variance and shot noise and indicates the comparative importance of off-diagonal terms. The off-diagonal contributions have a notable effect on the Fisher matrix amplitudes as a function of separation, giving rise to the differences between the left and right panels in Figure 11. The right panel shows the effect on the Fisher matrix of changing key model assumptions, the minimum detectable cluster mass and the mean pairwise velocity uncertainty. Altering the mass limit has a larger

effect than comparable changes to the the measurement error because the number of clusters and cluster pairs strongly depend on the limiting mass (see Figure 10), changing shot noise as well as the measurement error contribution to the covariance significantly.

III Cosmological Model

For our analysis we consider constraints on nine cosmological parameters:

$$\mathbf{p} \;=\; \{\Omega_b h^2, \Omega_m h^2, \Omega_k, \Omega_\Lambda, w_0, w_a, n_s, \ln A_s, \gamma\} \tag{3.2.18}$$

where Ω_b, Ω_m, Ω_k and Ω_Λ are the dimensionless baryon, matter, curvature and dark energy densities respectively, h is the Hubble constant in units of 100 km/s/Mpc, w_0 and w_a are the dark energy equation of state parameters, such that the equation of state is $w(a) = w_0 + (1-a)w_a$, γ is the growth rate exponent, such that $f_g = \Omega_m(a)^\gamma$, and n_s and A_s are the spectral index and normalization of the primordial spectrum of curvature perturbations.

Throughout this chapter we assume a fiducial model that is a ΛCDM cosmological model with parameters consistent with those adopted in [50]: $\Omega_b h^2 = 0.021805,\ \Omega_m h^2 = 0.1225,\ \Omega_k = 0,\ \Omega_\Lambda = 0.75,\ w_0 = -0.95,\ w_a = 0,\ n_s = 1,\ \ln(10^{10} A_s) = 3.1954.$

We calculate constraints on cosmological parameters using the Fisher Matrix formalism. The covariance between two parameters p_μ and p_ν, from (3.2.18), is given by

$$F_{\mu\nu} = \sum_i^{N_z} \sum_{p,q}^{N_r} \frac{\partial V(r_p, z_i)}{\partial p_\mu} \mathrm{Cov}_i^{-1}(r_p, r_q, z_i) \frac{\partial V(r_p, z_i)}{\partial p_\nu}, \tag{3.2.19}$$

where $\mathrm{Cov}(r_p, r_q, z_i)$ is the covariance matrix between two clusters pairs as defined in 3.2.II, including a redshift bin with mid-point z_i and the clusters in each pair having comoving separations of r_p and r_q. N_z and N_r are the number of redshift and spatial separation bins, respectively.

We quote results in terms of the Dark Energy Figures of Merit (FoM) as described in

Table 4: CMB survey specifications, for the sky coverage, $f_{\rm sky}$, beam size, $\theta_{\rm FWHM}$, and noise levels per pixel for the temperature and polarization detections at 3 frequencies, for a Planck-like survey.

	Frequency (GHz)		
	100	143	217
$f_{\rm sky}$		0.8	
$\theta_{\rm FWHM}$(arcmin)	10.7	8.0	5.5
$\sigma_T(\mu{\rm K})$	5.4	6.0	13.1
$\sigma_E(\mu{\rm K})$	-	11.4	26.7

section (1.4.II). When we are fixing γ to it's fiducial value we refer to the FoM$_{\rm GR}$ given by

$$\text{FoM}_{\rm GR} \;=\; \det\left[(F^{-1}_{\rm GR})\right]^{-1/2}_{w_0,w_a}. \tag{3.2.20}$$

with $(F^{-1}_{\rm GR})_{w_0,w_a}$ being the 2×2 submatrix of the inverted Fisher matrix excluding the modified gravity parameter γ. This procedure is equivalent to marginalizing over the seven parameters (for MG) or six parameters (for GR) of the model considered.

Throughout this chapter we consider results in combination with either simply a Planck-like CMB prior or a Dark Energy Task Force (DETF) [25] prior that includes CMB, SN, and non-kSZ related LSS constraints on the background cosmological and dark energy parameters. We do not include a prior on the modified gravity parameters unless stated otherwise. For the Planck-like CMB survey, we consider complementary constraints on the cosmological parameters from the temperature (T) and polarization (E) measurements up to $l = 3000$ as summarized in Table 4 [1].

IV Survey Specifications

We forecast cosmological constraints for three different combinations of surveys: 1) a current (Stage II) CMB survey, such as ACTPol [123], combined with a galaxy sample that includes

[1] www.rssd.esa.int/SA/P LANCK/docs/Bluebook-ESA-SCI(2005)1V2.pdf

spectroscopic redshifts, such as SDSS BOSS [52]), 2) a near-term (Stage III) survey, such as Advanced ACTPol [125], also combined with SDSS BOSS, and 3) a longer-term (Stage IV) survey, such as CMB-S4 [40], combined with a next generation spectroscopic survey, such as DESI [53].

The mean cluster pairwise velocity can be measured by cross-correlating the kSZ signal with cluster positions and redshifts. For the cluster sample, we assume that a spectroscopic survey provides redshifts to luminous red galaxies (LRGs) over an overlapping area with the CMB survey. Recent studies show that the kSZ signal can be extracted from the CMB maps using LRGs of the BOSS survey as a proxy for clusters [134]. Using LRGs creates a large, precise positioned sample of tracers to extract the kSZ correlation.

Table 5: Reference survey specifications used to model Stage II, III and IV kSZ cluster surveys. The expected instrument sensitivity of the CMB survey, $\Delta T_{\rm inst}$, along with the assumed optical LSS survey redshift range $z_{\rm min} < z < z_{\rm max}$, redshift binning, and minimum detectable cluster mass, $M_{\rm min}$ are shown. We consider an effective sky coverage by estimating the degree of overlap between the respective CMB and optically selected cluster data sets.

		Survey Stage		
Survey	Parameters	II	III	IV
CMB	$\Delta T_{\rm instr}$ (μKarcmin)	20	7	1
Galaxy	$z_{\rm min}$	0.1	0.1	0.1
	$z_{\rm max}$	0.4	0.4	0.6
	No. of z bins, N_z	3	3	5
	$M_{\rm min}$ ($10^{14} M_\odot$)	1	1	0.6
Overlap	Area (1000 sq. deg.)	4	6	10

However, there are several factors that need to be considered in using LRGs as cluster tracers. LRGs are not perfect tracers of a cluster's center, with perhaps 40% of bright LRGs and 70% of faint LRGs off-centered, satellite galaxies [135] that may be related to cluster mergers [136]. The imprecise match between LRGs and clusters could lead to detrimental misalignments, such as trying to extract the kSZ signal from positions that are not associated

with clusters or an incomplete cluster catalog if spectroscopic measurements of an LRG near the cluster center were not obtained. The theoretical mean cluster pairwise velocity is an observable averaged over all cluster pairs assuming a complete sample above a limiting minimum mass. While [134] optimize the angular size of the CMB sub-map used in the stacking approach to minimize the overall covariance, this does not ensure that the cluster sample obtained from the LRGs is complete. Further studies are needed to quantify the effects of using LRGs as cluster tracers and ensure that no bias is introduced in the analysis before this approach can be used for cosmological constraints. Additional clustering information, such as the halo occupation distribution of the galaxy sample, must be used to quantify the uncertainty of LRGs as accurate cluster tracers and ensure that no bias is introduced in the cosmological constraints. Modeling the number and distribution of galaxies within the dark matter halos could include both full simulations and constraints from LSS data. [137]

Another issue is that the uncertainty in the minimum mass of the cluster sample associated with the LRGs is difficult to estimate, although, the minimum mass uncertainty could be treated as an additional nuisance parameter in the analysis.

To acknowledge these issues in our forecasts, we assume a scenario that aims to maximize cluster completeness and purity, with a well defined cluster mass cut-off, rather than cluster number density. We select a survey area that has photometric and spectroscopic galaxy catalogs and overlapping CMB kSZ data. Specifically, we consider BOSS and a DESI-like survey, for which we expect photometric catalogs to exist over the survey area. We note that Euclid spectroscopic and imaging surveys, and LSST imaging with overlapping WFIRST imaging and spectroscopy would also provide future valuable data sets at higher redshifts. The uncertainties in the cosmological parameters evolve as the square root of the sky coverage. Requiring spectroscopic redshifts, e.g. from BOSS, limits the survey area, but provides confidence that the comoving cluster separation can be accurately calculated as in [122]. Photometric information allows cluster detection, and mass estimates, using algorithms, such as the friends-of-friends, as used in redMaPPer [138], to maximize the completeness

and purity of the cluster sample, with the drawback of a limited number of clusters and a volume-limited catalog. A study of using only photometric information to extract the kSZ signal can be found in [139].

The survey specification assumed in our analysis for the CMB and LSS Stage II, III and IV surveys are given in Table 5. We assume a BOSS-like spectroscopic survey for Stage II and III and a DESI-like Stage IV survey with redshift ranges that are determined by the redshift coverage of the LRG sample and assume joint photometric survey data. We assume Stage II and Stage III have access to the same or comparable LRG surveys so retain the same limiting mass, but do slightly increase CMB overlap with these data due to the larger survey area planned for Advanced ACTPol [125]. For Stage IV we assume a deeper LRG survey that provides lower minimum mass, higher z, and larger overlap. Our minimum mass assumptions are conservative, and will likely be improved upon at each respective stage. As an example, the LSST survey projects that the minimum detectable cluster mass at $z \sim 0.6$ will be lower than $\sim 5 \times 10^{13}\ M_\odot$ after a single visit image in all bands, and be better than $10^{13}\ M_\odot$ in all bands in the complete ten-year survey [49]. Similarly the SDSS-derived MaxBCG Catalog already achieves 90% purity and >85% completeness for clusters of masses exceeding $10^{14}\ M_\odot$ [140].

The measurement error for the radial peculiar velocity, v, of a cluster is a combination of the instrumental sensitivity as well as the uncertainty in the optical depth, τ, for each cluster as the kSZ signal is proportional to τ as follows [47],

$$\frac{\Delta T_{\rm kSZ}}{T_{\rm CMB}} = -\frac{v}{c}\tau, \tag{3.2.21}$$

where $T_{\rm CMB}$ is the temperature of the CMB. We estimate the total measurement error by adding those two sources of uncertainty in quadrature as

$$\sigma_v = \sqrt{\sigma^2_{\rm instr} + \sigma^2_\tau}. \tag{3.2.22}$$

Table 6: The assumed individual contribution from instrument sensitivity, $\sigma_{\rm instr}$, and uncertainty in τ, σ_τ. The values of τ and fractional uncertainty in τ, $(\Delta\tau/\bar{\tau})^2$, are estimated from simulations assuming a convolution over a $1.3'$ beam. σ_v is the total measurement uncertainty for the reference case.

		Redshift bin				
		0.15	0.25	0.35	0.45	0.55
$10^3\tau$		3.45	2.27	1.84	1.45	1.20
$(\Delta_\tau/\bar{\tau})^2$				0.15		
σ_τ (km/s)				120		
$\sigma_{\rm instr}$	Stage II	290	440	540	-	-
(km/s)	Stage III	100	150	190	-	-
	Stage IV	15	22	27	34	42
σ_v	Stage II	310	460	560	-	-
(km/s)	Stage III	160	200	230	-	-
	Stage IV	120	120	120	120	130

The accuracy of the instrument is given by

$$\sigma_{\rm instr} = \frac{\Delta T_{\rm instr}}{\Delta T_{\rm kSZ}} \times v = \frac{\Delta T_{\rm pixel}/\sqrt{N_{\rm pixel}}}{\tau v/cT_{\rm CMB}} \times v \tag{3.2.23}$$

where $\Delta T_{\rm pixel}$ is the sensitivity of the instrument per pixel and $N_{\rm pixel}$ being the number of pixels of a cluster. We assume that an average size cluster will have $N_{\rm pixel} \approx 4$ and an instrument sensitivity as summarized in Table 5. The uncertainty in the optical depth is given by

$$\sigma_\tau = \frac{\Delta\tau}{\tau} \times v. \tag{3.2.24}$$

Assumed uncertainties contributing to the measurement error are summarized in Table 6. We use the scatter in the optical depth, $|\Delta\tau/\bar{\tau}|$, and the mean value of τ from simulations [141] [2], to obtain an indicative estimate for the intrinsic dispersion in τ averaged over all cluster masses. For the fiducial analysis we do not include any further dispersion arising

[2]N. Battaglia: private communication

from potential additional measurement accuracy in determining τ. Section 3.3.IV includes a discussion of the impact of additional factors affecting the measurement error on the cosmological constraints.

3.3 Analysis

Section 3.3.I summarizes and compares the results of each survey. The effect of modeling assumptions on the minimum detectable cluster mass, the minimum cluster separation considered, the measurement error, and the dark energy model are discussed in sections 3.3.II-3.3.V.

I Potential kSZ constraints on dark energy and modified gravity

In this section we discuss the potential of upcoming kSZ surveys to constrain dark energy and modified gravity parameters. Figure 8 shows both the equation of state, driving the expansion history, and γ, that modifies the growth history of density perturbations, have qualitatively similar effects on the pairwise velocity function through their effect on the linear growth factor. For cluster measurements in each individual redshift bin this creates a degeneracy between the equation of state and γ parameters. As shown in Figure 13, the use of multiple redshift bins allows the differences in the evolution of the growth rate for the dark energy and modified gravity parameters to be distinguished. The constraints on w_0 and γ from the low and high redshift bins are markedly orthogonal; in combination this complementarity tightens the constraints, in particular on the growth factor. In Figure 14 we present the 2D marginalized constraints in the $w_0 - \gamma$ parameter plane for kSZ in combination with a Planck-like CMB and DETF priors on all parameters excluding γ, including CMB, BAO, weak lensing and supernovae measurements for a combination of Stage III like surveys [25]. The suite of Stage III DETF-motivated observables would provide stronger constraints

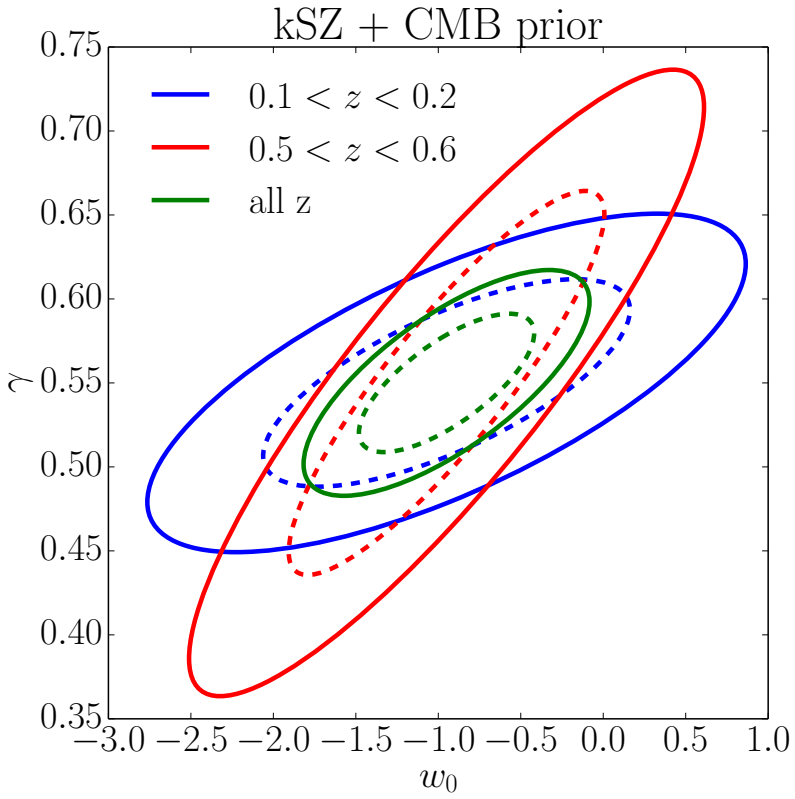

Figure 13: 2D projected likelihoods for the $w_0 - \gamma$ parameter space, showing the 68% and 95% confidence levels for Stage IV-like survey are shown for two well-separated spectroscopic redshift bins, $0.1 < z < 0.2$ (blue) and $0.5 < z < 0.6$ (red), and when all five redshift bins, $0.1 < z < 0.6$ (green) are considered when combined with Planck-like CMB priors. The inclusion of multiple redshift bins breaks degeneracies between w and γ and improves the kSZ driven constraints on the growth history.

on the equation of state, through the addition of geometric measurements that constrain the expansion history. These break the degeneracy between w_0 and γ from kSZ and CMB measurements alone. With the addition of a CMB prior on the data, however, the data can constrain γ to 9%, 8% and 5% respective in the Stage II through IV survey specifications. The kSZ is a less powerful tool for constraining the dark energy equation of state. A Stage IV-like survey can achieve figure of merits of $\mathrm{FoM}_{\mathrm{GR}} = 61$ with a CMB prior (which has $\mathrm{FoM}_{\mathrm{GR}} = 1.15$ alone), and $\mathrm{FoM} = 292$ with DETF Stage III data included ($\mathrm{FoM}_{\mathrm{GR}} = 116$).

Complementary, contemporaneous constraints from baryonic acoustic oscillations and

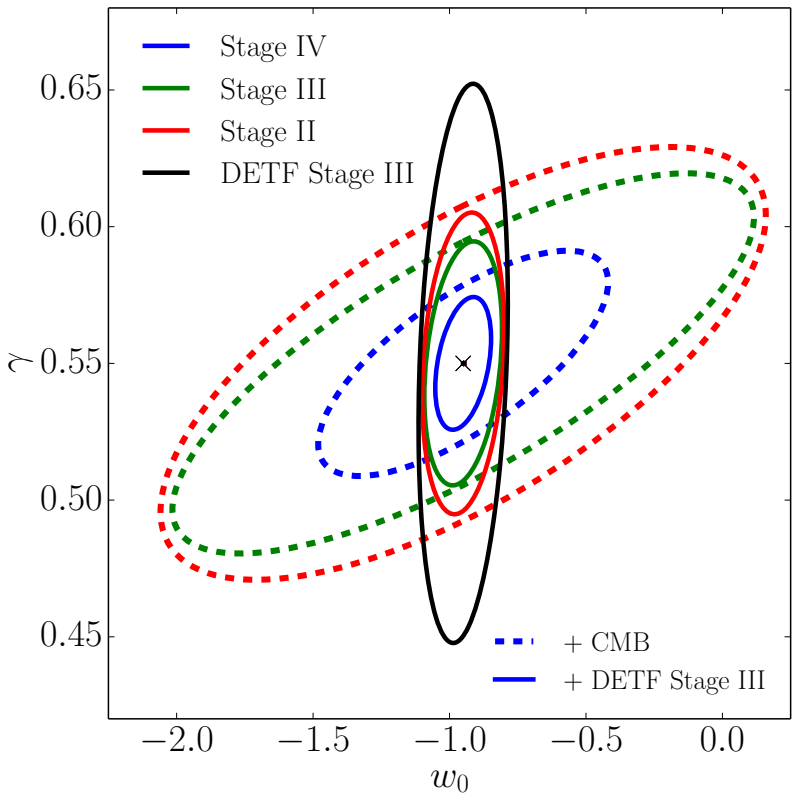

Figure 14: 2D projected likelihoods for $w_0 - \gamma$ parameter space, showing the 68% confidence levels for Stage II (red), III (green) and IV (blue)-like surveys when combined with Planck-like CMB priors only (dashed) and DETF stage III GR priors (solid, excluding DETF constraints on γ) [25]. For comparison, the projected DETF Stage III constraints alone (including γ), that includes CMB, SN and non-kSZ related LSS constraints, are shown (black solid line).

Type Ia supernovae will provide significantly tighter constraints on the background expansion history and the equation of state. If we include the impact of a DETF Stage III prior on all parameters, excluding the growth factor, the degeneracy between the equation of state and growth factor is significantly reduced and the projected constraints on γ are improved, with fractional errors of 5% and 3% for Stage III and Stage IV surveys. Table 7 summarizes the FoM, assuming modified gravity (MG) (nine parameters, marginalizing over γ), general relativity (GR) (eight parameters, fixing γ) and a flat, general relativity cosmology (seven parameters, fixing γ and Ω_k), as well as the 1σ constraints of w_0, w_a (marginalizing over γ)and γ for a Stage II, Stage III and Stage IV like survey, as specified in Table 5.

		Fiducial assumptions			+ Uncertainty in $M_{\rm min}$			+ Lower $M_{\rm min}$		
		Stg. II	Stg. III	Stg. IV	Stg. II	Stg. III	Stg. IV	Stg. II	Stg. III	Stg. IV
+CMB	FoM$_{MG}$	5	6	26	4	9	19	7	9	154
	FoM$_{\rm GR}$	7	10	47	6	12	29	10	15	195
	FoM$_{\rm flat}$	33	43	102	28	40	84	50	63	289
	$\sigma(w_0)$	0.73	0.70	0.35	0.62	0.39	0.41	0.67	0.63	0.09
	$\sigma(w_a)$	2.6	2.5	1.2	2.2	1.4	1.5	2.5	2.3	0.3
	$\Delta\gamma/\gamma$	0.09	0.08	0.05	0.10	0.07	0.05	0.07	0.06	0.02
+DETF	FoM$_{MG}$	119	130	208						
	FoM$_{\rm GR}$	128	139	229						
	FoM$_{\rm flat}$	176	191	321						
	$\sigma(w_0)$	0.10	0.09	0.07						
	$\sigma(w_a)$	0.30	0.29	0.24						
	$\Delta\gamma/\gamma$	0.07	0.05	0.03						

Table 7: [Left columns] Results for the reference survey assumptions as summarized in Table 5 including [top rows] Planck priors and [lower rows] constraints on the background cosmological parameters (excluding γ) from the DETF Stage III survey. For reference, the Planck-like Fisher matrix alone has FoM$_{\rm GR} = 1.15$ and DETF has FoM$_{\rm GR} = 116$. [Central columns] Results in which the impact of an uncertainty in the exact minimum mass of the cluster sample, $M_{\rm min}$, is included by marginalizing over $M_{\rm min}$ as a nuisance parameter with a 15% prior imposed. [Right columns] Results for a more optimistic mass cut-off of $M_{\rm min} = 4 \times 10^{13}\ M_\odot$ for Stage II and III and $M_{\rm min} = 1 \times 10^{13}\ M_\odot$ for Stage IV with marginalization over $M_{\rm min}$ with a 15% prior imposed as well. Constraints as a function of $M_{\rm min}$ are also shown at the top of Figure 15.

These results could provide valuable complementary constraints to those on γ from spectroscopic galaxy clustering surveys. Projections include constraints of $\Delta\gamma/\gamma \simeq 5\%$ from measurements at $z > 0.65$ using OII for a DESI-like survey [142], and comparable from a Euclid-like $H\alpha$ survey, for which [143] projected $\Delta\gamma/\gamma = 4\%$ (assuming a luminosity function [144] that has since been revised downwards to lower $H\alpha$ number counts [145, 146]).

II Dependence on minimum mass of the galaxy cluster sample

For cluster abundance measurements knowing the precision with which the minimum mass is known is important. To assess the degree of precision required for the pairwise measurements we consider the impact on the cosmological constraints of marginalizing over the minimum mass, with a 15% prior on $M_{\rm min}$. The middle panel of Table 7 shows the effects of this marginalization: the constraints are loosened only slightly compared to the fiducial case, that has no marginalization over the minimum mass. This implies that a precise knowledge of the minimum mass is not crucial to achieve cosmological constraints. An explanation for the comparative insensitivity of the dark energy constraints to uncertainties in M_{min}, can be understood with reference to Figure 8. While varying dark energy parameters and M_{min} both change the large scale pairwise velocity amplitude the minimum mass also changes the shape of the pairwise velocity function. This means that uncertainties in the minimum mass can be discerned from those in dark energy, and do not translate into a comparable degradation of constraints on w or γ.

The measurement uncertainty on the mean pairwise velocity decreases with the number of clusters used for the cross-correlation. The upper panels of Figure 15 presents the dependence of the FoM and $\Delta\gamma/\gamma$ constraints on the assumed minimum observed mass. The increased number density of clusters and cluster pairs arising from a lower mass bound, below $\sim 10^{14}\ M_\odot$, significantly improves the statistical uncertainties in the pairwise velocity. For our analysis we integrated over a Jenkins mass function using the minimum observed mass as our lower

limit. As the number density of clusters drops off quickly for higher masses the constraints deteriorate strongly for a minimum mass above $M > 2 \times 10^{14}\ M_\odot$.

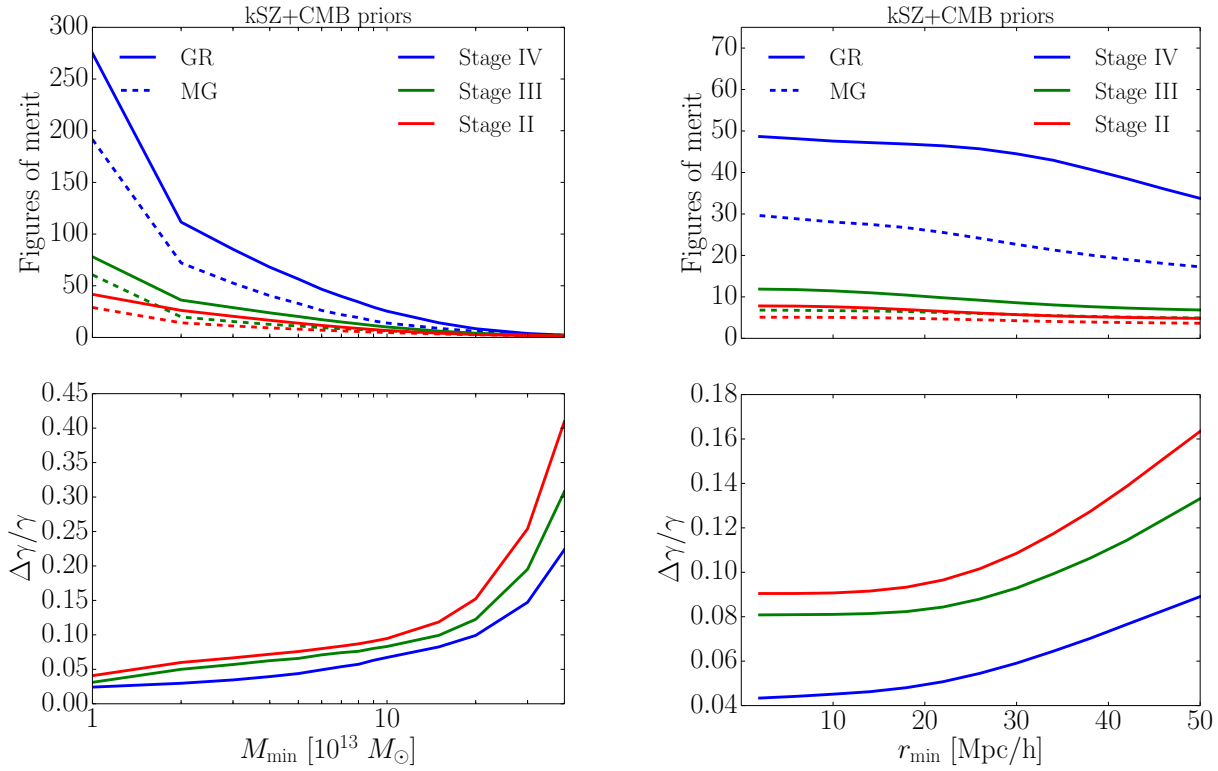

Figure 15: [Left] The impact of the assumed minimum mass of the cluster sample, $M_{\rm min}$, on the dark energy FoM and uncertainty on the growth factor, $\Delta\gamma/\gamma$, for the Stage II (red), Stage III (green) and Stage IV (blue) reference survey specifications (as given in Table 5) with a Planck-like CMB prior on all parameters except γ. FoM plots show results assuming standard general relativity ('GR', solid lines) and when the growth factor is marginalized over ('MG', dashed lines). [Right] The impact of including observations on small scales, denoted by the minimum separation $r_{\rm min}$. While including smaller-scale observations below ∼20 Mpc/h would appear to improve both the FoM and $\Delta\gamma/\gamma$, as discussed in the text, we note that caution must be used in including these scales, with the potential for additional theoretical uncertainties, not included here, as nonlinear effects become important.

Assuming that the complications discussed in section 3.2.IV, in determining LRG centrality and cluster mass estimates, can be controlled, in principle one could achieve much higher number densities and a smaller minimum mass. This would increase the number of pairs in the cluster sample. The window functions for lower mass halos would include additional

information in the mass averaged statistics from the power spectrum at smaller scales that would lead to tighter constraints on the cosmological parameters. The right columns of Table 7 show the results assuming a more optimistic mass cut-off than the reference case, $M_{\rm min} = 4 \times 10^{13}\ M_\odot$ for Stage II and III and $M_{\rm min} = 1 \times 10^{13}\ M_\odot$ for Stage IV. To account for the uncertainty in mass we marginalize over the minimum mass assuming a 15% prior. The GR FoM, with a CMB prior, are improved from $\mathrm{FoM_{GR}} = 6$ and $\mathrm{FoM_{GR}} = 10$ for Stage II and III to $\mathrm{FoM_{GR}} = 12$ and $\mathrm{FoM_{GR}} = 15$, compared to the reference scenarios, and by a factor of 1.8 for Stage IV. The uncertainty in γ reduces to $\Delta\gamma/\gamma = 0.07$, 0.06, and 0.02 for Stage II, III and IV.

III Dependence on the nonlinearity cut-off

As shown in Figure 11, the inverse covariance rises at lower cluster separations so that the inclusion of cluster pairs at small separation can have a potentially significant effect on improving the dark energy constraints. Simulation show a deviation from the predicted theoretical mean pairwise velocity, however, starting at separations of $r < 45$ Mpc/h [131] so that the nonlinear corrections to the cluster motion needs to be considered. Equation (3.2.1) has two major deficiencies: It relies on linear theory to model the underlying dark matter distribution [128, 130] and it assumes a linear, scale-independent bias [130]. The former leads to a discrepancy of the dark matter pairwise velocity with linear theory at nonlinear scales around $r \leq 10$ Mpc/h, the latter introduces deviations at even larger scales. It is worthwhile, therefore, to assess how accurately the mean pairwise velocity of clusters can be modeled in the transition to the nonlinear regime and how the cosmological constraints depend upon the assumed limiting minimum mass.

In Figure 15 we highlight the sensitivity of the FoM and uncertainty in the modified gravity parameter γ to the assumptions about the smallest cluster separations to be included in the analysis, parametrized here by $r_{\rm min}$. For a Stage IV like survey including all scales up

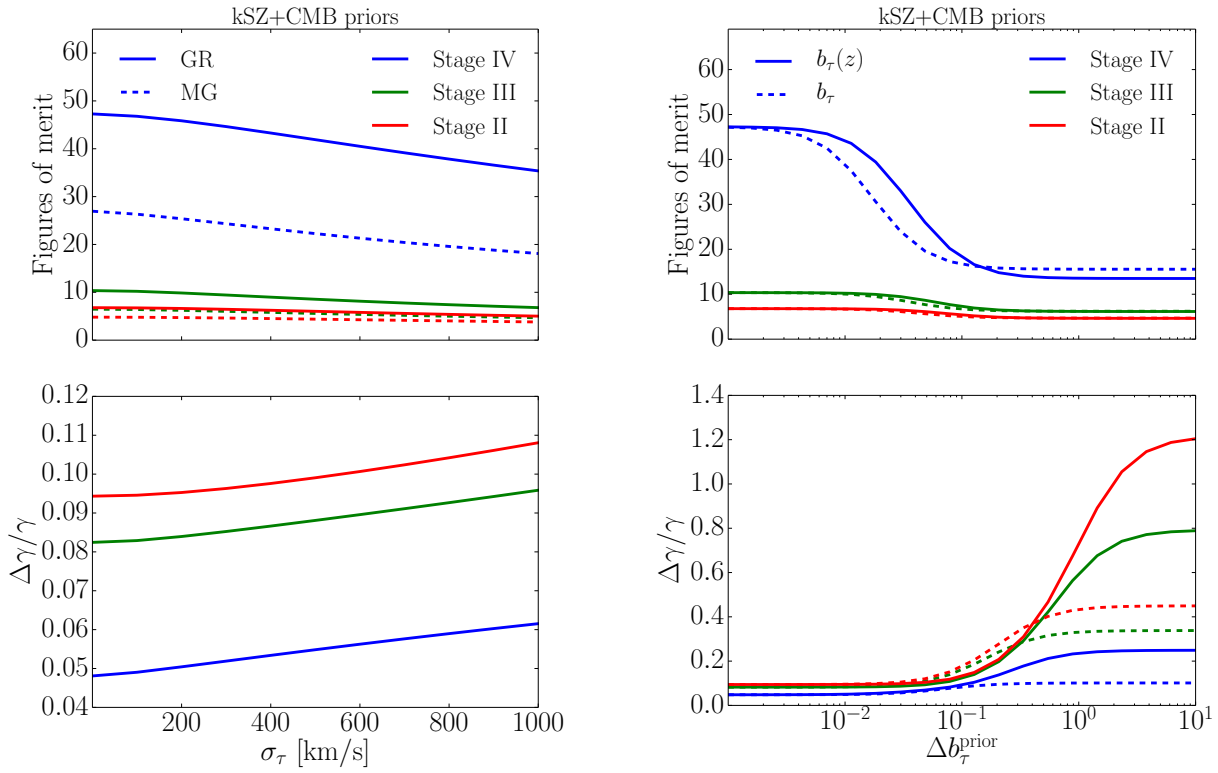

Figure 16: The impact of modeling assumptions in the determination of τ for each cluster on the dark energy FoM [upper panels] and fractional constraints on the growth factor [lower panels] for Stage II (red), Stage III (green) and Stage IV (blue) surveys. The left panels show the effect of increasing a statistical dispersion in the τ measurement, σ_τ, in the pairwise velocity covariance. The upper left shows the FoM assuming the growth rate is determined by GR (solid lines) and marginalizing over a freely varying γ ('MG', dashed lines), which corresponds to the $\Delta\gamma/\gamma$ constraints in the lower left panel. The right panels show the effect of a prior on a systematic offset in the τ value, parametrized by a multiplicative bias in each redshift bin (solid lines), $b_\tau(z)$, and a redshift independent multiplicative bias (dashed lines), b_τ. A detailed discussion of the relative sensitivities is provided in the text.

to $r = 5$ Mpc/h increases the FoM by 50% compared to an analysis with separations above 50 Mpc/h excluded and halves the uncertainty on γ.

In this work we chose a moderate approach cutting off our analysis in the mildly nonlinear regime using a minimum separation of $r_{\rm min} = 20$ Mpc/h. On-going work on using an perturbative approach to model nonlinearities [147] and improved N-body simulations suggests

that the formalism will be improved in the near future to fully exploit the mildly nonlinear regime.

IV Dependence on the measurement error

Central to utilizing the kSZ for cosmology, is the ability to measure the pairwise momentum accurately, and then in turn extract the pairwise velocity, from the momentum, through being able to determine the cluster optical depths. In this section we investigate in more detail the sensitivity of the constraints to these important effects.

As described in section 3.2.IV, the measurement error of a given cluster is given by the combination in quadrature of the instrument noise and the uncertainty in the optical depth of the cluster. In the fiducial analysis we include an uncertainty in the measurement of τ based on the intrinsic dispersion in the optical depth observed in cluster simulations, averaged over all masses. While this doesn't include the measurement error in estimating the optical depth, it also does not include additional information in the mass dependence of the optical depth that could reduce the intrinsic dispersion estimator through the creation of a fitting function. Possible ways to estimate τ beyond the scope of this chapter include combining thermal SZ and X-ray observations to break the electron temperature-optical depth degeneracy that will partially affect even multi-frequency arcminute resolution observations [148]. This technique relies on theoretical assumptions and modeling to connect the electron temperature to the X-ray temperature, that need more detailed testing against simulations. A polarization sensitive stage IV CMB survey may be able to measure τ by stacking clusters to extract the polarization signal introduced by the scattering, which depends directly on the optical depth (see e.g. [149]).

To understand the impact of greater uncertainty in the determination of τ on the cosmological constraints, we consider two potential forms of uncertainties, shown in Figure 16. The first is the effect of increased statistical dispersion, σ_τ in the optical depths of the cluster

sample and the second is a systematic offset in the τ. For the latter, we introduce a nuisance parameter, $b_\tau(z)$, in each redshift bin that scales the amplitude of the mean pairwise velocity, $\hat{V}(z) = b_\tau(z)V(z)$, and consider its effect on cosmological constraints when marginalizing over $b_\tau(z)$. Additionally we consider a constant, redshift independent nuisance parameter, b_τ, that scales the amplitude across all clusters. For clarity, when studying the impact of b_τ we remove the σ_τ^2 contribution to the covariance and purely parameterize the uncertainty in τ through a prior on b_τ.

Table 5 shows that for a near-term Stage II survey the noise will be dominated by the instrument accuracy, for a more sensitive Stage III both components become comparable, and for a Stage IV survey the velocity accuracy may be limited by the accuracy of τ. This is reflected in the top panels of Figure 16 in which varying the amplitude of σ_τ between 0 and 1000 km/s only minimally changes the constraints on the dark energy FoM and the constraints on γ for Stage II and III.

For Stage II and Stage III surveys, conclusions for the effect of b_τ on w_0 and w_a are similar to those for σ_τ. The constraints on these dark energy parameters are principally determined by the Planck-like prior, independent of the kSZ constraints, and uncorrelated with b_τ. For the Stage IV survey the kSZ constraints provide additional constraints on the equation of state, increasing their correlation with b_τ, and the prior has a more pronounced effect on improving the FoM once below $\Delta b_\tau \lesssim 10^{-1}$. Equivalently Stage II and III are not affected by the assumptions on the τ bias model; marginalizing over the amplitude in each redshift bin yields similar results to introducing a constant bias factor across all redshifts. For Stage IV slightly larger FoM are achieved for a redshift independent b_τ model without imposing any prior.

For the growth parameter, which is predominantly constrained by the kSZ data, the model assumptions on the τ nuisance parameter are more important. Marginalizing over the amplitude in each redshift bin, $b_\tau(z)$, without imposing any prior doubles the uncertainty in γ

compared to a constant, redshift independent nuisance parameter b_τ. The difference between this behavior and the FoM constraints (shown in Figure 16 lower panels) indicates that the redshift dependence of the FoM versus γ helps to break the degeneracy between them. A prior on the bias $\Delta b_\tau \lesssim 10^{-1}$ leads to a factor of 5 to 10 improvement in the parameter constraints for the redshift dependent $b_\tau(z)$ model and a factor of 3 to 4 improvement for a constant b_τ. For the Stage IV survey we find that the multiple-redshift bins and improved covariance reduce the degeneracy between the τ bias parameter and γ, so that the systematic bias and the growth parameter can be constrained simultaneously by the data, and the prior has less effect.

Beyond uncertainties in τ, the measurement uncertainty also depends on the peculiar velocity of the cluster, see (3.2.22). Even though the peculiar velocities of clusters are in principle distributed over a range of velocities, here for simplicity we assume a rms velocity of $v = 300$ km/s that corresponds to the peak velocity of the distribution found in simulations [150] for all clusters to calculate the total measurement error. Fortunately the peak velocity does not strongly depend on the mass of the cluster [150]. While future observations will reduce the velocity measurement uncertainty, there is an irreducible error of around $\sigma_v = (50 - 100)$ km/s on the cluster peculiar motion due to internal motion within the cluster [151, 152]) that will ultimately limit the CMB observations.

V Dependency on the Modified Gravity parametrization

In the previous sections we parametrized modified gravity models using one extra parameter γ that is assumed constant across all redshifts. Not all modified gravity models are well represented by such a simple parameterization. Some models are better fit by a more general parametrization that allows for a monotonic redshift dependence in γ, $\gamma(a) = \gamma_0 + (1 - a)\gamma_a$ [153], equivalent to the dark energy $w_0 - w_a$ model. Table 8 summarizes the FoM as well as the 1σ constraints on $\{w_0,w_a,\gamma_0,\gamma_a\}$. Introducing an additional extra parameter loosens the

constraints on the parameters with the advantage of imposing a smaller theoretical prior on modified gravity. Figure 17 shows the 1σ and 2σ constraints on $\gamma_0 - \gamma_a$ for Stage II, III and IV.

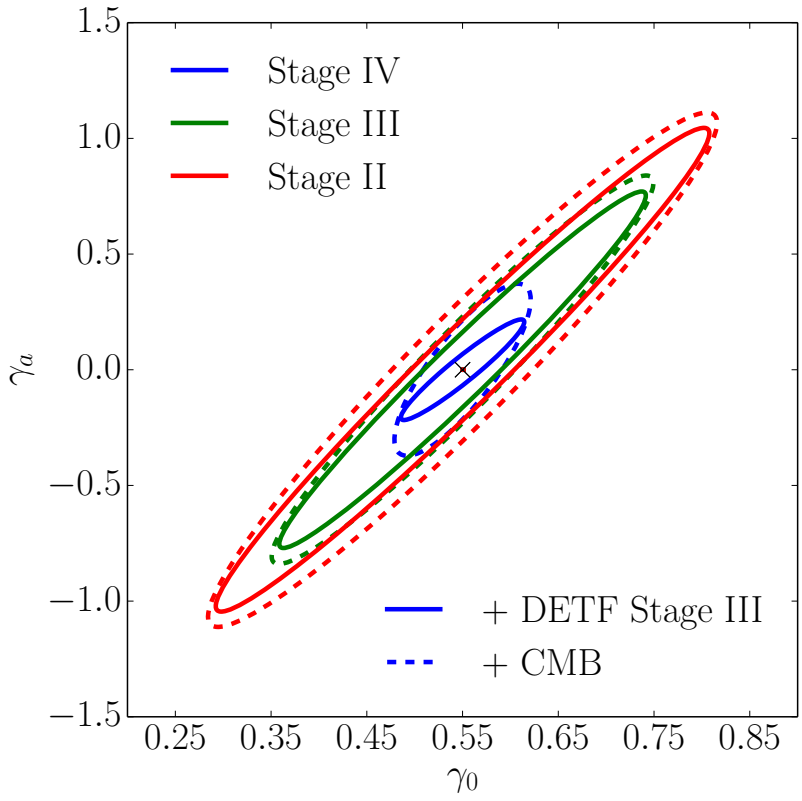

Figure 17: Marginalized constraints on the $\gamma_0 - \gamma_a$ parameter space showing the 68% confidence contours for the pairwise velocity constraints in combination with a Planck-like (dashed) or DETF Stage III (solid) prior on all parameters except γ_0 and γ_a. The fiducial model assumes GR with $\gamma_0 = 0.55$ and $\gamma_a = 0$.

An even more general approach is to directly constrain the growth rate in redshift bins as a 'model-independent' way. This approach is particularly applicable for spectroscopic galaxy surveys which can isolate peculiar velocity data, and hence the growth rate, in precise redshift bins. In Figure 18 we present the forecasts for this parametrization. We find, in combination with the Stage III DETF constraints on the equation of state, an uncertainty in f_g of around 2% at $z \sim 0.3 - 0.6$ for Stage IV surveys. These constraints provide a complementary measurement to the growth rate measurements from redshift space clustering

	$\gamma = \gamma_0 + \gamma_a(1-a)$		
	Stage II	Stage III	Stage IV
FoM_{MG}	127	137	211
$\sigma(w_0)$	0.10	0.09	0.07
$\sigma(w_a)$	0.29	0.28	0.23
$\Delta\gamma_0/\gamma_0$	0.31	0.23	0.08
$\sigma(\gamma_a)$	0.69	0.51	0.14

Table 8: A summary of the dark energy FoM and 1σ marginalized constraints on for the dark energy parameters in the $\gamma_0 - \gamma_a$ parametrization for Stage II, III and IV scenarios in combination with a DETF prior on all parameters except γ_0 and γ_a.

of emission line galaxies (ELGs) and LRGs with a DESI-like survey. On its own, without the additional DETF stage III data, forecasts for DESI project 1.4-1.6% errors on the growth factor multiplied by σ_8 over a comparable redshift range to that considered in our analysis [53]. DESI, along with Euclid [143] and WFIRST [51] will also provide complementary spectroscopic constraints on the growth rate at higher redshifts, $1 < z < 3$.

3.4 Conclusions

Recent analyses have demonstrated that the kSZ can be successfully extracted from sub arcminute resolution CMB maps by cross-correlating them with cluster positions and redshift from spectroscopic LSS surveys. In this chapter we have considered the potential to apply this technique, in light of planned CMB and LSS surveys with greater sensitivity and larger areas, to constrain dark energy and modifications to gravity on cosmic scales using the mean pairwise velocity of clusters as an observable. We have extended the model presented in [131] to account for the dependence on the binning in cluster separations, shot noise, and potential contributions to the total covariance matrix due to small number densities, that we show are significant, despite being frequently neglected, and provided a detailed derivation of the

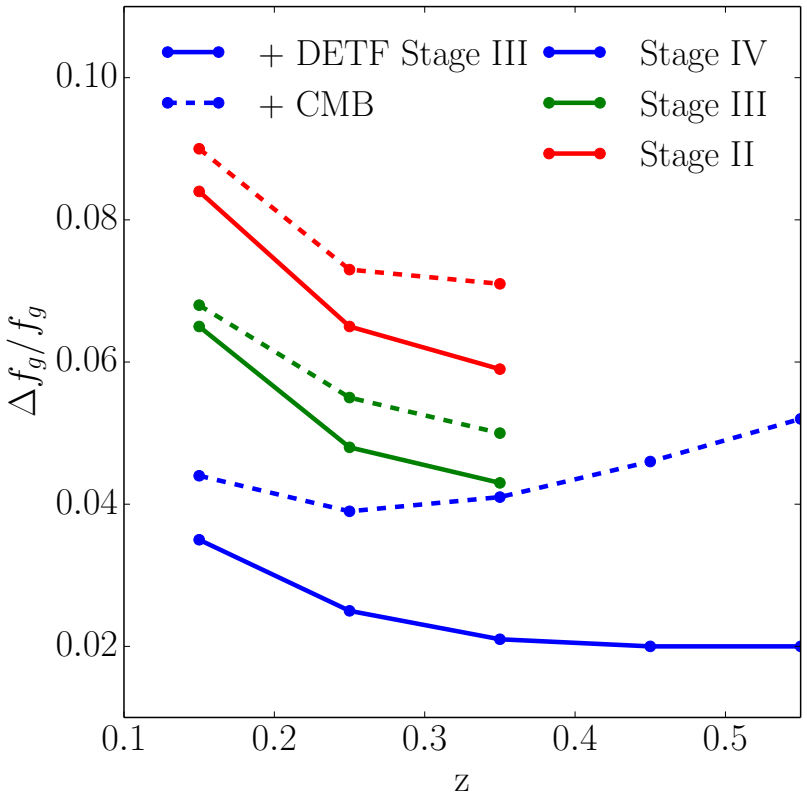

Figure 18: Expected fractional 1σ errors on the growth rate, f_g, in each redshift bin for Stage II (red), Stage III (green) and Stage IV (blue) when combined with a Planck-like CMB (dashed) or DETF Stage III (solid) prior on all parameters except $f_g(z)$.

covariance components.

The projected constraints are intimately related to not only the quality of future data, determined by the instrumental precision, but also to the modeling of the uncertainties in transforming the kSZ observations into velocity estimates that constrain the LSS growth history. We investigate a range of uncertainties, using reasonable assumptions based on simulations and projected survey capabilities. We also study the sensitivity to assumptions by varying theoretical priors to understand and estimate the robustness of the results. We included a study of the effect of survey assumptions on the minimum detectable cluster mass and the minimum cluster separation that could be included, in light of the influence of nonlinear effects in the cluster motions and correlations.

The mean pairwise velocity is modeled assuming linear theory for the underlying matter distribution as well as the halo bias. Variations in the equation of state and the growth rate affect the linear growth factor in similar ways, that leads to degenerate effects on the pairwise velocity amplitude. However, the different redshift dependence of these effects helps to break the degeneracy, and constraints on the expansion history, such as those from Type 1a supernovae, BAO and CMB geometric constraints, break it further, allowing growth information to be extracted from the kSZ.

The cluster sample's minimum mass has a significant impact on the predicted constraints. A smaller minimum mass leads to an increase of the number of clusters in the catalog (assuming the catalog is nearly complete) and significantly reduces the errors on all cosmological parameters. Assuming an optimistic mass cut-off for the upcoming cluster catalogs leads to an improvement on the FoM (including CMB priors) from $\mathrm{FoM_{GR}} = 47$ to $\mathrm{FoM_{GR}} = 195$ and a reduction of the 1σ uncertainty of the modified gravity parameter γ from 5% to 2% for a Stage IV survey compared to our fiducial assumption.

In contrast, the uncertainty in the exact minimum mass had only a mild impact on the dark energy and modified gravity constraints. This was understood in terms of the additional effect of the minimum mass on the shape, as a function of cluster pair separation, as well as amplitude, of the pairwise velocity. Marginalizing over the minimum mass, while imposing a 15% prior in our analysis, in a scenario in which the covariance remains unchanged, reduces the FoM for a Stage IV survey from $\mathrm{FoM_{GR}} = 47$ to $\mathrm{FoM_{GR}} = 29$ and marginally loosens the constrains on γ since the mean pairwise velocity is only weakly dependent on the assumed mass cut-off. In comparison to the abundance of clusters as a cosmological probe, the mean pairwise velocity of clusters appears to be more robust to uncertainties in the mass calibration.

Considering pairwise correlations down to cluster separations of $r = 5$ Mpc/h halves the error on γ compared to an analysis that excludes all scales below $r = 50$ Mpc/h. While extending the analysis to smaller separations could significantly improve the constraints,

including scales in the nonlinear regime without accurate modeling could also potentially bias the constraints and introduce more systematic uncertainties.

Improved constraints on τ in clusters are critical for accurate extraction of cluster streaming velocities from kSZ measurements. We studied the impact of uncertainties in the τ measurement by considering constraints as we varied the level of statistical uncertainty in individual cluster τ measurements and, separately, the effect of a systematic offset in the τ determinations. The later was parametrized by a multiplicative bias parameter in each redshift bin, $b_\tau(z)$, as well as a constant, redshift independent bias, b_τ. We found that the effect of σ_τ on the dark energy FoM was minimal reflecting that the principal constraints come from the external CMB or DETF prior. For Stage IV, in particular, the dispersion in τ does have a notable impact on the growth factor constraints as the instrument contribution to the measurement error and shot noise contributions have decreased. For the systematic offset in τ, we found that the prior on b_τ or $b_\tau(z)$ had the biggest impact for Stage II and Stage III surveys for which significant degeneracies exist between the τ bias and γ. Though, a $\sim$10% prior on the amplitude of τ enables these surveys to provide competitive constraints. For a Stage IV survey and a b_τ bias model, the redshift bins and reduced covariance allowed both b_τ and γ to be extracted from the data without the need for a prior on τ.

In addition to a minimal model to modify gravity, in which a modification to the growth rate is parametrized by a single parameter, γ, we also predict constraints for more general modified gravity parametrization. We use a γ parametrization that monotonically varies with the scale factor, and a model independent approach of measuring the growth rate as a function of redshift, $f_g(z)$, directly. We forecast $\sim 6-8\%$ 1σ errors on f_g for Stage II, $4-6\%$ for Stage III and $2-3\%$ constraints for Stage IV when combined with a Stage III DETF constraints on the expansion history.

Potential improvements in the covariance could include taking advantage of multi-frequency information available in upcoming surveys (e.g. [125, 126]) to improve the kSZ signal

extraction and reduce the measurement error. Larger LRG catalogs could also be used, such as in the first kSZ detection; however, this increases uncertainty in the minimum mass of the cluster sample. Similarly, with the improvements in cluster photometric redshift uncertainties that are coming from improved algorithms and spectroscopic training sets, it may be feasible to use photometric surveys, without spectroscopic follow up, to significantly enlarge the cluster sample. This will degrade the redshift accuracy, and therefore the measurements of the cluster separation, particularly on small scales; however, the larger sample size will help compensate and might even improve the constraining power.

Measurements of the kSZ effect provide complementary constraints on the growth of structure to weak lensing and redshift space distortion measurements by providing measurements on larger physical scales and using a highly complementary, and more massive, tracer of the cosmological gravitational field, that is not dependent upon a characterization of galaxy bias. Having a variety of cosmological probes of dark energy and modified gravity with different systematics is going to be vital for reducing systematic effects and biases in parameter estimation and determining the properties of dark energy and gravity in a variety of epochs and regimes.

Chapter 4

Constraints on massive neutrinos from the pairwise kinematic Sunyaev-Zel'dovich effect

Contents

4.1 Introduction

To achieve precision cosmology and reduce systematic effects measurements from a variety of different cosmological observations are necessary. In this chapter we consider CMB secondary anisotropies, specifically the mean pairwise velocity of clusters as observed through the kinematic Sunyaev-Zel'dovich (kSZ) effect [47], as a novel probe of neutrino properties, complementary to large scale structure (LSS) probes. Previously, we studied the potential of using kSZ measurements to test dark energy and modified gravity models [2]. In this chapter we extend the standard ΛCDM parameter space to massive neutrinos, parametrized in terms of $\sum m_\nu$, and forecast constrains on $\sum m_\nu$ from upcoming surveys.

The chapter is organized as follows. In Section 4.2 we: a) give a summary of the effect of massive neutrinos on the power spectrum, halo mass function (HMF), and the growth rate, b) present the formalism of the pairwise statistics of clusters in ΛCDM cosmological models including massive neutrinos, and c) describe modeling of the covariance matrix and nuisance parameters as well as survey assumptions. In Section 4.3 we describe our analysis and present results before concluding in Section 4.4.

4.2 Formalism

I Cosmic structure and massive neutrinos

We provide a short summary of the cosmological effects of massive neutrinos, focusing on the effect of massive neutrinos on the LSS, and point the reader to [154, 155, 156] as helpful reviews for more details.

Neutrinos cannot be confined on scales below their free-streaming scale, $k_{\rm fs}$, given by

$$k_{\rm fs}(z) = 0.8\frac{\Omega_\Lambda + \Omega_m(1+z)^3}{(1+z)^2}\left(\frac{m_\nu}{1\ {\rm eV}}\right)\ {\rm h\ Mpc^{-1}} \tag{4.2.1}$$

where Ω_m and Ω_Λ are the matter and Λ energy density of today and therefore suppress the matter power spectrum for $k > k_{\rm fs}$. Note that different neutrino masses have different free-streaming wave numbers, leaving LSS not only sensitive to the total neutrino mass but potentially also to individual masses. We calculate the matter power spectrum using CAMB [157] and taking the effect of massive neutrinos into account.

The universality of the halo mass function in the context of massive neutrino cosmologies has been studied in detail (e.g., [158, 159]). It was found that the halo mass function as well as the halo bias is more accurately described if only the cold dark matter and baryonic matter components, $\Omega_m - \Omega_\nu$, are taken into account when calculating the halo mass function rather than the total mass, $\Omega_m = \Omega_{\rm cdm} + \Omega_b + \Omega_\nu$. Following [159] we will denote the cold

dark matter and baryonic component as "cold" matter (subscript "c") in contrast to total matter that includes the neutrino mass (subscript "m"). The comoving number density of halos per unit mass, $dn(M)/dM$, can then be modeled in the common form

$$\frac{dn(M,z)}{dM} = \frac{\rho_c}{M} f(\sigma_c, z) \frac{d\ln\sigma_c^{-1}}{dM}, \tag{4.2.2}$$

using $\rho_c = \rho_{\rm cdm} + \rho_b$ as the background matter density and with the rms of the linear cold matter density field given by

$$\sigma_c^2(M,z) = \int d^3k P_{\rm lin}^{cc}(k,z) W^2(Rk), \tag{4.2.3}$$

where $P_{\rm lin}^{cc}$ is the linear cold matter power spectrum and the scale R is given by $M = \frac{4\pi}{3}\rho_c R^3$. Many different fitting functions have been proposed within the literature, however, for the purpose of this work the choice of halo mass function has little effect. Here we adopt the fitting function given in [160] to parametrize the halo multiplicity function, $f(\sigma_c, z)$.

Similarly we define the halo bias with respect to the cold matter, $b_c(M,z)$, using the description given in [160].

The growth rate, f_g, is defined as

$$f_g(a) \equiv \frac{d\ln D(a)}{d\ln a}, \tag{4.2.4}$$

with the growth factor, $D(a)$, normalized to $D(a_0) = 1$, and becomes scale dependent in the presence of massive neutrinos. Here we use the fitting function

$$f_g(z,k) \approx \mu(k)\Omega_m^\gamma(z), \tag{4.2.5}$$

where

$$\mu(k) = 1 - A(k)\Omega_\Lambda f_\nu + B(k) f_\nu^2 - C(k) f_\nu^3 \tag{4.2.6}$$

with $A(k)$, $B(k)$, $C(k)$ given in Table II of [161] and with the growth exponent, γ, parametrized as $\gamma = 0.55 + 0.05[1 + w(z=1)]$ [30].

II Motion of clusters as a probe of massive neutrinos

The mean pairwise velocity of clusters can be modeled [130, 131, 2] as

$$V(r,a) = -\frac{2}{3}H(a)a\ \Omega_m^{\gamma}(a)\frac{r\bar{\xi}_h(r,a)}{1+\xi_h(r,a)}, \tag{4.2.7}$$

with ξ_h and $\bar{\xi}_h$ given by

$$\xi_h(r,a) = \frac{1}{2\pi^2}\int dk k^2 j_0(kr)P_{\rm lin}(k,a)b_{h,c}^{(2)}(k), \tag{4.2.8}$$

$$\bar{\xi}_h(r,a) = \frac{3}{r^3}\int_0^r dr' r'^2 \mu(k,a)\xi(r',a)b_{h,c}^{(1)}(k), \tag{4.2.9}$$

where $P_{\rm lin}$ is the linear, total matter power spectrum and $b_{h,c}^{(q)}$ are the moments of the halo bias defined as

$$b_{h,c}^{(q)} = \frac{\int dM\ M\ n(M,z)b_c^q(M,z)W^2[kR]}{\int dM\ M\ n(M,z)W^2[kR]}. \tag{4.2.10}$$

assuming a Gaussian window function with $M(R) = (2\pi)^{3/2}\,\rho_c R^3$. Note that the moments of the halo bias are taken with respect to the halo mass function and halo bias, including the effect of massive neutrinos as described above.

Figure 19 shows the mean pairwise velocity of clusters for different neutrino masses assuming a normal hierarchy fixing all other cosmological parameters, including $\Omega_m h^2$ and A_s, to fiducial values. Note that fixing A_s and $\Omega_m h^2$ while increasing the neutrino mass leads to decreasing σ_8 and $\Omega_{\rm cdm}h^2$ values which corresponds to an increase in the halo bias. The suppression of the dark matter power spectrum at large k leads to a suppression of $V(r)$ at small separations, while at large r the effect of massive neutrinos on the halo bias dominates. The mass of the neutrinos leaves an r-dependent imprint on $V(r)$, which enables us to differentiate between the mass of the neutrinos and other cosmological parameters and systematic effects that primarily change the overall amplitude of $V(r)$. Figure 20 displays the mild sensitivity of $V(r)$ to the different neutrino hierarchies.

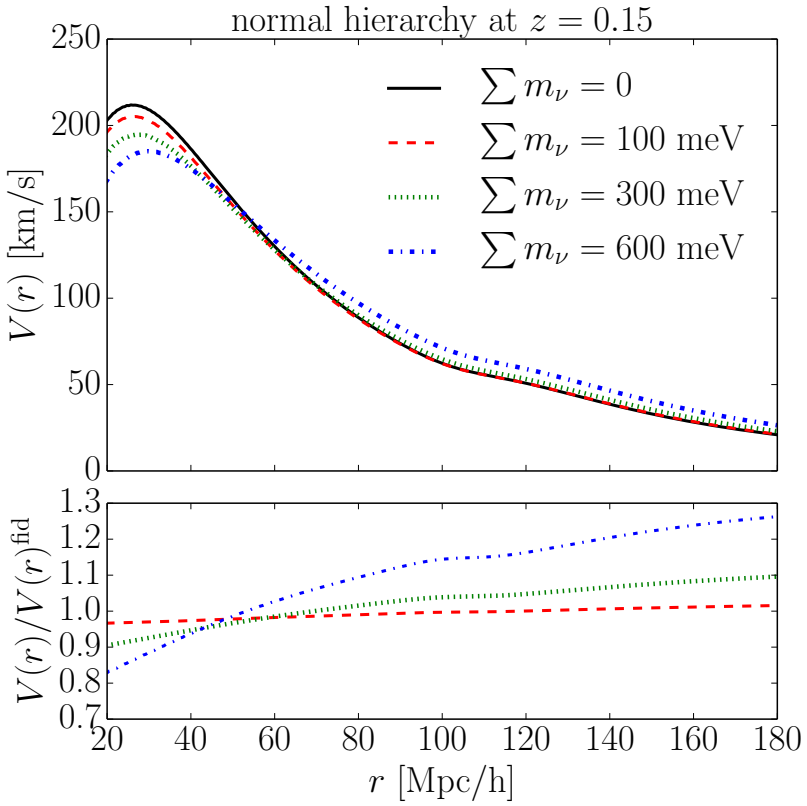

Figure 19: [Upper panel]: The mean pairwise cluster velocity, $V(r)$, for different neutrino mass sums, $\sum m_\nu$. $V(r)$ is calculated at $z = 0.15$ and assuming a minimum cluster mass of $M_{\rm min} = 1 \times 10^{14}\ M_\odot$ with other cosmological parameters, including $\Omega_m h^2$ and A_s, fixed to fiducial values. Here we assume a normal neutrino hierarchy ($m_1 \approx m_2 \approx 0, m_3 \neq 0$). [Lower panel]: Ratio of the mean pairwise velocity, $V(r)$, for the different scenarios to the fiducial model with $\sum m_\nu = 0$ (black line in upper panel). Massive neutrinos clearly leave a scale-dependent imprint on $V(r)$, which is highlighted by the different slopes of the lower curves.

III General methodology and survey assumptions

We use the Fisher matrix approach to estimate the covariance matrix between parameters p_μ and p_ν, $C_{\mu\nu} = F^{-1}_{\mu\nu}$, with

$$F_{\mu\nu} = \sum_i^{N_z} \sum_{p,q}^{N_r} \frac{\partial V(r_p, z_i)}{\partial p_\mu} {\rm Cov}_i^{-1}(r_p, r_q, z_i) \frac{\partial V(r_p, z_i)}{\partial p_\nu}, \tag{4.2.11}$$

where ${\rm Cov}(r_p, r_q, z_i)$ is the covariance matrix, as defined in [2], between two clusters pairs at redshift z_i with each pair having comoving separations of r_p and r_q, including cosmic variance,

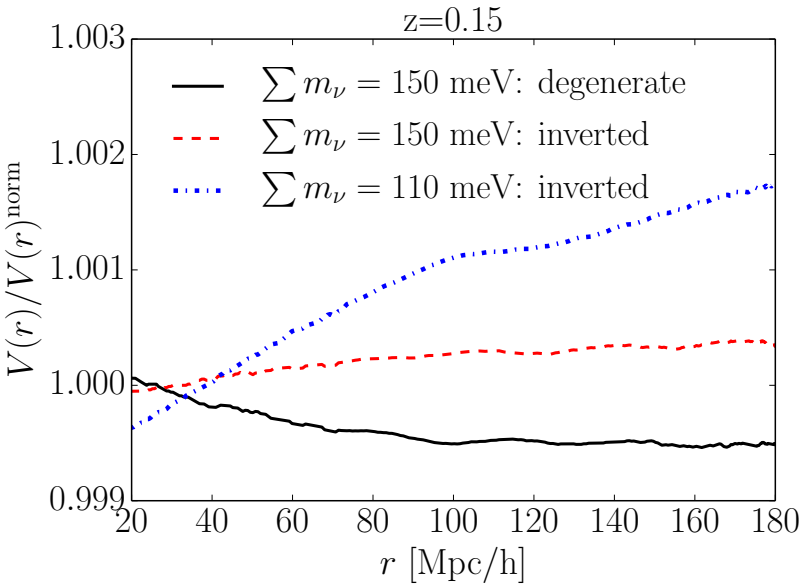

Figure 20: Ratio of the mean pairwise velocity, $V(r)$, for the different neutrino models to the normal hierarchy ($m_1 < m_2 \ll m_3$) , $V(r)^{\rm norm}$. The inverted hierarchy ($m_3 \ll m_1 \simeq m_2$) deviates more strongly from the normal hierarchy assuming a total mass of $\sum m_\nu = 110$ meV (blue, dashed-dotted line) than for $\sum m_\nu = 150$ meV (red, dashed line). A degenerate model ($m_1 \approx m_2 \approx m_3$, black, solid line) with $\sum m_\nu = 150$ meV exhibits a slightly different behavior from the normal and inverted hierarchies. This shows that there is a mild sensitivity to the different masses of the individual neutrinos even when $\sum m_\nu$ is constant.

shot noise and a measurement uncertainty due to the sensitivity of the CMB instrument (given in [2] Table III). N_z and N_r are the number of redshift and spatial separation bins, respectively.

The kSZ effect is proportional to the mean pairwise momentum of clusters, $\sim \tau v$. In order to accurately measure cluster velocities, the average cluster optical depth and its dependency on mass and redshift must be known. The optical depth can be modeled, for instance using hydrodynamical simulations [141], or constrained using complementary cluster data such as CMB polarization [149]. We allow large uncertainties in the cluster optical depth that could introduce systematic biases in $V(r)$ by marginalizing over a potential bias, defined via $\hat{V}(z_i) = b_\tau(z_i)V(z_i)$, that scales the amplitude in each redshift slice. We also introduce the limiting cluster mass of the sample as a nuisance parameter in our analysis, imposing a 15%

prior.

We consider two sets of cosmological parameters. The first is a minimal six-parameter flat ΛCDM cosmological model plus the neutrino mass sum and $(1+N_z)$ nuisance parameters, which we denote as ΛM(ixed)DM and summarize as

$$\begin{aligned} \mathbf{p}_{\rm min} &= \{\Omega_b h^2, \Omega_m h^2, \Omega_\Lambda, n_s, \log(10^{10} A_s), \sum m_\nu\} \\ &\quad + \{M_{\rm min}, b_\tau(z)\}, \end{aligned} \tag{4.2.12}$$

where Ω_b, Ω_m, Ω_Λ are the dimensionless baryon, matter and dark energy densities respectively; h is the Hubble constant in units of 100 km/s/Mpc; n_s and A_s are the spectral index and normalization of the primordial spectrum of curvature perturbations; $M_{\rm min}$ is the limiting cluster mass of the catalog; and b_τ the nuisance parameter due to uncertainty in τ. The matter energy density includes cold dark matter, baryons, and the neutrino mass contribution, i.e. $\Omega_m = \Omega_{\rm cdm} + \Omega_b + \Omega_\nu$, where Ω_ν is the neutrino energy density, related to the neutrino mass via $\Omega_\nu = \sum m_\nu/(93.14\ h^2{\rm eV})$ (see e.g., [155]). The second set of parameters is a more general ΛMDM model that also includes the curvature energy density, Ω_k, and the dark energy equation of state parameters, w_0 and w_a, such that the equation of state is $w(a) = w_0 + (1-a)w_a$, or

$$\mathbf{p} = \mathbf{p}_{\rm min} + \{\Omega_k, w_0, w_a\}. \tag{4.2.13}$$

We adopt the fiducial values assumed in the Euclid Assessment Study report [50], $\omega_b = 0.021805, \omega_m = 0.1225, \Omega_\Lambda = 0.75, n_s = 1, \log(10^{10} A_s) = 3.2336, \Omega_k = 0, w_0 = -0.95, w_a = 0$ which corresponds to $\Omega_m = 0.25, \Omega_b = 0.0445, h = 0.7$ and $\sigma_8 = 0.8$. For the CMB Fisher matrix we also marginalize over the reionization optical depth with fiducial value $\tau_0 = 0.11$. We assume a normal hierarchy ($m_1 \approx m_2 \approx 0, m_3 \neq 0$) as our reference case with the fiducial total neutrino mass, $\sum m_\nu = 60$ meV. We find that our results are robust to the assumed fiducial cosmology, including the fiducial neutrino mass, and only show a mild sensitivity to the assumed neutrino hierarchy.

The kSZ effect can be extracted by cross-correlating the CMB surveys with cluster positions and redshifts, using LRGs as a tracer for clusters or by using a photometrical selected cluster catalog such as RedMApper [138]. In this work we consider three potential surveys: Stage II - ACTPol [123] cross-correlated with BOSS [162], Stage III - Advanced ACTPol [163] and BOSS, and Stage IV - CMB Stage IV [40] and DESI [53]. Details of the survey assumptions, including redshift range, overlapping sky coverage between CMB and LSS surveys, and the minimum cluster mass of the potential cluster catalogs, are summarized in Table 9.

		Survey Stage		
Survey	Parameters	II	III	IV
CMB	$\Delta T_{\rm instr}$ (μKarcmin)	20	7	1
Galaxy	$z_{\rm min}$	0.1	0.1	0.1
	$z_{\rm max}$	0.4	0.4	0.6
	No. of z bins, N_z	3	3	5
	$M_{\rm min}$ (10^{14} $M_\odot$)	1	1	0.6
Overlap	Area (1000 sq. deg.)	4	6	10

Table 9: Reference survey specifications used to model Stage II, III and IV kSZ cluster surveys. The expected instrument sensitivity of the CMB survey, $\Delta T_{\rm inst}$, along with the assumed optical LSS survey redshift range $z_{\rm min} < z < z_{\rm max}$, redshift binning, and minimum detectable cluster mass $M_{\rm min}$ are shown. We consider an effective sky coverage by estimating the degree of overlap between the respective CMB and optically selected cluster data sets.

We are conservative in our survey specifications by assuming a photometrical selected cluster catalog, to ensure completeness and purity of our sample, with spectroscopically selected LRGs to give cluster redshifts. We also only assume single frequency, 150 GHz, CMB measurements (even though, e.g., Advanced ACTPol will have five frequency bands). The assumed sky coverage for the kSZ analysis is subsequently limited by the overlapping area of photometric and spectroscopic LSS surveys with CMB kSZ measurements. The assumed redshift range is given by that for the spectroscopic LRG sample, and the limiting mass is motivated by the expected, photometrically selected cluster catalogs. A more detailed

discussion can be found in [2].

In addition to the fiducial scenario, we consider a more optimistic lower cluster mass limit of $M_{\rm min} = 4 \times 10^{13}\ M_\odot$ for Stages II, III and $M_{\rm min} = 1 \times 10^{13}\ M_\odot$ for Stage IV. For our CMB priors we use the survey specification for a Planck-like survey, including primordial temperature and polarization as well as lensing information, as given in [164].

4.3 Analysis

Potential kSZ constraints on massive neutrinos

The results of our Fisher matrix analysis, the forecast 1-σ errors on the total neutrino mass $\sum m_\nu$, are displayed in Table 10 for our fiducial case as well as more optimistic assumptions on the τ bias parameter and limiting mass. The left-hand columns of Table 10 depict the most conservative scenario in which we treat the mass-averaged optical depth of clusters τ as an unknown nuisance parameter in each redshift bin, $b_\tau(z)$, that scales the overall amplitude of the mean pairwise velocity, $V(r)$. Under this assumption the optical depth of clusters can scale the overall amplitude of $V(r)$ but has no r-dependent effect. The scenarios depicted in the middle and right columns show less conservative assumptions on the limiting mass (middle) as well as adding a 1% prior on $b_\tau(z)$ (right).

With kSZ measurements alone, the total neutrino mass is degenerate with other cosmological parameters, in particular with the matter density $\Omega_m h^2$ and the dark energy equation of state parameters w_0 and w_a. Since kSZ data alone cannot constrain the cosmological background parameters well [2], the predicted error on the total neutrino mass is comparatively loose. The forecasted 68% upper limit on the total neutrino mass with kSZ data only is 1300, 810 and 280 meV for Stage II, III and IV respectively for the minimal ΛMDM cosmology in our most conservative scenario. In comparison, our projected Planck constraints are 540 meV using the primordial temperature and polarization power spectrum and 200 meV when

		$\sigma(\sum m_\nu)$ in meV								
		no prior on b_τ			no prior on b_τ, opt. $M_{\rm min}$			1% prior on b_τ, opt. $M_{\rm min}$		
		Stg. II	Stg. III	Stg. IV	Stg. II	Stg. III	Stg. IV	Stg. II	Stg. III	Stg. IV
kSZ+Planck	Minimal ΛMDM	310	240	110	180	140	64	100	85	33
	$+\Omega_k, w_0, w_a$	520	470	220	430	360	120	220	210	99
kSZ+Planck+lens	Minimal ΛMDM	74	70	47	64	58	30	63	57	28
	$+\Omega_k, w_0, w_a$	87	85	79	84	83	68	81	79	60

Table 10: Forecasts for 1σ errors on $\sum m_\nu$ for a normal hierarchy. [Left columns]: Results marginalizing over b_τ [top row] marginalized constraints (top row) on the sum of the neutrinos mass for the kSZ surveys including Planck primordial CMB priors for a five-parameter minimal ΛMDM cosmology $+\sum m_\nu$ as well as (second row) including Ω_k, w_0, w_a; and (lower rows) similar results also including Planck lensing constraints. [Middle columns]: Assuming a more optimistic optically selected mass cutoff of $M_{\rm min} = 4 \times 10^{13}\ M_\odot$ for Stages II and III and $M_{\rm min} = 1 \times 10^{13}\ M_\odot$ for Stage IV, relative to the fiducial scenarios of $M_{\rm min} = 10^{14}\ M_\odot$ (Stages II and III) and $M_{\rm min} = 6 \times 10^{13}\ M_\odot$ (Stage IV). [Right columns] Including a 1% prior on b_τ and optimistic assumptions on the minimum mass. The CMB Planck priors alone provide $\sigma(\sum m_\nu) = 540$ (660) meV for a minimal (general) ΛMDM cosmology and $\sigma(\sum m_\nu) = 200$ (240) meV including CMB lensing.

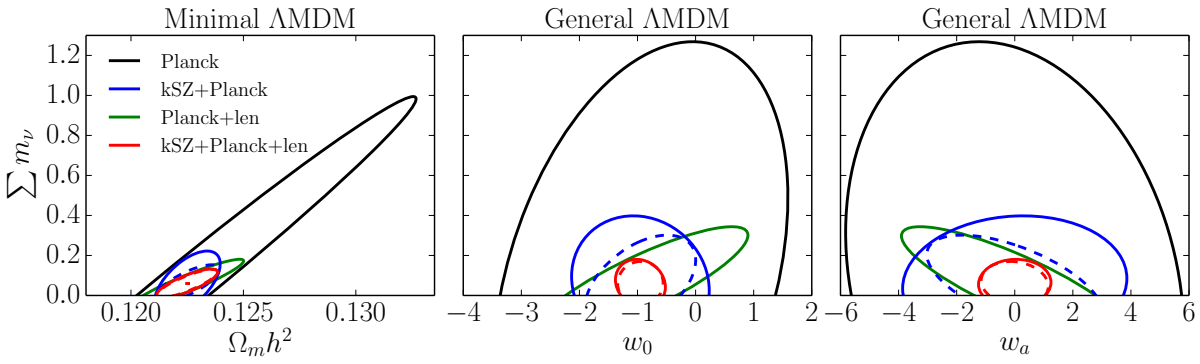

Figure 21: Constraints on the neutrino mass sum, $\sum m_\nu$, versus the matter density, $\Omega_m h^2$ (left); the dark energy equation of state, w_0 (middle); and its evolution, w_a (right). Contours show 2D 68% confidence levels for the following data sets: Planck (black), Planck and kSZ Stage IV (blue), Planck including CMB lensing (green), and Planck including CMB lensing plus kSZ Stage IV(red). Solid lines assume no prior on the average cluster optical depth evolution, $b_\tau(z)$, while dashed lines assume a 1% prior on $b_\tau(z)$.

including lensing.

Adding primordial CMB data from Planck can improve the constraints significantly by breaking degeneracies with the other parameters. For a minimal ΛMDM cosmology in combination with Planck CMB results, kSZ measurements can improve constraints on $\sum m_\nu$ and achieve 310, 240 and 110 meV at 68% confidence level for Stage II, III and IV with no prior on $b_\tau(z)$. Marginalizing over the overall amplitude in each redshift bin does not deteriorate the constraints significantly. This can be understood considering the scale-dependent effect of the neutrino mass on $V(r)$, see Figure (19). The r-dependent change of $V(r)$ due to massive neutrinos cannot be compensated by an overall shift of the amplitude of $V(r)$; therefore there is not a strong degeneracy between $\sum m_\nu$ and b_τ. Remarkably, even without prior knowledge of the average cluster optical depth, τ, the kSZ data set should significantly improve upon the Planck constraints (see Figure 21).

Incompleteness of the survey on the sky or substantial variation in the depth of the survey could potentially yield to an inaccurate estimate of the minimum mass of the sample introducing a scale dependence. However, loosening the prior on the limiting mass to account

for this effect only mildly affects the results when the CMB information is included. Doubling the prior on the minimum mass to 30% changes the results on the neutrino mass by less than 8%.

The CMB contains additional information related to $\sum m_\nu$ due to gravitational lensing by LSS. We compare the relative potential constraints by including the information from Planck CMB lensing as a separate case. In Table 10, *Planck* refers to CMB temperature and polarization data only, while *Planck+lens* also includes the forecasts for a Planck CMB lensing extraction performed with a quadratic estimator based on temperature and polarization data [165]. For the minimal ΛMDM cosmology, when including lensing, the expected errors reduce to 74, 70 , and 47 meV. As shown in Figure 21, this represents a considerable improvement relative to constraints from Planck alone plus CMB lensing. We stress that in this analysis we are assuming that the lensing extraction can be performed perfectly from CMB maps, which is an optimistic assumption. On the other hand, the kSZ constraints include relatively conservative assumptions (see §4.2.III). Hence, it is likely that the improvement with respect to CMB data alone achievable with pairwise velocities will be even larger than that presented in this chapter.

The right-hand columns of Table 10 display the results assuming a more optimistic limiting mass of the cluster sample, $M_{\rm min} = 1 \times 10^{13}\ M_\odot$ for Stage IV and $M_{\rm min} = 4 \times 10^{13}\ M_\odot$ for Stage II and III. Under these assumptions, the sum of the total neutrino mass for a Stage IV survey plus CMB priors can be constrained up to 64 meV at 68% confidence level. Imposing a prior on the optical depth bias parameter can further improve the results (see Figure 22). The uncertainty in $\sum m_\nu$ reduces to 100, 85 , and 33 eV (Stage II, III and IV) assuming a 1% prior on the mass-averaged optical depth.

For a more general cosmology including the curvature energy density, Ω_k, and the dark energy equation of state parameters, w_0 and w_a, the kSZ measurement constraints are significantly degraded; however, as shown in Table 10, the constraints remain quite strong

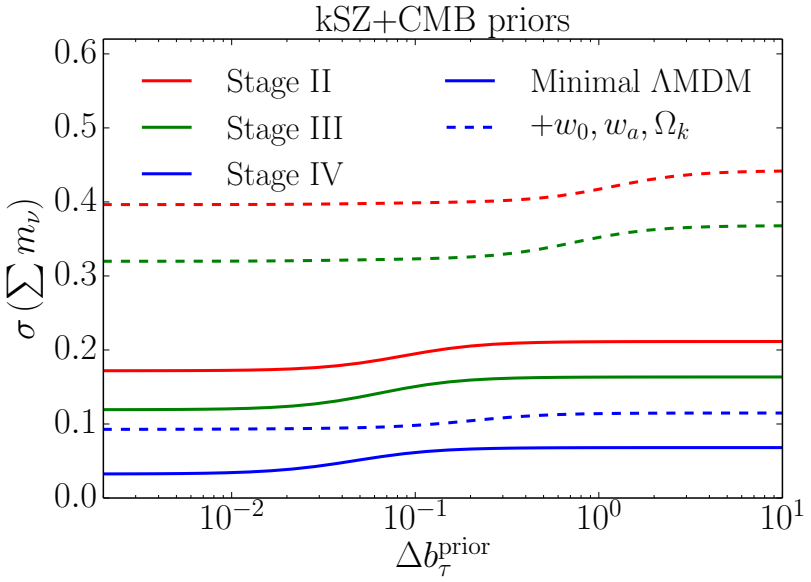

Figure 22: The impact of imposing a prior on a potential systematic offset in the mass-averaged optical depth, parametrized by a multiplicative bias in each redshift bin, b_τ(z), for Stage II (blue), Stage III (green) and Stage IV (red) surveys, on the 1-σ constraints on $\sum m_\nu$. This assumes a mass cutoff of $M_{\rm min} = 4 \times 10^{13}\ M_\odot$ for Stage II and III and $M_{\rm min} = 1 \times 10^{13}\ M_\odot$ for Stage IV as well as including CMB temperature and polarization priors. This shows that $\sum m_\nu$ constraints are more weakly dependent on τ than the dark energy and gravity parameters studied in [2].

when also including Planck lensing measurements to help constrain the background expansion history (see also the discussion in [2]). This highlights the potential power of combining constraints from CMB lensing and kSZ measurements from the same survey instead of relying on the Planck lensing measurements. Here we highlight the sensitivity of kSZ measurements to $\sum m_\nu$ and leave combined lensing and kSZ forecasts to future work.

An important factor that determines the constraining power of kSZ pairwise velocities measurements is the minimum comoving separation achievable by the survey. Photometric surveys would not be able to reconstruct the signal at lower separations as a consequence of the redshift uncertainty. As a test, we have repeated our baseline analysis using a minimum r cutoff $r_{\rm min} = 50$ Mpc/h. This cutoff represents the approximate minimum separation achievable with a photometric survey like the Dark Energy Survey (see, for example, the

discussion in [139]). In this case, while for kSZ data only the constraints deteriorate more than a factor of 2, when including CMB priors from Planck the 1σ error degradation is only $10\% - 20\%$ depending on the survey considered. For example, for a minimal ΛMDM model we find a $\sigma(\sum m_\nu)$ of 90, 89, and 82 meV respectively for Stage II, III and IV surveys, from the combination of kSZ data with Planck CMB + lensing with no prior on b_τ(z).

kSZ measurements from combining LSS and CMB surveys provide an alternative, complementary approach to constraining the neutrino mass sum from using galaxy cluster and CMB measurements independently. For example, Stage IV LRG and emission line galaxy (ELG) clustering forecasts, assuming degenerate massive neutrinos with a total mass $\sum m_\nu = 60$ meV, a minimal ΛMDM cosmology and fiducial values of the cosmological parameters from Planck [166], suggest potential constraints on the neutrino mass, of 24 meV for DESI [142] including a CMB prior and using the galaxy broadband up to $k_{\rm max} = 0.1$ h/Mpc, after accounting for uncertainties in galaxy bias, shot noise and nonlinear damping uncertainties. Similar constraints are forecast for Stage IV CMB surveys alone and improved constraints from combining CMB lensing with galaxy surveys (see e.g., [40]). Adding kSZ measurements should improve these constraints for CMB surveys with the roughly arcminute resolution required for accurate kSZ measurements [163].

4.4 Conclusions

The mean pairwise velocity of clusters, as observed through the kSZ effect, is a novel probe of massive neutrinos. Upcoming kSZ measurements are expected to be comparable in their constraining power to upcoming spectroscopic and photometric galaxy surveys and CMB surveys. Like other LSS probes, the kSZ cannot differentiate strongly between different hierarchies, but can measure the sum of the neutrino mass through its suppression of the matter power spectrum and its effects in the HMF, halo bias and growth rate, as discussed in Section 4.2, leading to a scale-dependent variation in $V(r)$.

Conservative forecasts for kSZ measurements in combination with Planck primordial CMB priors provide constraints on the sum of neutrino masses with a precision of 310, 240, and 110 meV for Stage II, III and IV respectively, assuming a fiducial mass of 60 meV, a normal hierarchy and a minimal ΛMDM cosmology. These constraints include simultaneous constraints on the average optical depth of the cluster sample in different redshift bins by marginalizing over the overall amplitude of $V(r)$ in each bin. The kSZ effect can lead to strong constraints and improve upon Planck results even without precise knowledge of τ, due to the scale-dependent effect of massive neutrinos on $V(r)$. We investigated the uncertainty in the minimum mass of the sample, that could change the scale dependency of the mean pairwise velocity and potentially introduce a bias. The results only show a mild dependency on the uncertainty in the limiting mass. Detailed hydrodynamical simulations could further improve the understanding of potential scale-dependent effects. We leave additional analysis of systematic effects for further studies. More optimistic assumptions on the limiting mass of the cluster sample and the cluster optical depth can improve the results to 100, 85, and 33 meV (Stage II, III and IV). These constraints can be further improved by including CMB lensing measurements.

Our conservative analysis has led to potentially powerful constraints on the cosmic growth history to characterize the properties of neutrinos and other cosmological parameters using the kinematic Sunyaev-Zel'dovich effect. Here we have only considered constraints from Planck satellite data combined with kSZ measurements from cross-correlating spectroscopic galaxy surveys and CMB surveys. CMB polarization and x-ray cluster measurements may allow a refined understanding of cluster optical depth. Upcoming measurements of type 1a supernovae, galaxy clustering, weak lensing, and the CMB have the potential to break degeneracies in kSZ measurements, providing complementary constraints on the expansion history, to give even more stringent constraints on the properties of the dark sector including dark energy and neutrinos.

Chapter 5

Discussion

A central theme of this thesis is the connection of physics beyond the cosmological standard model to cosmological observations, with a focus on dark energy and modified gravity models as well as massive neutrinos. The study of cosmological signatures must go hand in hand with the advancement of effective parametrization of these models, to achieve precision cosmology and to verify underlying physical theories. In this thesis, we have studied the cosmological effects of models within the framework of EFT of gravity, as well as developed and used statistical tools to leverage correlations between complementary spectroscopic LSS surveys and CMB observations. We end by highlighting the main concepts and results of this thesis and outline possible extension of this work.

The EFT approach is a unifying framework to classify both dark energy and modified gravity models. We have studied the effects of additional degrees of freedom, that arise within this framework, on the background expansion of the Universe and assessed their viability and stability by finding dynamical attractor solutions of the cosmological evolution. A large class of possible models can be eliminated by the data because in these models the cosmological background is fundamentally altered. We put constraints on these possible extensions to GR by performing a Monte-Carlo Markov chain likelihood analysis. Gauss-Bonnet models, for instance, that give rise to a late-time de Sitter solution, could confidently be ruled out as dark energy candidates. However, we unfortunately also found that the effect of many other classes of models is not significant enough to achieve meaningful constraints. Higher order

kinetic terms for example leave the cosmological background mainly unaffected and therefore can neither be verified nor dismissed.

The kSZ effect can lead to powerful constraints on dark energy and modified gravity. We explored the possibility of cross-correlating spectroscopic surveys with kSZ measurements to extract the mean pairwise velocity of cluster, $V(r)$, and estimated constraints on dark energy and modified gravity models expected for near term and future surveys, such as ACTPol, eBOSS and DESI. The kSZ observations are directly proportional to the optical depth of the cluster, which is determined by baryonic physics and internal properties of the clusters. We identified the uncertainty in the optical depth of clusters as the limiting factor when extracting cosmological information from the kSZ effect. Information on the optical depth could potentially be provided by hydrodynamical simulations, x-ray measurements or thermal SZ observations. To account for the incompleteness of our knowledge on the optical depth we employed two methods. First, we included an additional term in the covariance of the mean pairwise velocity and second, we introduced and marginalized over a bias parameter, b_τ, that scales the overall amplitude of $V(r)$. Both methods show a severe depletion of the constraining power of the kSZ measurement. However, given that the mass-averaged optical depth of clusters can be modeled accurately up to 10%, the kSZ effect yields tight constraints on modified gravity models complementary to upcoming spectroscopic surveys within the same redshift range.

KSZ measurements are a novel probe of massive neutrinos. In chapter 4, we studied the sensitivity of the mean pairwise velocity of clusters on the sum of neutrino masses. Massive neutrinos leave an imprint on the mean pairwise velocity of clusters through their suppression of the power spectrum and their effect on the growth rate as well as the halo mass function. The scale dependency of this effect seems very promising since it reduces the degeneracy with the optical depth of clusters as well as other cosmological parameters. The constraints on $\sum m_\nu$ are therefore robust to the uncertainty in τ. We estimate 68% upper limits on the neutrino mass sum of 310, 240, 110 meV for "Stage II" (ACTPol +

BOSS), "Stage III" (Advanced ACTPol + BOSS), and "Stage IV" (CMB-S4 + DESI) surveys respectively. For more optimistic assumptions on the limiting mass of the survey, the projected kSZ constraints improve further to 100, 85 and 33 meV (Stage II, III and IV), comparable to conservative Stage IV LSS estimates.

The EFT has been successfully applied to the level of cosmological perturbations [167]. A natural extension of this work is therefore to put constrains on dark energy and modified gravity models on the perturbation level. A first step towards that goal was done in [168]. The extreme wealth in upcoming spectroscopic and photometric surveys as well as CMB experiments will drastically improve upon these constraints. Equivalently, upcoming CMB experiments will enable us to extract cosmological information from the kSZ signal on dark energy models as well as neutrino masses. To fully exploit the kSZ signal, however, we need to further model systematic effects, making use of N-body simulations to model nonlinearities and hydrodynamical simulations to control systematic effect due to baryonic physics within the cluster.

Appendix

Derivation of the mean pairwise velocity covariance

In this section we provide a detailed derivation of the Gaussian and non-Gaussian contributions to the covariance matrix given in equation (3.2.13) in the main text. The covariance matrix specified in (3.2.11) in terms of the volume average of the estimator, $\hat{V}$ of the pairwise velocity V,

$$C_V(r, r') = \langle \hat{V}(r)\hat{V}(r')\rangle - \langle \hat{V}(r)\rangle\langle \hat{V}(r')\rangle. \tag{.1}$$

Let's first consider a covariance between the pairwise cluster velocities of two cluster pairs, each with respective separations r and r', we will then incorporate the effect of including finite bin sizes in the cluster separations. Using the expression for the mean pairwise cluster velocity, given in (3.2.1), the covariance of V can be written as

$$\begin{aligned} C_V(r, a, r', a') &= \frac{1}{1+\xi_h(r,a)}\frac{2}{3}rH(a)af_g(a)\frac{1}{1+\xi_h(r',a')}\frac{2}{3}r'H(a')a'f_g(a') \\ &\times \left[\langle \hat{\bar{\xi}}_h(r)\hat{\bar{\xi}}_h(r')\rangle - \langle \hat{\bar{\xi}}_h(r)\rangle\langle \hat{\bar{\xi}}_h(r')\rangle\right]. \end{aligned} \tag{.2}$$

For simplicity in the following derivation, we drop the subscript "h" (denoting halo) from the correlation function, ξ_h and mass average correlation function, $\bar{\xi}_h$, denoting them respectively by ξ and $\bar{\xi}$. Similarly we use $P(k, a)$ to denote the halo linear dark matter power spectrum, given in full by $P_{\rm lin}^{\rm dm}(k, a)b_h^{(2)}(k)$, and the cluster number density $n_{\rm cl}$ is denoted n.

We define an estimator of the volume averaged correlation function $\bar{\xi}$ equivalently to the

estimator of the correlation function ξ as

$$\begin{aligned}\hat{\bar{\xi}}(\vec{r}) &= \frac{1}{V(\vec{r})}\int_0^{\vec{r}} d^3r_1 \frac{1}{V(\vec{r}_1)}\int d^3x W(\vec{x})\int d^3x' W(\vec{x}')\delta(\vec{x})\delta(\vec{x}')\delta_D^{(3)}(\vec{x}-\vec{x}'-\vec{r}_1) \\ &= \frac{1}{V(\vec{r})}\int_0^{\vec{r}_1} d^3r_1 \int \frac{d^3k}{(2\pi)^3}\int \frac{d^3k_1}{(2\pi)^3}\delta_{\vec{k}}\delta^*_{\vec{k}_1} e^{i\vec{k}_1\vec{r}} h(\vec{k}-\vec{k}_1,\vec{r}_1) \qquad (.3)\end{aligned}$$

where

$$h(\vec{k},\vec{r}) = \frac{1}{V(\vec{r})}\int d^3x e^{i\vec{k}\vec{r}} W(\vec{x})W(\vec{x}+\vec{r}). \qquad (.4)$$

The covariance matrix at a given redshift (dropping the subscript a) becomes

$$\begin{aligned}C_{\bar{\xi}}(\vec{r},\vec{r}') &= \frac{1}{V(\vec{r})}\int_0^{\vec{r}} d^3r_1 \frac{1}{V(\vec{r}')}\int_0^{\vec{r}'} d^3r_1' \int \frac{d^3k}{(2\pi)^3}\int \frac{d^3k_1}{(2\pi)^3} e^{i\vec{k}_1\vec{r}_1} h(\vec{k}-\vec{k}_1,\vec{r}_1) \\ &\times \int \frac{d^3k'}{(2\pi)^3}\int \frac{d^3k_1'}{(2\pi)^3} e^{i\vec{k'}_1\vec{r'}_1} h(\vec{k'}-\vec{k'}_1,\vec{r}_1') \\ &\times \left[\langle \delta_{\vec{k}}\delta^*_{\vec{k}_1}\delta_{\vec{k}'}\delta^*_{\vec{k}_1'}\rangle - \langle\delta_{\vec{k}}\delta^*_{\vec{k}_1}\rangle\langle\delta_{\vec{k}'}\delta^*_{\vec{k}_1'}\rangle\right]. \qquad (.5)\end{aligned}$$

The expectation value of the four $\delta's$ including noise is

$$\begin{aligned}&\left[\langle \delta_{\vec{k}}\delta^*_{\vec{k}_1}\delta_{\vec{k}'}\delta^*_{\vec{k}_1'}\rangle - \langle\delta_{\vec{k}}\delta^*_{\vec{k}_1}\rangle\langle\delta_{\vec{k}'}\delta^*_{\vec{k}_1'}\rangle\right] \\ &= (2\pi)^3\delta_D^{(3)}(\vec{k}+\vec{k}')\left(P(\vec{k})+\frac{1}{n}\right)(2\pi)^3\delta_D^{(3)}(\vec{k}_1+\vec{k}_1')\left(P(\vec{k})_1+\frac{1}{n}\right) \\ &+ (2\pi)^3\delta_D^{(3)}(\vec{k}-\vec{k}_1')\left(P(\vec{k})+\frac{1}{n}\right)(2\pi)^3\delta_D^{(3)}(\vec{k}_1-\vec{k}')\left(P(\vec{k})_1+\frac{1}{n}\right) \\ &+ (2\pi)^3\delta_D^{(3)}(\vec{k}-\vec{k}_1+\vec{k}'-\vec{k}_1')T_4^{\rm full}(\vec{k},\vec{k}_1,\vec{k}',\vec{k}_1'). \qquad (.6)\end{aligned}$$

Evaluating the first two terms of the above equation leads to the Gaussian contribution of the covariance matrix

$$\begin{aligned}C_{\xi}(\vec{r},\vec{r}') &= \frac{1}{V(\vec{r})}\int_0^{\vec{r}} d^3r_1 \frac{1}{V(\vec{r}')}\int_0^{\vec{r}'} d^3r_1' \int \frac{d^3k}{(2\pi)^3}\int \frac{d^3k_1}{(2\pi)^3}\left(P(\vec{k})+\frac{1}{n}\right)\left(P(\vec{k}_1)+\frac{1}{n}\right) \\ &\times h(\vec{k}-\vec{k}_1,\vec{r})h^*(\vec{k}'-\vec{k}_1',\vec{r}')\left(e^{i\vec{k}_1\vec{r}+i\vec{k}\vec{r}'}+e^{i\vec{k}_1\vec{r}-i\vec{k}_1\vec{r}'}\right). \qquad (.7)\end{aligned}$$

Using the approximation

$$\int \frac{d^3k}{(2\pi)^3}h(\vec{k},\vec{r})h^*(\vec{k},\vec{r}') = \frac{1}{V_s(a)}\delta_{aa'} \qquad (.8)$$

the Gaussian terms become

$$\begin{aligned} C_{\bar{\xi}}(\vec{r},\vec{r}') &= \frac{1}{V(\vec{r})}\int_0^{\vec{r}} d^3r_1 \frac{1}{V(\vec{r}')}\int_0^{\vec{r}'} d^3r'_1 \frac{1}{V_s}\int \frac{d^3k}{(2\pi)^3}\left(P(\vec{k})^2 + \frac{2P(\vec{k})}{n} + \frac{1}{n^2}\right) \\ &\times \left[e^{i\vec{k}(\vec{r}_1+\vec{r'}_1)} + e^{i\vec{k}(\vec{r}_1-\vec{r}'_1)}\right] \\ &= \frac{1}{\pi^2 V_s(a)}\frac{1}{V(r)V(r')}\int k^2dk \int_0^r 4\pi r_1^2 dr_1 \int_0^{r'} 4\pi r_1'^2 dr'_1 \\ &\times \left(\frac{\sin(kr_1)}{kr_1}\right)\left(\frac{\sin(kr'_1)}{kr'_1}\right)P(k)^2 \\ &= \frac{9}{\pi^2 r r' V_s(a)}\int dk \left(P(k)^2 + \frac{2P(k)}{n} + \frac{1}{n^2}\right) j_1(kr)j_1(kr'). \end{aligned} \tag{.9}$$

The remaining non-Gaussian terms come from the trispectrum ([169])

$$\begin{aligned} &T_4^{\rm full}(\vec{k},\vec{k}_1,\vec{k}',\vec{k}'_1) = \\ &\frac{1}{n^2}\left[P(\vec{k}-\vec{k}_1+\vec{k}') + P(\vec{k}+\vec{k}'-\vec{k}'_1) + P(\vec{k}-\vec{k}'_1-\vec{k}_1) + P(\vec{k}'-\vec{k}_1-\vec{k}'_1)\right] \\ &+\frac{1}{n^2}\left[P(\vec{k}-\vec{k}_1) + P(\vec{k}+\vec{k}') + P(\vec{k}-\vec{k}'_1)\right] + \frac{1}{n^3} \end{aligned} \tag{.10}$$

dropping all the terms proportional to the bispectrum, and four point functions, assuming a Gaussian density distribution.

Evaluating the first term of (.10) leads to a non-zero contribution only for a separation with $r = 0$, proportional to $\left[2\xi(\vec{r})\delta_D^{(3)}(\vec{r}') + 2\xi(\vec{r}')\delta_D^{(3)}(\vec{r})\right]$ and is therefore not relevant for this work. Similarly, the last term leads to

$$\begin{aligned} &\int \frac{d^3k}{(2\pi)^3}\int \frac{d^3k_1}{(2\pi)^3} e^{i\vec{k}_1\vec{r}} h(\vec{k}-\vec{k}_1,\vec{r}) \int \frac{d^3k'}{(2\pi)^3}\int \frac{d^3k'_1}{(2\pi)^3} e^{i\vec{k'}_1\vec{r'}} h(\vec{k'}-\vec{k'}_1,\vec{r'}) \frac{1}{n^3} \\ &\times \quad (2\pi)^3\delta_D^{(3)}(\vec{k}-\vec{k}_1+\vec{k}'-\vec{k}'_1) \\ &= \quad \frac{1}{n^3 V_s}\delta_D^{(3)}(\vec{r})\delta_D^{(3)}(\vec{r}'). \end{aligned} \tag{.11}$$

The only non-zero term, proportional to $1/n^2$, gives rise to a non-Gaussian contribution to

the covariance, we will denote as 'Poisson' shot noise term, and can be evaluated using

$$\begin{aligned}
& \int \frac{d^3k}{(2\pi)^3} \int \frac{d^3k_1}{(2\pi)^3} e^{i\vec{k}_1\vec{r}} h(\vec{k}-\vec{k}_1,\vec{r}) \int \frac{d^3k'}{(2\pi)^3} \int \frac{d^3k'_1}{(2\pi)^3} e^{i\vec{k'}_1\vec{r'}} h(\vec{k'}-\vec{k'}_1,\vec{r'}) \\
\times \quad & (2\pi)^3 \delta_D^{(3)}(\vec{k}-\vec{k}_1+\vec{k'}-\vec{k}'_1) \left(\frac{1}{n^2} \left[P(\vec{k}-\vec{k}_1) + P(\vec{k}+\vec{k'}) + P(\vec{k}-\vec{k}'_1) \right] \right) \\
= \quad & \int \frac{d^3k}{(2\pi)^3} \int \frac{d^3k_1}{(2\pi)^3} e^{i\vec{k}_1\vec{r}} h(\vec{k}-\vec{k}_1,\vec{r}) \int \frac{d^3k'}{(2\pi)^3} e^{i(\vec{k}-\vec{k}_1+\vec{k'})\vec{r'}} h(\vec{k}_1-\vec{k},\vec{r'}) \\
\times \quad & \left(\frac{1}{n^2} \left[P(\vec{k}-\vec{k}_1) + P(\vec{k}+\vec{k'}) + P(\vec{k}_1-\vec{k'}) \right] \right) \\
= \quad & \frac{1}{n^2 V_s} \int \frac{d^3k}{(2\pi)^3} \int \frac{d^3k'}{(2\pi)^3} e^{i\vec{k}\vec{r}} e^{i\vec{k'}\vec{r'}} \left[P(\vec{k}+\vec{k'}) + P(\vec{k}-\vec{k'}) \right] \\
= \quad & \frac{1}{n^2 V_s} \int \frac{d^3k}{(2\pi)^3} \int \frac{d^3k'}{(2\pi)^3} e^{i\vec{k'}\vec{r}} e^{i(\vec{k}-\vec{k'})\vec{r'}} P(\vec{k}) + \frac{1}{n^2 V_s} \int \frac{d^3k}{(2\pi)^3} \int \frac{d^3k'}{(2\pi)^3} e^{i(\vec{k}+\vec{k'})\vec{r}} e^{i\vec{k'}\vec{r'}} P(k) \\
= \quad & \frac{1}{n^2 V_s} \int \frac{d^3k}{(2\pi)^3} \int \frac{d^3k'}{(2\pi)^3} e^{i\vec{k'}(\vec{r}-\vec{r'})} e^{i\vec{k}\vec{r'}} P(\vec{k}) + \frac{1}{n^2 V_s} \int \frac{d^3k}{(2\pi)^3} \int \frac{d^3k'}{(2\pi)^3} e^{i\vec{k}\vec{r}} e^{i\vec{k'}(\vec{r}+\vec{r'})} P(k) \\
= \quad & \frac{1}{n^2 V_s} (\delta_D^{(3)}(\vec{r}-\vec{r'})\xi(\vec{r}) + \delta_D^{(3)}(\vec{r}+\vec{r'})\xi(\vec{r})) \qquad (.12)
\end{aligned}$$

dropping the term proportional to $P(0)$. Using spherical symmetry

$$\delta_D(\vec{r}-\vec{r'})\xi(\vec{r'}) + \delta_D(\vec{r'}-\vec{r})\xi(\vec{r}) = \frac{\delta_D(r-r')}{4\pi r^2}\xi(r') + \frac{\delta_D(r'-r)}{4\pi r'^2}\xi(r) \qquad (.13)$$

and volume averaging over r and r' leads to

$$\begin{aligned}
& \frac{1}{V(r)} \frac{1}{V(r')} \int_0^{r'} \int_0^{r} \left(\frac{\delta_D(\tilde{r}-\tilde{r}')}{4\pi\tilde{r}^2}\xi(\tilde{r}') + \frac{\delta_D(\tilde{r}'-\tilde{r})}{4\pi\tilde{r}'^2}\xi(\tilde{r}) \right) 4\pi\tilde{r}^2 4\pi\tilde{r}'^2 d\tilde{r} d\tilde{r}' \\
& = \begin{cases} \frac{2}{V(r')}\bar{\xi}(r) & \text{if } r' > r \\ \frac{2}{V(r)}\bar{\xi}(r') & \text{if } r' < r \\ \frac{1}{V(r')}\bar{\xi}(r) + \frac{1}{V(r)}\bar{\xi}(r') & \text{if } r' = r \end{cases} \qquad (.14)
\end{aligned}$$

where we have used the integral expression for the Dirac delta function

$$\begin{aligned}
\int_0^r \delta_D(\vec{\tilde{r}}-\vec{\tilde{r}}')d^3r &= \int_0^r \int_{-1}^1 2\pi\tilde{r}^2 d\tilde{r} d\mu \int \frac{dk}{(2\pi)^3} \int_{-1}^1 d\mu' 2\pi k^2 e^{ik\mu\tilde{r} - ik\mu' r'} \\
&= \frac{2}{\pi} \int dk k j_1(kr) j_0(kr') r^2 \qquad (.15)
\end{aligned}$$

to calculate the integrals as

$$\begin{aligned}
&\int_0^r \int_0^{r'} \delta_D(\vec{\tilde{r}} - \vec{\tilde{r}}')\xi(\vec{\tilde{r}}')d^3\tilde{r}d^3\tilde{r}' \\
&= \int_0^{r'} \frac{2}{\pi}\int dk k j_1(kr) j_0(k\tilde{r}') r^2 \frac{1}{2\pi^2}\int dk' k'^2 j_0(k'\tilde{r}')P(k')4\pi\tilde{r}'^2 d\tilde{r}' \\
&= \frac{2}{\pi}\int dk' P(k') \begin{cases} j_1(rk')k'r^2 & \text{if } r' > r \\ j_1(r'k')k'r'^2 & \text{if } r' < r \\ \frac{1}{2}j_1(rk')k'r^2 + \frac{1}{2}j_1(r'k')k'r'^2 & \text{if } r' = r \end{cases}
\end{aligned} \tag{.16}$$

The total covariance for the pairwise velocity correlation of cluster pairs of exact separation r and r' can therefore be written as

$$C_V(r, a, r', a') = C_V^{\text{Gaus.}}(r, a, r', a') + C_V^{\text{Poiss.}}(r, a, r', a') \tag{.17}$$

with

$$\begin{aligned}
C_V^{\text{Gaus.}}(r, a, r', a') &= \frac{4}{\pi^2 V_s(a)} \frac{H(a)a}{1+\xi(r,a)} \frac{H(a')a'}{1+\xi(r',a')} f_g(a) f_g(a')\ \delta_{aa'} \\
&\times \int dk \left(P(k,a) + \frac{1}{n(a)}\right)\left(P(k,a') + \frac{1}{n(a')}\right) j_1(kr) j_1(kr')
\end{aligned} \tag{.18}$$

$$\begin{aligned}
C_V^{\text{Poiss.}}(r, a, r', a') &= \frac{1}{V_s(a)} \frac{1}{3\pi} \frac{H(a)a}{1+\xi(r,a)} \frac{H(a')a'}{1+\xi(r',a')} f_g(a) f_g(a')\ \delta_{aa'} \\
&\times \begin{cases} \frac{r}{n(a)^2 r'^2}\bar{\xi}(r,a) & \text{if } r' \geq r \\ \frac{2r'}{n(a')^2 r^2}\bar{\xi}(r',a') & \text{if } r' < r \end{cases}
\end{aligned} \tag{.19}$$

Now we consider the statistics calculated by binning cluster separations in a bin of width Δr. In this case the pairwise velocity estimate is averaged over cluster pairs with separations within the finite bin,

$$\hat{V}(r) \to \frac{1}{V_{\text{bin}}} \int_{r-\Delta r/2}^{r+\Delta r/2} \tilde{r}^2 d\tilde{r} \int d\Omega \hat{V}(\tilde{r}) \tag{.20}$$

where we again assume spherical symmetry. Volume averaging over a bin of size $\Delta r = R_{\rm max} - R_{\rm min}$ yields

$$j_1(kr) \;\; \rightarrow \;\; \frac{3}{R_{i,\rm max}^3 - R_{i,\rm min}^3} \int_{R_{i,\rm min}}^{R_{i,\rm max}} r^2 \; j_1(kr) dr. \tag{.21}$$

Using that

$$\int_{R_{i,\rm min}}^{R_{i,\rm max}} r^2 \; j_1(kr) dr \;\; = \;\; R_{i,\rm min}^3 \tilde{W}(kR_{i,\rm min}) - R_{i,\rm max}^3 \tilde{W}(kR_{i,\rm max}) \tag{.22}$$

with

$$\tilde{W}(x) = \frac{2\cos(x) + x\sin(x)}{x^3}. \tag{.23}$$

Binning in r translates into replacing the Bessel function with a function related to the bin limits,

$$j_1(kr) \;\; \rightarrow \;\; \frac{3}{R_{i,\rm max}^3 - R_{i,\rm min}^3} \left(R_{i,\rm min}^3 \tilde{W}(kR_{i,\rm min}) - R_{i,\rm max}^3 \tilde{W}(kR_{i,\rm max}) \right) \equiv W_\Delta(kr). \tag{.24}$$

Rewriting the volume averaged correlation function in terms of the power spectrum,

$$\frac{2r}{r'^2} \bar{\xi}(r) \;\; = \;\; \frac{3}{r'^2 \pi^2} \int dk k P(k) j_1(kr), \tag{.25}$$

and with

$$\frac{1}{r^2} \rightarrow \frac{4\pi \Delta r}{V_\Delta(r)}, \tag{.26}$$

the full, angle-averaged covariance for the mean pairwise velocity, excluding measurement error, is given by the sum of a Gaussian cosmic variance and shot noise component plus a Poisson component,

$$C_V(r, a, r', a') = C_V^{\rm Gaus.}(r, a, r', a') + C_V^{\rm Poiss.}(r, a, r', a') \tag{.27}$$

with

$$C_V^{\rm Gaus.}(r,a,r',a') = \frac{4}{\pi^2 V_s(a)}\frac{H(a)a}{1+\xi(r,a)}\frac{H(a')a'}{1+\xi(r',a')}f_g(a)f_g(a')\delta_{aa'} \times \int dk\left(P(k,a)+\frac{1}{n(a)}\right)\left(P(k,a')+\frac{1}{n(a')}\right)W_\Delta(kr)W_\Delta(kr') \quad (.28)$$

$$C_V^{\rm Poiss.}(r,a,r',a') = \frac{4}{\pi^2 V_s(a)}\frac{H(a)a}{1+\xi(r,a)}\frac{H(a')a'}{1+\xi(r',a')}f_g(a)f_g(a')\ \delta_{aa'} \times \begin{cases} \frac{\Delta r'}{n(a)^2 V_\Delta(r')}\int dk k P(k,a)W_\Delta(kr) & \text{if } r' \geq r \\ \frac{\Delta r}{n(a')^2 V_\Delta(r)}\int dk k P(k,a')W_\Delta(kr') & \text{if } r' < r. \end{cases} \quad (.29)$$

These results are used in equation (3.2.13) in the main text.

References

[1] Eva-Maria Mueller, Rachel Bean, and Scott Watson. Cosmological implications of the effective field theory of cosmic acceleration. *Phys. Rev.*, D87(8):083504, 2013. arXiv:1209.2706, doi:10.1103/PhysRevD.87.083504.

[2] Eva-Maria Mueller, Francesco de Bernardis, Rachel Bean, and Michael D. Niemack. Constraints on gravity and dark energy from the pairwise kinematic Sunyaev-Zeldovich effect. *Astrophys. J.*, 808(1):47, 2015. arXiv:1408.6248, doi:10.1088/0004-637X/808/1/47.

[3] Eva-Maria Mueller, Francesco de Bernardis, Rachel Bean, and Michael D. Niemack. Constraints on massive neutrinos from the pairwise kinematic Sunyaev-Zeldovich effect. *Phys. Rev.*, D92(6):063501, 2015. arXiv:1412.0592, doi:10.1103/PhysRevD.92.063501.

[4] M. Kowalski et al. Improved Cosmological Constraints from New, Old and Combined Supernova Datasets. *Astrophys.J.*, 686:749–778, 2008. arXiv:0804.4142, doi:10.1086/589937.

[5] Adam G. Riess et al. New Hubble Space Telescope Discoveries of Type Ia Supernovae at z¿=1: Narrowing Constraints on the Early Behavior of Dark Energy. *Astrophys. J.*, 659:98–121, 2007. arXiv:astro-ph/0611572, doi:10.1086/510378.

[6] Pierre Astier et al. The Supernova legacy survey: Measurement of omega(m), omega(lambda) and W from the first year data set. *Astron.Astrophys.*, 447:31–48, 2006. arXiv:astro-ph/0510447, doi:10.1051/0004-6361:20054185.

[7] S. Perlmutter et al. Measurements of Omega and Lambda from 42 high redshift supernovae. *Astrophys.J.*, 517:565–586, 1999. arXiv:astro-ph/9812133, doi:10.1086/307221.

[8] Adam G. Riess et al. Observational evidence from supernovae for an accelerating universe and a cosmological constant. *Astron.J.*, 116:1009–1038, 1998. arXiv:astro-ph/9805201, doi:10.1086/300499.

[9] Malcolm Hicken, Peter Challis, Saurabh Jha, Robert P. Kirsher, Tom Matheson, et al. CfA3: 185 Type Ia Supernova Light Curves from the CfA. *Astrophys.J.*, 700:331–357, 2009. arXiv:0901.4787, doi:10.1088/0004-637X/700/1/331.

[10] R. Amanullah et al. Spectra and Light Curves of Six Type Ia Supernovae at 0.511 ¡ z ¡ 1.12 and the Union2 Compilation. *Astrophys. J.*, 716:712–738, 2010. arXiv:1004.1711, doi:10.1088/0004-637X/716/1/712.

[11] E. Komatsu et al. Seven-Year Wilkinson Microwave Anisotropy Probe (WMAP) Observations: Cosmological Interpretation. *Astrophys.J.Suppl.*, 192:18, 2011. arXiv:1001.4538, doi:10.1088/0067-0049/192/2/18.

[12] D. N. Spergel et al. First Year Wilkinson Microwave Anisotropy Probe (WMAP) Observations: Determination of Cosmological Parameters. *Astrophys. J. Suppl.*, 148:175, 2003. arXiv:astro-ph/0302209, doi:10.1086/377226.

[13] D. N. Spergel, R. Bean, D Dore, et al. Wilkinson Microwave Anisotropy Probe (WMAP) three year results: Implications for cosmology. *Astrophys. J. Suppl.*, 170:377, 2007. arXiv:astro-ph/0603449, doi:10.1086/513700.

[14] C. L. Reichardt et al. High resolution CMB power spectrum from the complete ACBAR data set. *Astrophys. J.*, 694:1200–1219, 2009. arXiv:0801.1491, doi:10.1088/0004-637X/694/2/1200.

[15] M. R. Nolta et al. Five-Year Wilkinson Microwave Anisotropy Probe (WMAP) Observations: Angular Power Spectra. *Astrophys. J. Suppl.*, 180:296–305, 2009. arXiv:0803.0593, doi:10.1088/0067-0049/180/2/296.

[16] C. L. Reichardt et al. A measurement of secondary cosmic microwave background anisotropies with two years of South Pole Telescope observations. *Astrophys. J.*, 755:70, 2012. arXiv:1111.0932, doi:10.1088/0004-637X/755/1/70.

[17] Will J. Percival et al. Measuring the Baryon Acoustic Oscillation scale using the SDSS and 2dFGRS. *Mon. Not. Roy. Astron. Soc.*, 381:1053–1066, 2007. arXiv:0705.3323, doi:10.1111/j.1365-2966.2007.12268.x.

[18] Chris Blake, Eyal Kazin, Florian Beutler, Tamara Davis, David Parkinson, et al. The WiggleZ Dark Energy Survey: mapping the distance-redshift relation with baryon acoustic oscillations. *Mon.Not.Roy.Astron.Soc.*, 418:1707–1724, 2011. arXiv:1108.2635, doi:10.1111/j.1365-2966.2011.19592.x.

[19] Lauren Anderson, Eric Aubourg, Stephen Bailey, Dmitry Bizyaev, Michael Blanton, et al. The clustering of galaxies in the SDSS-III Baryon Oscillation Spectroscopic Survey: Baryon Acoustic Oscillations in the Data Release 9 Spectroscopic Galaxy Sample. *Mon.Not.Roy.Astron.Soc.*, 427(4):3435–3467, 2013. arXiv:1203.6594, doi:10.1111/j.1365-2966.2012.22066.x.

[20] Edmund J. Copeland, M. Sami, and Shinji Tsujikawa. Dynamics of dark energy. *Int.J.Mod.Phys.*, D15:1753–1936, 2006. arXiv:hep-th/0603057, doi:10.1142/S021827180600942X.

[21] Shinji Tsujikawa. Modified gravity models of dark energy. *Lect.Notes Phys.*, 800:99–145, 2010. arXiv:1101.0191, doi:10.1007/978-3-642-10598-2_3.

[22] Kurt Hinterbichler. Theoretical Aspects of Massive Gravity. *Rev.Mod.Phys.*, 84:671–710, 2012. arXiv:1105.3735, doi:10.1103/RevModPhys.84.671.

[23] Michel Chevallier and David Polarski. Accelerating universes with scaling dark matter. *Int. J. Mod. Phys.*, D10:213–224, 2001. arXiv:gr-qc/0009008, doi:10.1142/S0218271801000822.

[24] Eric V. Linder. Exploring the expansion history of the universe. *Phys. Rev. Lett.*, 90:091301, 2003. arXiv:astro-ph/0208512, doi:10.1103/PhysRevLett.90.091301.

[25] Andreas Albrecht, Gary Bernstein, Robert Cahn, Wendy L. Freedman, Jacqueline Hewitt, et al. Report of the Dark Energy Task Force. 2006. arXiv:astro-ph/0609591.

[26] Istvan Laszlo and Rachel Bean. Nonlinear growth in modified gravity theories of dark

energy. *Phys. Rev.*, D77:024048, 2008. arXiv:0709.0307, doi:10.1103/PhysRevD.77.024048.

[27] Luca Amendola, Martin Kunz, and Domenico Sapone. Measuring the dark side (with weak lensing). *JCAP*, 0804:013, 2008. arXiv:0704.2421, doi:10.1088/1475-7516/2008/04/013.

[28] Eric V. Linder and Robert N. Cahn. Parameterized Beyond-Einstein Growth. *Astropart.Phys.*, 28:481–488, 2007. arXiv:astro-ph/0701317, doi:10.1016/j.astropartphys.2007.09.003.

[29] Li-Min Wang and Paul J. Steinhardt. Cluster abundance constraints on quintessence models. *Astrophys.J.*, 508:483–490, 1998. arXiv:astro-ph/9804015, doi:10.1086/306436.

[30] Eric V. Linder. Cosmic growth history and expansion history. *Phys.Rev.*, D72:043529, 2005. arXiv:astro-ph/0507263, doi:10.1103/PhysRevD.72.043529.

[31] Y. Fukuda et al. Evidence for oscillation of atmospheric neutrinos. *Phys.Rev.Lett.*, 81:1562–1567, 1998. arXiv:hep-ex/9807003, doi:10.1103/PhysRevLett.81.1562.

[32] Y. Ashie et al. Evidence for an oscillatory signature in atmospheric neutrino oscillation. *Phys.Rev.Lett.*, 93:101801, 2004. arXiv:hep-ex/0404034, doi:10.1103/PhysRevLett.93.101801.

[33] Q.R. Ahmad et al. Measurement of the rate of $\nu_e + d \rightarrow p + p + e^-$ interactions produced by ^8B solar neutrinos at the Sudbury Neutrino Observatory. *Phys.Rev.Lett.*, 87:071301, 2001. arXiv:nucl-ex/0106015, doi:10.1103/PhysRevLett.87.071301.

[34] Q.R. Ahmad et al. Direct evidence for neutrino flavor transformation from neutral current interactions in the Sudbury Neutrino Observatory. *Phys.Rev.Lett.*, 89:011301, 2002. arXiv:nucl-ex/0204008, doi:10.1103/PhysRevLett.89.011301.

[35] F.P. An et al. Observation of electron-antineutrino disappearance at Daya Bay. *Phys.Rev.Lett.*, 108:171803, 2012. arXiv:1203.1669, doi:10.1103/PhysRevLett.108.171803.

[36] K. Eguchi et al. First results from KamLAND: Evidence for reactor anti-neutrino disappearance. *Phys.Rev.Lett.*, 90:021802, 2003. arXiv:hep-ex/0212021, doi:10.1103/PhysRevLett.90.021802.

[37] M.H. Ahn et al. Measurement of Neutrino Oscillation by the K2K Experiment. *Phys.Rev.*, D74:072003, 2006. arXiv:hep-ex/0606032, doi:10.1103/PhysRevD.74.072003.

[38] K. Abe et al. Indication of Electron Neutrino Appearance from an Accelerator-produced Off-axis Muon Neutrino Beam. *Phys.Rev.Lett.*, 107:041801, 2011. arXiv:1106.2822, doi:10.1103/PhysRevLett.107.041801.

[39] K. Nakamura, K. Hagiwara, K. Hikasa, H. Murayama, M. Tanabashi, T. Watari, C. Amsler, M. Antonelli, D. M. Asner, H. Baer, H. R. Band, R. M. Barnett, T. Basaglia, E. Bergren, J. Beringer, G. Bernardi, W. Bertl, H. Bichsel, O. Biebel, E. Blucher, S. Blusk, R. N. Cahn, M. Carena, A. Ceccucci, D. Chakraborty, M. C. Chen, R. S. Chivukula, G. Cowan, O. Dahl, G. D'Ambrosio, T. Damour, D. de Florian, A. de Gouvea, T. DeGrand, G. Dissertori, B. Dobrescu, M. Doser, M. Drees, D. A. Edwards, S. Eidelman, J. Erler, V. V. Ezhela, W. Fetscher, B. D. Fields, B. Foster, T. K. Gaisser, L. Garren, H. J. Gerber, G. Gerbier, T. Gherghetta, C. F. Giudice, S. Golwala, M. Goodman, C. Grab, A. V. Gritsan, J. F. Grivaz, D. E. Groom, M. Grunewald, A. Gurtu, T. Gutsche, H. E. Haber, C. Hagmann, K. G. Hayes, M. Heffner, B. Heltsley, J. J. Hernandez-Rey, A. Hoecker, J. Holder, J. Huston, J. D. Jackson, K. F. Johnson, T. Junk, A. Karle, D. Karlen, B. Kayser, D. Kirkby, S. R. Klein, C. Kolda, R. V. Kowalewski, B. Krusche, Yu. V. Kuyanov, Y. Kwon, O. Lahav, P. Langacker, A. Liddle, Z. Ligeti, C. J. Lin, T. M. Liss, L. Littenberg, K. S. Lugovsky, S. B. Lugovsky, J. Lys, H. Mahlke, T. Mannel, A. V. Manohar, W. J. Marciano, A. D. Martin, A. Masoni, D. Milstead, R. Miquel, K. Moenig, M. Narain, P. Nason, S. Navas, P. Nevski, Y. Nir, K. A. Olive, L. Pape, C. Patrignani, J. A. Peacock, S. T. Petcov, A. Piepke, G. Punzi, A. Quadt, S. Raby, G. Raffelt, B. N. Ratcliff, P. Richardson, S. Roesler, S. Rolli, A. Romaniouk, L. J. Rosenberg, J. L. Rosner, C. T. Sachrajda, Y. Sakai, G. P. Salam, S. Sarkar, F. Sauli, O. Schneider, K. Scholberg, D. Scott, W. G. Seligman, M. H. Shaevitz, M. Silari, Torbjö rn Sjö strand, J. G. Smith, G. F. Smoot, S. Spanier, H. Spieler, A. Stahl, T. Stanev, S. L. Stone, T. Sumiyoshi, M. J. Syphers, J. Terning, M. Titov, N. P. Tkachenko, N. A. Tornqvist, D. Tovey, T. G. Trippe, G. Valencia, K. van Bibber, G. Venanzoni, M. G. Vincter, P. Vogel, A. Vogt, W. Walkowiak, C. W. Walter, D. R. Ward, B. R. Webber, G. Weiglein, E. J. Weinberg, J. D. Wells, A. Wheeler, L. R. . Wiencke, C. G. Wohl, L. Wolfenstein, J. Womersley, C. L. Woody, R. L. Workman, A. Yamamoto, W. M. Yao, O. V. Zenin, J. Zhang, R. Y. Zhu, P. A. Zyla, G. Harper, V. S. Lugovsky, and P. Schaffner. Review of particle physics. 37(7A):1–1422, 2010. URL: http://dx.doi.org/10.1088/0954-3899/37/7A/075021.

[40] K. N. Abazajian et al. Neutrino Physics from the Cosmic Microwave Background and Large Scale Structure. *Astropart. Phys.*, 63:66–80, 2015. arXiv:1309.5383, doi:10.1016/j.astropartphys.2014.05.014.

[41] P.A.R. Ade et al. Planck 2015 results. XIII. Cosmological parameters. 2015. arXiv:1502.01589.

[42] Nathalie Palanque-Delabrouille et al. Constraint on neutrino masses from sdss-iii/boss lyα forest and other cosmological probes. *JCAP*, 1502:045, 2015. arXiv:1410.7244.

[43] Mark Wyman, Douglas H. Rudd, R. Ali Vanderveld, and Wayne Hu. Neutrinos Help Reconcile Planck Measurements with the Local Universe. *Phys.Rev.Lett.*, 112(5):051302, 2014. arXiv:1307.7715, doi:10.1103/PhysRevLett.112.051302.

[44] Cora Dvorkin, Mark Wyman, Douglas H. Rudd, and Wayne Hu. Neutrinos help reconcile Planck measurements with both Early and Local Universe. *Phys.Rev.*, D90:083503, 2014. arXiv:1403.8049.

[45] E. Komatsu et al. Five-Year Wilkinson Microwave Anisotropy Probe (WMAP) Observations: Cosmological Interpretation. *Astrophys.J.Suppl.*, 180:330–376, 2009. arXiv:0803.0547, doi:10.1088/0067-0049/180/2/330.

[46] Dragan Huterer et al. Growth of Cosmic Structure: Probing Dark Energy Beyond Expansion. *Astropart. Phys.*, 63:23–41, 2015. arXiv:1309.5385, doi:10.1016/j.astropartphys.2014.07.004.

[47] R.A. Sunyaev and Ya.B. Zeldovich. The Velocity of clusters of galaxies relative to the microwave background. The Possibility of its measurement. *Mon.Not.Roy.Astron.Soc.*, 190:413–420, 1980.

[48] T. Abbott et al. The dark energy survey. 2005. arXiv:astro-ph/0510346.

[49] Paul A. Abell et al. LSST Science Book, Version 2.0. 2009. arXiv:0912.0201.

[50] R. Laureijs et al. Euclid Definition Study Report. 2011. arXiv:1110.3193.

[51] D. Spergel, N. Gehrels, J. Breckinridge, M. Donahue, A. Dressler, et al. Wide-Field InfraRed Survey Telescope-Astrophysics Focused Telescope Assets WFIRST-AFTA Final Report. 2013. arXiv:1305.5422.

[52] Johan Comparat, Jean-Paul Kneib, Stephanie Escoffier, Julien Zoubian, Anne Ealet, et al. Investigating Emission Line Galaxy Surveys with the Sloan Digital Sky Survey Telescope. *Mon.Not.Roy.Astron.Soc.*, 2012, 2012. arXiv:1207.4321, doi:10.1093/mnras/sts127.

[53] Michael Levi et al. The DESI Experiment, a whitepaper for Snowmass 2013. 2013. arXiv:1308.0847.

[54] Alexandra Abate et al. Large Synoptic Survey Telescope: Dark Energy Science Collaboration. 2012. arXiv:1211.0310.

[55] B. Joachimi and S.L. Bridle. Simultaneous measurement of cosmology and intrinsic alignments using joint cosmic shear and galaxy number density correlations. *Astron.Astrophys.*, 523:A1, 2010. arXiv:0911.2454, doi:10.1051/0004-6361/200913657.

[56] Istvan Laszlo, Rachel Bean, Donnacha Kirk, and Sarah Bridle. Disentangling dark energy and cosmic tests of gravity from weak lensing systematics. *Mon. Not. Roy. Astron. Soc.*, 423:1750, 2012. arXiv:1109.4535, doi:10.1111/j.1365-2966.2012.20994.x.

[57] Donnacha Kirk, Istvan Laszlo, Sarah Bridle, and Rachel Bean. Optimising cosmic shear surveys to measure modifications to gravity on cosmic scales. 2011. arXiv:1109.4536.

[58] Juliana Kwan, Geraint F. Lewis, and Eric V. Linder. Mapping Growth and Gravity with Robust Redshift Space Distortions. *Astrophys.J.*, 748:78, 2012. arXiv:1105.1194, doi:10.1088/0004-637X/748/2/78.

[59] A. Heavens. Fisher Matrices and All That: Experimental Design and Data Compression. In V. J. Martínez, E. Saar, E. Martínez-González, and M.-J. Pons-Bordería, editors, *Data Analysis in Cosmology*, volume 665 of *Lecture Notes in Physics, Berlin Springer Verlag*, pages 51–72, 2009. doi:10.1007/978-3-540-44767-2_2.

[60] David B. Kaplan. Five lectures on effective field theory. 2005. arXiv:nucl-th/0510023.

[61] C.P. Burgess. Introduction to Effective Field Theory. *Ann.Rev.Nucl.Part.Sci.*, 57:329–362, 2007. arXiv:hep-th/0701053, doi:10.1146/annurev.nucl.56.080805.140508.

[62] Clifford Cheung, Paolo Creminelli, A. Liam Fitzpatrick, Jared Kaplan, and Leonardo Senatore. The Effective Field Theory of Inflation. *JHEP*, 0803:014, 2008. arXiv:0709.0293, doi:10.1088/1126-6708/2008/03/014.

[63] Leonardo Senatore and Matias Zaldarriaga. The Effective Field Theory of Multifield Inflation. *JHEP*, 1204:024, 2012. arXiv:1009.2093, doi:10.1007/JHEP04(2012)024.

[64] Anastasios Avgoustidis, Sera Cremonini, Anne-Christine Davis, Raquel H. Ribeiro, Krzysztof Turzynski, and Scott Watson. Decoupling Survives Inflation: A Critical Look at Effective Field Theory Violations During Inflation. *JCAP*, 1206:025, 2012. arXiv:1203.0016, doi:10.1088/1475-7516/2012/06/025.

[65] Steven Weinberg. Effective Field Theory for Inflation. *Phys.Rev.*, D77:123541, 2008. arXiv:0804.4291, doi:10.1103/PhysRevD.77.123541.

[66] Minjoon Park, Kathryn M. Zurek, and Scott Watson. A Unified Approach to Cosmic Acceleration. *Phys.Rev.*, D81:124008, 2010. arXiv:1003.1722, doi:10.1103/PhysRevD.81.124008.

[67] Jolyon K. Bloomfield and Eanna E. Flanagan. A Class of Effective Field Theory Models of Cosmic Acceleration. *JCAP*, 1210:039, 2012. arXiv:1112.0303, doi:10.1088/1475-7516/2012/10/039.

[68] Raul Jimenez, P. Talavera, and Licia Verde. An effective theory of accelerated expansion. *Int.J.Mod.Phys.*, A27:1250174, 2012. arXiv:1107.2542, doi:10.1142/S0217751X12501746.

[69] Raul Jimenez, P. Talavera, Licia Verde, Michele Moresco, Andrea Cimatti, et al. The effective Lagrangian of dark energy from observations. *JCAP*, 1203:014, 2012. arXiv:1201.3608, doi:10.1088/1475-7516/2012/03/014.

[70] Nima Khosravi. Effective Field Theory of Multi-Field Inflation a la Weinberg. *JCAP*, 1205:018, 2012. arXiv:1203.2266, doi:10.1088/1475-7516/2012/05/018.

[71] Paolo Creminelli, Guido D'Amico, Jorge Norena, and Filippo Vernizzi. The Effective Theory of Quintessence: the w¡-1 Side Unveiled. *JCAP*, 0902:018, 2009. arXiv:0811.0827, doi:10.1088/1475-7516/2009/02/018.

[72] Justin Khoury and Amanda Weltman. Chameleon fields: Awaiting surprises for tests of gravity in space. *Phys.Rev.Lett.*, 93:171104, 2004. arXiv:astro-ph/0309300, doi:10.1103/PhysRevLett.93.171104.

[73] Bhuvnesh Jain and Justin Khoury. Cosmological Tests of Gravity. *Annals Phys.*, 325:1479–1516, 2010. arXiv:1004.3294, doi:10.1016/j.aop.2010.04.002.

[74] Kurt Hinterbichler and Justin Khoury. Symmetron Fields: Screening Long-Range Forces Through Local Symmetry Restoration. *Phys.Rev.Lett.*, 104:231301, 2010. arXiv:1001.4525, doi:10.1103/PhysRevLett.104.231301.

[75] G. W. Horndeski. Second-Order Scalar-Tensor Field Equations in a Four-Dimensional Space. *International Journal of Theoretical Physics*, 10:363–384, September 1974. doi:10.1007/BF01807638.

[76] Christos Charmousis, Edmund J. Copeland, Antonio Padilla, and Paul M. Saffin. General second order scalar-tensor theory, self tuning, and the Fab Four. *Phys.Rev.Lett.*, 108:051101, 2012. arXiv:1106.2000, doi:10.1103/PhysRevLett.108.051101.

[77] Pedro G. Ferreira and Michael Joyce. Cosmology with a Primordial Scaling Field. *Phys. Rev.*, D58:023503, 1998. arXiv:astro-ph/9711102, doi:10.1103/PhysRevD.58.023503.

[78] Christof Wetterich. The Cosmon model for an asymptotically vanishing time dependent cosmological 'constant'. *Astron.Astrophys.*, 301:321–328, 1995. arXiv:hep-th/9408025.

[79] Rachel Bean, Eanna E. Flanagan, Istvan Laszlo, and Mark Trodden. Constraining Interactions in Cosmology's Dark Sector. *Phys. Rev.*, D78:123514, 2008. arXiv:0808.1105, doi:10.1103/PhysRevD.78.123514.

[80] Luca Amendola, David Polarski, and Shinji Tsujikawa. Are f(R) dark energy models cosmologically viable ? *Phys.Rev.Lett.*, 98:131302, 2007. arXiv:astro-ph/0603703, doi:10.1103/PhysRevLett.98.131302.

[81] Edmund J. Copeland, Andrew R Liddle, and David Wands. Exponential potentials and cosmological scaling solutions. *Phys.Rev.*, D57:4686–4690, 1998. arXiv:gr-qc/9711068, doi:10.1103/PhysRevD.57.4686.

[82] Wayne Hu and Ignacy Sawicki. Models of f(R) Cosmic Acceleration that Evade Solar-System Tests. *Phys. Rev.*, D76:064004, 2007. arXiv:0705.1158, doi:10.1103/PhysRevD.76.064004.

[83] Richard A. Battye and Jonathan A. Pearson. Effective action approach to cosmological perturbations in dark energy and modified gravity. *JCAP*, 1207:019, 2012. arXiv:1203.0398, doi:10.1088/1475-7516/2012/07/019.

[84] Jonathan A. Pearson. Effective field theory for perturbations in dark energy and modified gravity. 2012. arXiv:1205.3611.

[85] Tessa Baker, Pedro G. Ferreira, and Constantinos Skordis. The Parameterized Post-Friedmann Framework for Theories of Modified Gravity: Concepts, Formalism and Examples. *Phys.Rev.*, D87:024015, 2013. arXiv:1209.2117, doi:10.1103/PhysRevD.87.024015.

[86] Christopher F. Kolda and David H. Lyth. Quintessential difficulties. *Phys.Lett.*, B458:197–201, 1999. arXiv:hep-ph/9811375, doi:10.1016/S0370-2693(99)00657-7.

[87] C.P. Burgess, Hyun Min Lee, and Michael Trott. Power-counting and the Validity of the Classical Approximation During Inflation. *JHEP*, 0909:103, 2009. arXiv:0902.4465, doi:10.1088/1126-6708/2009/09/103.

[88] Nima Arkani-Hamed, Hsin-Chia Cheng, Markus A. Luty, and Shinji Mukohyama. Ghost condensation and a consistent infrared modification of gravity. *JHEP*, 0405:074, 2004. arXiv:hep-th/0312099, doi:10.1088/1126-6708/2004/05/074.

[89] Shinji Tsujikawa and M. Sami. String-inspired cosmology: Late time transition from scaling matter era to dark energy universe caused by a Gauss-Bonnet coupling. *JCAP*, 0701:006, 2007. arXiv:hep-th/0608178, doi:10.1088/1475-7516/2007/01/006.

[90] Valeria Pettorino, Luca Amendola, Carlo Baccigalupi, and Claudia Quercellini. Constraints on coupled dark energy using CMB data from WMAP and SPT. *Phys. Rev.*, D86:103507, 2012. arXiv:1207.3293, doi:10.1103/PhysRevD.86.103507.

[91] Rachel Bean, Steen H. Hansen, and Alessandro Melchiorri. Early universe constraints on a primordial scaling field. *Phys.Rev.*, D64:103508, 2001. arXiv:astro-ph/0104162, doi:10.1103/PhysRevD.64.103508.

[92] Andreas Albrecht and Constantinos Skordis. Phenomenology of a realistic accelerating universe using only Planck scale physics. *Phys.Rev.Lett.*, 84:2076–2079, 2000. arXiv:astro-ph/9908085, doi:10.1103/PhysRevLett.84.2076.

[93] Tomi Koivisto and David F. Mota. Gauss-Bonnet Quintessence: Background Evolution, Large Scale Structure and Cosmological Constraints. *Phys.Rev.*, D75:023518, 2007. arXiv:hep-th/0609155, doi:10.1103/PhysRevD.75.023518.

[94] N. Suzuki et al. The Hubble Space Telescope Cluster Supernova Survey: V. Improving the Dark Energy Constraints Above z¿1 and Building an Early-Type-Hosted Supernova Sample. *Astrophys. J.*, 746:85, 2012. arXiv:1105.3470, doi:10.1088/0004-637X/746/1/85.

[95] Wayne Hu and Naoshi Sugiyama. Small scale cosmological perturbations: An Analytic approach. *Astrophys.J.*, 471:542–570, 1996. arXiv:astro-ph/9510117, doi:10.1086/177989.

[96] Daniel J. Eisenstein et al. Detection of the baryon acoustic peak in the large-scale correlation function of SDSS luminous red galaxies. *Astrophys.J.*, 633:560–574, 2005. arXiv:astro-ph/0501171, doi:10.1086/466512.

[97] Daniel J. Eisenstein and Wayne Hu. Baryonic features in the matter transfer function. *Astrophys.J.*, 496:605, 1998. arXiv:astro-ph/9709112, doi:10.1086/305424.

[98] Nikhil Padmanabhan, Xiaoying Xu, Daniel J. Eisenstein, Richard Scalzo, Antonio J. Cuesta, et al. A 2 per cent distance to z=0.35 by reconstructing baryon acoustic oscillations - I. Methods and application to the Sloan Digital Sky Survey. *Mon.Not.Roy.Astron.Soc.*, 427(3):2132–2145, 2012. arXiv:1202.0090, doi:10.1111/j.1365-2966.2012.21888.x.

[99] Dragan Huterer and Glenn Starkman. Parameterization of dark-energy properties: A Principal-component approach. *Phys.Rev.Lett.*, 90:031301, 2003. arXiv:astro-ph/0207517, doi:10.1103/PhysRevLett.90.031301.

[100] Pengjie Zhang, Michele Liguori, Rachel Bean, and Scott Dodelson. Probing Gravity at Cosmological Scales by Measurements which Test the Relationship between Gravitational Lensing and Matter Overdensity. *Phys. Rev. Lett.*, 99:141302, 2007. arXiv:0704.1932, doi:10.1103/PhysRevLett.99.141302.

[101] Peng-Jie Zhang, Albert Stebbins, Roman Juszkiewicz, and Hume Feldman. A New method of measuring the peculiar velocity power spectrum. *Astrophys.J.Lett.*, 2004. arXiv:astro-ph/0410637.

[102] A. Diaferio, S. Borgani, L. Moscardini, G. Murante, K. Dolag, et al. Measuring cluster peculiar velocities with the sunyaev-zeldovich effects: scaling relations and systematics. *Mon.Not.Roy.Astron.Soc.*, 356:1477–1488, 2005. arXiv:astro-ph/0405365, doi:10.1111/j.1365-2966.2004.08586.x/abs/.

[103] Carlos Hernandez-Monteagudo, Licia Verde, Raul Jimenez, and David N. Spergel. Correlation properties of the kinematic sunyaev-zel'dovich effect and implications for dark energy. *Astrophys.J.*, 643:598–615, 2006. arXiv:astro-ph/0511061, doi:10.1086/503190.

[104] Simon DeDeo, David N. Spergel, and Hy Trac. The kinetic sunyaev-zel'dovitch effect as a dark energy probe. 2005. arXiv:astro-ph/0511060.

[105] Pablo Fosalba and Olivier Dore. Probing the Largest Cosmological Scales with the CMB-Velocity Correlation. *Phys.Rev.*, D76:103523, 2007. arXiv:astro-ph/0701782, doi:10.1103/PhysRevD.76.103523.

[106] Suman Bhattacharya and Arthur Kosowsky. Cosmological Constraints from Galaxy

Cluster Velocity Statistics. *Astrophys.J.*, 659:L83–L86, 2007. arXiv:astro-ph/0612555, doi:10.1086/517523.

[107] Arthur Kosowsky and Suman Bhattacharya. A Future Test of Gravitation Using Galaxy Cluster Velocities. *Phys. Rev.*, D80:062003, 2009. arXiv:0907.4202, doi:10.1103/PhysRevD.80.062003.

[108] D. S. Y. Mak, E. Pierpaoli, and S. J. Osborne. Measuring Bulk Flow of Galaxy Clusters using Kinematic Sunyaev-Zel'dovich effect: Prediction for Planck. *Astrophys. J.*, 736:116, 2011. arXiv:1101.1581, doi:10.1088/0004-637X/736/2/116.

[109] W. L. Holzapfel, P. A. R. Ade, S. E. Church, P. D. Mauskopf, Y. Rephaeli, T. M. Wilbanks, and Andrew E. Lange. Limits on the peculiar velocities of two distant clusters using the kinematic Sunyaev-Zel'dovich effect. *Astrophys. J.*, 481:35, 1997. arXiv:astro-ph/9702223, doi:10.1086/304019.

[110] B. A. Benson, Sarah E. Church, P. A. R. Ade, J. J. Bock, K. M. Ganga, J. R. Hinderks, P. D. Mauskopf, B. Philhour, M. C. Runyan, and K. L. Thompson. Peculiar velocity limits from measurements of the spectrum of the Sunyaev - Zel'dovich effect in six clusters of galaxies. *Astrophys. J.*, 592:674–691, 2003. arXiv:astro-ph/0303510, doi:10.1086/375864.

[111] T. Kitayama, E. Komatsu, N. Ota, T. Kuwabara, Y. Suto, K. Yoshikawa, M. Hattori, and H. Matsuo. Exploring cluster physics with high-resolution sunyaev-zel'dovich effect images and x-ray data: a case of the most x-ray luminous galaxy cluster rxj1347-1145. *Publ. Astron. Soc. Jap.*, 56:17–28, 2004. arXiv:astro-ph/0311574.

[112] Piers Horner, Philip Mauskopf, James Aguirre, Jamie Bock, Eiichi Egami, Jason Glenn, Sunil Golwala, Glenn Laurent, Hien Nguyen, and Jack Sayers. A high signal to noise ratio map of the Sunyaev-Zel'dovich increment at 1.1 mm wavelength in Abell 1835. 2010. arXiv:1005.4699.

[113] Tony Mroczkowski et al. A Multi-wavelength Study of the Sunyaev-Zel'dovich Effect in the Triple-Merger Cluster MACS J0717.5+3745 with MUSTANG and Bolocam. *Astrophys. J.*, 761:47, 2012. arXiv:1205.0052, doi:10.1088/0004-637X/761/1/47.

[114] M. Zemcov et al. High Spectral Resolution Measurement of the Sunyaev-Zel'dovich

Effect Null with Z-Spec. *Astrophys. J.*, 749:114, 2012. arXiv:1202.0029, doi:10.1088/0004-637X/749/2/114.

[115] J. Sayers, T. Mroczkowski, M. Zemcov, P.M. Korngut, J. Bock, et al. A Measurement of the Kinetic Sunyaev-Zel'dovich Signal Toward MACS J0717.5+3745. *Astrophys.J.*, 778(52):52, 2013. arXiv:1312.3680, doi:10.1088/0004-637X/778/1/52.

[116] S.J. Osborne, D.S.Y. Mak, S.E. Church, and E. Pierpaoli. Measuring the Galaxy Cluster Bulk Flow from WMAP data. *Astrophys.J.*, 737:98, 2011. arXiv:1011.2781, doi:10.1088/0004-637X/737/2/98.

[117] P.A.R. Ade et al. Planck intermediate results. XIII. Constraints on peculiar velocities. *Astron.Astrophys.*, 2013. arXiv:1303.5090.

[118] O. Zahn et al. Cosmic microwave background constraints on the duration and timing of reionization from the South Pole Telescope. *Astrophys. J.*, 756:65, 2012. arXiv:1111.6386, doi:10.1088/0004-637X/756/1/65.

[119] Jonathan L. Sievers et al. The Atacama Cosmology Telescope: Cosmological parameters from three seasons of data. *JCAP*, 1310:060, 2013. arXiv:1301.0824, doi:10.1088/1475-7516/2013/10/060.

[120] Ming Li, Raul E. Angulo, Simon D. M. White, and Jens Jasche. Matched filter optimization of kSZ measurements with a reconstructed cosmological flow field. *Mon. Not. Roy. Astron. Soc.*, 443(3):2311–2326, 2014. arXiv:1404.0007, doi:10.1093/mnras/stu1224.

[121] J. W. Fowler, M. D. Niemack, S. R. Dicker, A. M. Aboobaker, P. A. R. Ade, E. S. Battistelli, M. J. Devlin, R. P. Fisher, M. Halpern, P. C. Hargrave, A. D. Hincks, M. Kaul, J. Klein, J. M. Lau, M. Limon, T. A. Marriage, P. D. Mauskopf, L. Page, S. T. Staggs, D. S. Swetz, E. R. Switzer, R. J. Thornton, and C. E. Tucker. Optical design of the Atacama Cosmology Telescope and the Millimeter Bolometric Array Camera. *Applied Optics*, 46:3444–3454, June 2007. arXiv:arXiv:astro-ph/0701020, doi:10.1364/AO.46.003444.

[122] Nick Hand, Graeme E. Addison, Eric Aubourg, Nick Battaglia, Elia S. Battistelli, et al. Evidence of Galaxy Cluster Motions with the Kinematic Sunyaev-Zel'dovich Effect.

Phys.Rev.Lett., 109:041101, 2012. arXiv:1203.4219, doi:10.1103/PhysRevLett.109.041101.

[123] M.D. Niemack, P.A.R. Ade, J. Aguirre, F. Barrientos, J.A. Beall, et al. ACTPol: A polarization-sensitive receiver for the Atacama Cosmology Telescope. *Proc.SPIE Int.Soc.Opt.Eng.*, 7741:77411S, 2010. arXiv:1006.5049.

[124] J.E. Austermann, K.A. Aird, J.A. Beall, D. Becker, A. Bender, et al. SPTpol: an instrument for CMB polarization measurements with the South Pole Telescope. *Proc.SPIE Int.Soc.Opt.Eng.*, 8452:84520E, 2012. arXiv:1210.4970.

[125] E. Calabrese, R. Hložek, N. Battaglia, J. R. Bond, F. de Bernardis, M. J. Devlin, A. Hajian, S. Henderson, J. C. Hill, A. Kosowsky, T. Louis, J. McMahon, K. Moodley, L. Newburgh, M. D. Niemack, L. A. Page, B. Partridge, N. Sehgal, J. L. Sievers, D. N. Spergel, S. T. Staggs, E. R. Switzer, H. Trac, and E. J. Wollack. Precision Epoch of Reionization studies with next-generation CMB experiments. *ArXiv e-prints*, June 2014. arXiv:1406.4794.

[126] B. A. Benson, P. A. R. Ade, Z. Ahmed, S. W. Allen, K. Arnold, J. E. Austermann, A. N. Bender, L. E. Bleem, J. E. Carlstrom, C. L. Chang, H. M. Cho, S. T. Ciocys, J. F. Cliche, T. M. Crawford, A. Cukierman, T. de Haan, M. A. Dobbs, D. Dutcher, W. Everett, A. Gilbert, N. W. Halverson, D. Hanson, N. L. Harrington, K. Hattori, J. W. Henning, G. C. Hilton, G. P. Holder, W. L. Holzapfel, K. D. Irwin, R. Keisler, L. Knox, D. Kubik, C. L. Kuo, A. T. Lee, E. M. Leitch, D. Li, M. McDonald, S. S. Meyer, J. Montgomery, M. Myers, T. Natoli, H. Nguyen, V. Novosad, S. Padin, Z. Pan, J. Pearson, C. L. Reichardt, J. E. Ruhl, B. R. Saliwanchik, G. Simard, G. Smecher, J. T. Sayre, E. Shirokoff, A. A. Stark, K. Story, A. Suzuki, K. L. Thompson, C. Tucker, K. Vanderlinde, J. D. Vieira, A. Vikhlinin, G. Wang, V. Yefremenko, and K. W. Yoon. SPT-3G: A Next-Generation Cosmic Microwave Background Polarization Experiment on the South Pole Telescope. *ArXiv e-prints*, July 2014. arXiv:1407.2973.

[127] M. Davis and P. J. E. Peebles. On the integration of the BBGKY equations for the development of strongly nonlinear clustering in an expanding universe. *Astrophys.J.Suppl.*, 34:425–450, August 1977. doi:10.1086/190456.

[128] Roman Juszkiewicz, Volker Springel, and Ruth Durrer. Dynamics of pairwise motions. *Astrophys. J.*, 518:L25–L28, 1999. arXiv:astro-ph/9812387, doi:10.1086/312055.

[129] P.G. Ferreira, R. Juszkiewicz, H.A. Feldman, M. Davis, and Andrew H. Jaffe. Streaming velocities as a dynamical estimator of omega. *Astrophys.J.*, 515:L1–L4, 1999. arXiv:astro-ph/9812456, doi:10.1086/311959.

[130] Ravi K. Sheth, Antonaldo Diaferio, L. Hui, and Roman Scoccimarro. On the streaming motions of haloes and galaxies. *Mon.Not.Roy.Astron.Soc.*, 326:463–472, 2001. arXiv:astro-ph/0010137, doi:10.1046/j.1365-8711.2001.04457.x.

[131] Suman Bhattacharya and Arthur Kosowsky. Dark Energy Constraints from Galaxy Cluster Peculiar Velocities. *Phys.Rev.*, D77:083004, 2008. arXiv:0712.0034, doi:10.1103/PhysRevD.77.083004.

[132] Daniel J. Eisenstein and Matias Zaldarriaga. Correlations in the spatial power spectrum inferred from angular clustering: methods and application to apm. *Astrophys. J.*, 546:2, 2001. arXiv:astro-ph/9912149, doi:10.1086/318226.

[133] Joanne D. Cohn. Power spectrum and correlation function errors: Poisson vs. Gaussian shot noise. *New Astron.*, 11:226–239, 2006. arXiv:astro-ph/0503285, doi:10.1016/j.newast.2005.08.002.

[134] Nick Hand et al. The Atacama Cosmology Telescope: Detection of Sunyaev-Zel'dovich Decrement in Groups and Clusters Associated with Luminous Red Galaxies. *Astrophys. J.*, 736:39, 2011. arXiv:1101.1951, doi:10.1088/0004-637X/736/1/39.

[135] Chiaki Hikage, Rachel Mandelbaum, Masahiro Takada, and David N. Spergel. Where are the Luminous Red Galaxies (LRGs)? Using correlation measurements and lensing to relate LRGs to dark matter halos. *Mon. Not. Roy. Astron. Soc.*, 435:2345, 2013. arXiv:1211.1009, doi:10.1093/mnras/stt1446.

[136] Hugo Martel, Fidle Robichaud, and Paramita Barai. Major Cluster Mergers and the Location of the Brightest Cluster Galaxy. *Astrophys. J.*, 786:79, 2014. arXiv:1403.3063, doi:10.1088/0004-637X/786/2/79.

[137] Martin White, M. Blanton, A. Bolton, D. Schlegel, J. Tinker, et al. The clustering of massive galaxies at z 0.5 from the first semester of BOSS data. *Astrophys.J.*, 728:126, 2011. arXiv:1010.4915, doi:10.1088/0004-637X/728/2/126.

[138] E.S. Rykoff et al. redMaPPer I: Algorithm and SDSS DR8 Catalog. *Astrophys.J.*, 785:104, 2014. arXiv:1303.3562, doi:10.1088/0004-637X/785/2/104.

[139] Ryan Keisler and Fabian Schmidt. Prospects for measuring the relative velocities of galaxy clusters in photometric surveys using the kinetic Sunyaev-Zel'dovich Effect. *Astrophys.J.*, 765:L32, 2013. arXiv:1211.0668, doi:10.1088/2041-8205/765/2/L32.

[140] Benjamin Koester et al. A MaxBCG Catalog of 13,823 Galaxy Clusters from the Sloan Digital Sky Survey. *Astrophys.J.*, 660:239–255, 2007. arXiv:astro-ph/0701265, doi:10.1086/509599.

[141] N. Battaglia, J.R. Bond, C. Pfrommer, J.L. Sievers, and D. Sijacki. Simulations of the Sunyaev-Zel'dovich Power Spectrum with AGN Feedback. *Astrophys.J.*, 725:91–99, 2010. arXiv:1003.4256, doi:10.1088/0004-637X/725/1/91.

[142] Andreu Font-Ribera, Patrick McDonald, Nick Mostek, Beth A. Reid, Hee-Jong Seo, et al. DESI and other dark energy experiments in the era of neutrino mass measurements. *JCAP*, 1405:023, 2014. arXiv:1308.4164, doi:10.1088/1475-7516/2014/05/023.

[143] Luca Amendola et al. Cosmology and fundamental physics with the Euclid satellite. 2012. arXiv:1206.1225.

[144] J. E. Geach et al. Empirical H-alpha emitter count predictions for dark energy surveys. *Mon. Not. Roy. Astron. Soc.*, 402:1330, 2010. arXiv:0911.0686, doi:10.1111/j.1365-2966.2009.15977.x.

[145] Yun Wang, Chia-Hsun Chuang, and Christopher M. Hirata. Toward More Realistic Forecasting of Dark Energy Constraints from Galaxy Redshift Surveys. *Mon. Not. Roy. Astron. Soc.*, 430:2446, 2013. arXiv:1211.0532, doi:10.1093/mnras/stt068.

[146] James W. Colbert, Harry Teplitz, Hakim Atek, Andrew Bunker, Marc Rafelski, et al. Predicting Future Space Near-IR Grism Surveys using the WFC3 Infrared Spectroscopic Parallels Survey. *Astrophys.J.*, 779:34, 2013. arXiv:1305.1399, doi:10.1088/0004-637X/779/1/34.

[147] Teppei Okumura, Uros Seljak, Zvonimir Vlah, and Vincent Desjacques. Peculiar

velocities in redshift space: formalism, N-body simulations and perturbation theory. *JCAP*, 1405:003, 2014. arXiv:1312.4214, doi:10.1088/1475-7516/2014/05/003.

[148] Neelima Sehgal, Arthur Kosowsky, and Gilbert Holder. Constrained Cluster Parameters from Sunyaev-Zel'dovich Observations. *Astrophys.J.*, 635:22–34, 2005. arXiv:astro-ph/0504274, doi:10.1086/497258.

[149] S.Y. Sazonov and R.A. Sunyaev. Microwave polarization in the direction of galaxy clusters induced by the CMB quadrupole anisotropy. *Mon.Not.Roy.Astron.Soc.*, 310:765–772, 1999. arXiv:astro-ph/9903287, doi:10.1046/j.1365-8711.1999.02981.x.

[150] Ravi K. Sheth and Antonaldo Diaferio. Peculiar velocities of galaxies and clusters. *Mon.Not.Roy.Astron.Soc.*, 322:901, 2001. arXiv:astro-ph/0009166, doi:10.1046/j.1365-8711.2001.04202.x.

[151] Daisuke Nagai, Andrey V. Kravtsov, and Arthur Kosowsky. Effect of internal flows on Sunyaev-Zeldovich measurements of cluster peculiar velocities. *Astrophys.J.*, 587:524–532, 2003. arXiv:astro-ph/0208308, doi:10.1086/368281.

[152] Gilbert P. Holder. Measuring cluster peculiar velocities and temperatures at CM and MM wavelengths. *Astrophys.J.*, 602:18–25, 2004. arXiv:astro-ph/0207600, doi:10.1086/380916.

[153] Puxun Wu, Hong Wei Yu, and Xiangyun Fu. A Parametrization for the growth index of linear matter perturbations. *JCAP*, 0906:019, 2009. arXiv:0905.3444, doi:10.1088/1475-7516/2009/06/019.

[154] Julien Lesgourgues and Sergio Pastor. Massive neutrinos and cosmology. *Phys.Rept.*, 429:307–379, 2006. arXiv:astro-ph/0603494, doi:10.1016/j.physrep.2006.04.001.

[155] Julien Lesgourgues and Sergio Pastor. Neutrino cosmology and Planck. *New J.Phys.*, 16:065002, 2014. arXiv:1404.1740, doi:10.1088/1367-2630/16/6/065002.

[156] K. N. Abazajian, E. Calabrese, A. Cooray, F. De Bernardis, S. Dodelson, A. Friedland, G. M. Fuller, S. Hannestad, B. G. Keating, E. V. Linder, C. Lunardini, A. Melchiorri,

R. Miquel, E. Pierpaoli, J. Pritchard, P. Serra, M. Takada, and Y. Y. Y. Wong. Cosmological and astrophysical neutrino mass measurements. *Astroparticle Physics*, 35:177–184, November 2011. arXiv:1103.5083, doi:10.1016/j.astropartphys.2011.07.002.

[157] Antony Lewis, Anthony Challinor, and Anthony Lasenby. Efficient computation of CMB anisotropies in closed FRW models. *Astrophys.J.*, 538:473–476, 2000. arXiv:astro-ph/9911177, doi:10.1086/309179.

[158] Jacob Brandbyge, Steen Hannestad, Troels Haugboelle, and Yvonne Y.Y. Wong. Neutrinos in Non-linear Structure Formation - The Effect on Halo Properties. *JCAP*, 1009:014, 2010. arXiv:1004.4105, doi:10.1088/1475-7516/2010/09/014.

[159] Emanuele Castorina, Emiliano Sefusatti, Ravi K. Sheth, Francisco Villaescusa-Navarro, and Matteo Viel. Cosmology with massive neutrinos II: on the universality of the halo mass function and bias. *JCAP*, 1402:049, 2014. arXiv:1311.1212, doi:10.1088/1475-7516/2014/02/049.

[160] Suman Bhattacharya, Katrin Heitmann, Martin White, Zarija Lukic, Christian Wagner, and Salman Habib. Mass Function Predictions Beyond LCDM. *Astrophys. J.*, 732:122, 2011. arXiv:1005.2239, doi:10.1088/0004-637X/732/2/122.

[161] Angeliki Kiakotou, Oystein Elgaroy, and Ofer Lahav. Neutrino Mass, Dark Energy, and the Linear Growth Factor. *Phys.Rev.*, D77:063005, 2008. arXiv:0709.0253, doi:10.1103/PhysRevD.77.063005.

[162] Kyle S. Dawson et al. The Baryon Oscillation Spectroscopic Survey of SDSS-III. 2012. arXiv:1208.0022.

[163] Erminia Calabrese, Rene Hloek, Nick Battaglia, J. Richard Bond, Francesco de Bernardis, et al. Precision Epoch of Reionization studies with next-generation CMB experiments. *JCAP*, 1408:010, 2014. arXiv:1406.4794, doi:10.1088/1475-7516/2014/08/010.

[164] Julien Lesgourgues, Laurence Perotto, Sergio Pastor, and Michel Piat. Probing neutrino masses with cmb lensing extraction. *Phys. Rev.*, D73:045021, 2006. arXiv:astro-ph/0511735, doi:10.1103/PhysRevD.73.045021.

[165] Takemi Okamoto and Wayne Hu. CMB lensing reconstruction on the full sky. *Phys. Rev.*, D67:083002, 2003. arXiv:astro-ph/0301031, doi:10.1103/PhysRevD.67.083002.

[166] P. A. R. Ade et al. Planck 2013 results. XVI. Cosmological parameters. *Astron. Astrophys.*, 571:A16, 2014. arXiv:1303.5076, doi:10.1051/0004-6361/201321591.

[167] Jolyon K. Bloomfield, anna . Flanagan, Minjoon Park, and Scott Watson. Dark energy or modified gravity? An effective field theory approach. *JCAP*, 1308:010, 2013. arXiv:1211.7054, doi:10.1088/1475-7516/2013/08/010.

[168] P. A. R. Ade et al. Planck 2015 results. XIV. Dark energy and modified gravity. 2015. arXiv:1502.01590.

[169] S. Matarrese, Licia Verde, and A.F. Heavens. Large scale bias in the universe: Bispectrum method. *Mon.Not.Roy.Astron.Soc.*, 290:651–662, 1997. arXiv:astro-ph/9706059, doi:10.1093/mnras/290.4.651.